

1225-0767(ISSN Print)  
2287-6715(ISSN Online)  
한국연구재단 우수등재학술지

# Journal of Ocean Engineering and Technology

Vol. 36, No. 6 (Serial Number 169)

December 2022

한국해양공학회지



[www.joet.org](http://www.joet.org)



The Korean Society of Ocean Engineers

## Editorial Board

### ■ Editor-in-Chief

Joonmo Choung Inha University, Korea

### ■ Head Editors

Jong Chun Park Pusan National University, Korea

Do Kyun Kim Seoul National University, Korea

Kwon-Hoo Kim Pukyong National University, Korea

Sungwon Shin Hanyang University, Korea

Woo Dong Lee Gyeongsang National University, Korea

### ■ Editorial Board Members

Atila Incecik University of Strathclyde, UK

Beom-Seon Jang Seoul National University, Korea

Binbin Li Tsinghua University, China

Bo Woo Nam Seoul National University, Korea

Byongug Jeong University of Strathclyde, UK

Chang Yong Song Mokpo National University, Korea

Chong Hyun Lee Jeju National University, Korea

Choonghyun Kang Gyeongsang National University, Korea

Dongho Jung Korea Research Institute of Ships & Ocean Engineering, Korea

Erkan Oterkus University of Strathclyde, UK

Gökhan Tansel Tayyar Istanbul Technical University, Turkey

Gyusung Cho Tongmyong University, Korea

Hooi-Siang Kang Universiti Teknologi Malaysia, Malaysia

Hyeon Kyu Yoon Changwon National University, Korea

Hyun-Sik Kim Tongmyong University, Korea

Jeong-Hwan Kim Dong-A University, Korea

Jinwhan Kim Korea Advanced Institute of Science and Technology, Korea

Joohyun Woo Korea Maritime and Ocean University, Korea

Jooyong Lee i-CoAST, Korea

Junbong Jang Dong-A University, Korea

Jung Kwan Seo Pusan National University, Korea

Kangsu Lee Korea Research Institute of Ships & Ocean Engineering, Korea

Kideok Do Korea Maritime and Ocean University, Korea

Kwang-Jun Paik Inha University, Korea

Moo Hyun Kim Texas A&M University, USA

Narakorn Srin Newcastle University, UK

Sang Jin Kim National Sun Yat-sen University, Taiwan

Se-Min Jeong Chosun University, Korea

Seokhwan Ahn Jungwon University, Korea

Seongim Choi Gwangju Institute of Science and Technology, Korea

Seung Min Park Hyein Engineering & Construction, Co., Ltd., Korea

Seung-Ho Ham Changwon National University, Korea

Soonchul Kwon Pusan National University, Korea

Sung-Woong Choi Gyeongsang National University, Korea

Taeseong Kim Loughborough University, UK

TaeSoon Kang GeoSystem Research Corp., Korea

Tak Kee Lee Gyeongsang National University, Korea

Weoncheol Koo Inha University, Korea

Yeon-Joong Kim Inje University, Korea

Yeulwoo Kim Pukyong National University, Korea

Yoon Hyeok Bae Jeju National University, Korea

Younghun Kim Kyungnam University, Korea

Youngsub Lim Seoul National University, Korea

## Research and Publication Ethics Committee

### ■ Chair

Jae-Yong Ko Mokpo National Maritime University, Korea

### ■ Research and Publication Ethics Committee Members

Jinwhan Kim Korea Advanced Institute of Science and Technology, Korea

Jin Ho Lee Pukyong National University, Korea

Kangsu Lee Korea Research Institute of Ships & Ocean Engineering, Korea

Joon-Young Kim Korea Maritime and Ocean University, Korea

**Published on** December 31, 2022

**Published by** The Korean Society of Ocean Engineers (KSOE)

Room 1302, 13, Jungang-daero 180beon-gil, Dong-gu, Busan, 48821, Korea

TEL: +82-51-759-0656 FAX: +82-51-759-0657 E-mail: ksoehj@ksoe.or.kr URL: http://www.ksoe.or.kr

**Printed by** Hanrimwon Co., Ltd., Seoul, Korea E-mail: hanrim@hanrimwon.co.kr

**ISSN(print)** 1225-0767 **ISSN(online)** 2287-6715

This journal was supported by the Korean Federation of Science and Technology Societies (KOFST) grant funded by the Korean government.

© 2022 by The Korean Society of Ocean Engineers (KSOE)

This is an open access article distributed under the terms of the creative commons attribution non-commercial license (<http://creativecommons.org/licenses/by-nc/4.0>) which permits unrestricted non-commercial use, distribution, and reproduction in any medium, provided the original work is properly cited.

# Journal of Ocean Engineering and Technology

한국해양공학회지

## CONTENTS

Volume 36, Number 6

December, 2022

---

### <Original Research Articles>

- Designation of the Boundary Conditions for Estimating the Thrust Loss due to Thruster-Hull Interactions  
Gi Su Song, Seung Jae Lee and Ju Sung Kim ..... 353
- Numerical Investigation of Countermeasure Effects on Overland Flow Hydrodynamic and Force Mitigation in Coastal Communities  
Hai Van Dang, Sungwon Shin, Eunju Lee, Hyongsu Park and Jun-Nyeong Park ..... 364
- An Analysis of the Impact of Building Wind by Field Observation in Haeundae LCT Area, South Korea: Typhoon Omais in 2021  
Byeonggug Kang, Jongyeong Kim, Yongju Kwon, Joowon Choi, Youngsu Jang and Soonchul Kwon ..... 380
- Motion Analysis of A Wind-Wave Energy TLP Platform Considering Second-order Wave Forces  
Hongbhin Kim, Eun-hong Min, Sanghwan Heo and WeonCheol Koo ..... 390

## GENERAL INFORMATION

“Journal of Ocean Engineering and Technology” is the official journal published by “The Korean Society of Ocean Engineers (KSOE)”. The ISO abbreviation is “J. Ocean Eng. Technol.” and acronym is “**JOET**”. It was launched in 1987. It is published bimonthly in February, April, June, August, October, and December each year. Supplement numbers are published at times.

Journal of Ocean Engineering and Technology (JOET) is a medium for the publication of original research and development work in the field of ocean engineering. JOET covers the entire range of issues and technologies related to the following topics:

**Ships and offshore platforms:** Design of marine structures; Resistance and propulsion; Seakeeping and maneuvering; Experimental and computational fluid dynamics; Ocean wave mechanics; Fatigue strength; Plasticity; Optimization and reliability; Arctic technology and extreme mechanics; Noise, vibration, and acoustics; Concrete engineering; Thermodynamics and heat transfer; Hydraulics and pneumatics;

**Coastal civil engineering:** Coastal structures; Port and harbor structures; Soil mechanics; Drilling and exploration; Hydraulics of estuary; Seismic engineering; Coastal disaster prevention engineering;

**Ocean renewable energy platforms:** Offshore wind turbines; Wave energy platforms; Tidal current energy platforms; Floating photovoltaic energy platforms;

**Marine robots:** Robot sensor system; Autonomous navigation; Robot equipments; Spatial information and communications; Underwater network; Design of underwater vehicles;

**Multidisciplinary areas:** Design for safety; IT-based design; IT-based production engineering; Welding mechanics; Control engineering; GPS and GIS; Inspection and sensor; Port and logistics; Leisure boat and deep sea water; Offshore process systems engineering; Marine metallic materials; Marine organic materials; Marine Composite materials; Materials properties; Corrosion and Anti-corrosion; Tribology;

It contains original research articles, case reports, brief communications and reviews on technical issues. Conference papers, research papers, diploma papers and academic articles can be submitted.

All of the manuscripts are peer-reviewed. **JOET** has a system where two or more peer reviewers must review each submitted paper and it is operated very strictly.

**JOET** is an open access journal distributed under the terms of the creative commons attribution non-commercial license (<http://creativecommons.org/licenses/by-nc/4.0>). Therefore, all ocean engineers and researchers around the world can easily access all journal articles via the journal homepage (<http://www.joet.org>) and download the PDF-based original texts or view the web-based XML texts for free.

**JOET** is being indexed in some prominent database such as Korean Citation Index (KCI), Google Scholar, Science Central, Korea Science and Directory of Open Access Journals (DOAJ).

For correspondences concerning business matters, author needs to contact KSOE Secretariat by email or phone (e-mail: [ksoehj@ksoe.or.kr](mailto:ksoehj@ksoe.or.kr) or Tel: +82 51 759 0656). Correspondences for publication matters can be asked via email to the Editor-in-Chief (email: [heroeswise2@gmail.com](mailto:heroeswise2@gmail.com)).



# Designation of the Boundary Conditions for Estimating the Thrust Loss due to Thruster-Hull Interactions

Gi Su Song<sup>1</sup>, Seung Jae Lee<sup>2</sup> and Ju Sung Kim<sup>3</sup>

<sup>1</sup>Assistant Professor, Division of Naval Architecture and Ocean Systems Engineering, Korea Maritime and Ocean University, Busan, Korea

<sup>2</sup>Professor, Division of Naval Architecture and Ocean Systems Engineering, Korea Maritime and Ocean University, Busan, Korea

<sup>3</sup>Principal Research Engineer, Samsung Ship Model Basin, Samsung Heavy Industries Co. Ltd., Daejeon, Korea

**KEY WORDS:** Thruster-Hull interaction, Thrust loss, Azimuth thruster, Current load, CFD

**ABSTRACT:** The azimuth thruster is mainly installed on a vessel that requires a dynamic positioning (DP) function for special purposes. When the azimuth thruster on a vessel operates for DP, the thrust loss is induced by the thruster-hull interaction. This study examined the influence of boundary conditions in numerical simulations for predicting thrust loss. Wind turbine installation vessels (WTIV) and floating production storage and offloading (FPSO) were chosen as a target vessels. In this study, two types of boundaries were defined. The first consideration is that the boundary condition was assigned with consideration of the azimuth angle of the thruster, whereas it is fixed regardless azimuth angle of the thruster. The predicted thrust loss according to these boundary conditions showed a difference. This observation originated from the current load of the vessel. Therefore, the boundary conditions for which the current load is not induced need to be designated to obtain a realistic thrust loss in a numerical simulation.

## 1. Introduction

In the design of various floating offshore facilities or special purpose vessels, such as floating production storage and offloading (FPSO), wind turbine installation vessels (WTIV), semi-submergible, and drillship, the dynamic positioning (DP) performance is one of the most important performance indicators that is related directly to the operating performance of the facility. Efficient use of the thrust generated by the propulsion system is essential to respond to various marine environments (wind, waves, and currents) and operate marine facilities or special vessels stably and economically simultaneously. Hence, multiple azimuth thrusters are generally installed in offshore facilities or special vessels. The installed azimuth thruster must consume minimum power and, at the same time, effectively produce thrust to achieve optimal DP performance. Hence, the operating direction, required thrust, and power consumption of the azimuth thruster are controlled according to the optimization algorithm. On the other hand, a loss of thrust occurs compared to the case where it exists alone when an azimuth thruster is attached to an offshore facility or special vessel. Dang and Laheij (2004) attributed this phenomenon is caused by four interference effects. These refer to the thruster-hull

interference effect, thruster-thruster interference effect, thruster-tide interference effect, and thruster-wave interference effect, and accurate prediction of thrust reduction is an essential factor to consider while selecting an azimuth thruster with appropriate capacity at the design stage of offshore facilities and special vessels. The decrease in thrust due to these interference effects has been studied previously using model tests and numerical methods.

As a representative example, Lehn (1980) examined thrust reduction by the thruster-thruster interference effect. When two azimuth thrusters are placed in a row, they studied how the thrust performance of the azimuth thruster located at the rear deteriorates according to the distance ( $x$ ) between the two thrusters or the operating direction ( $\phi$ ) of the azimuth thruster located at the front and proposed a simple estimation formula (Fig. 1). Nienhuis (1992) studied how the wake characteristics of an azimuth thruster located at the bottom of the hull

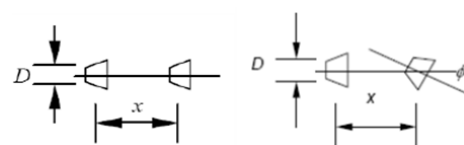


Fig. 1 Example of thruster-thruster interaction

Received 29 November 2022, revised 29 November 2022, accepted 12 December 2022

Corresponding author Seung Jae Lee: +82-51-410-4309, [slee@kmou.ac.kr](mailto:slee@kmou.ac.kr)

© 2022, The Korean Society of Ocean Engineers

This is an open access article distributed under the terms of the creative commons attribution non-commercial license (<http://creativecommons.org/licenses/by-nc/4.0>) which permits unrestricted non-commercial use, distribution, and reproduction in any medium, provided the original work is properly cited.

change depending on the side curvature when the wake flows toward the side of the vessel. Cozijn et al. (2010) conducted a study similar to Nienhuis (1992) using the Particle image velocimetry test equipment and precisely measured and analyzed the wake. Since the 2000s, studies using numerical analysis methods have been conducted. Song et al. (2013) simulated the thruster-hull interference effect and the thruster-thruster interference effect using a numerical analysis method with the WTIV as a target vessel. They conducted a quantitative study to compare the thrust loss with the model test results. Ottens et al. (2011) numerically predicted the thrust loss due to the thruster-hull interference effect for semi-submergible. In addition, the duct or propeller axis of the azimuth thruster is rotated (tilt) downward by about  $5^{\circ}$ – $7^{\circ}$  to minimize the thrust loss due to the thruster-hull mutual interference effect and Palm et al. (2010) studied the resulting changes in thrust performance and mutual interference effect. Dang and Laheij (2004) reported that although there are numerous variables, such as vessel type, hull shape, stern appendage, and special thruster shape, the loss of thrust due to the thruster-hull interference effect can comprise up to approximately 40% of the thrust produced by an azimuth thruster in a single state. In addition, the actual DP is usually conducted under the bollard condition, in which only the thruster operates while offshore facilities or special vessels are stopped. Although there are points to note in implementing this condition in numerical analysis, research on the imposition of boundary conditions is lacking (Song et al., 2022).

In predicting the thrust loss that inevitably occurs due to the thruster-hull interference effect, this study compared the difference that occurs depending on the method of imposing boundary conditions in numerical analysis and proposed what boundary conditions can be practically applied when performing a similar analysis in the future. Chapter 2 describes the numerical analysis method in detail, and Chapter 3 compares the difference in thrust loss calculated according to the boundary condition imposition method. Chapter 4 considers the cause of the difference in thrust loss, and Chapter 5 presents the conclusions drawn from this study. The Samsung Ship Model Basin provided the shape of the target vessel used in this study, the shape of the azimuth thruster, and related model test results.

## 2. Numerical Analysis Method

### 2.1 Definition of Numerical Analysis Method

This study conducted a numerical analysis using STAR-CCM+ code, one of the commercial software for fluid analysis. Table 1 lists the basic numerical analysis techniques applied in this study.

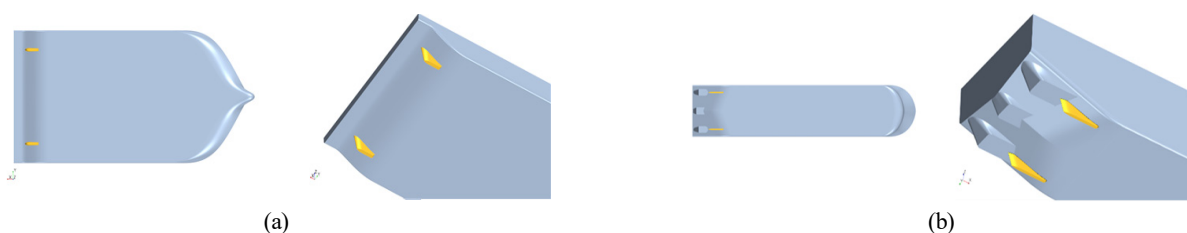


Fig. 2 Target vessel: (a) WTIV and (b) FPSO

Table 1 Numerical setup

Item	Description
Code	STAR-CCM+ V.13
Turbulence model	Realizable $k-\varepsilon$ model
Convection term	2nd order upwind
Grid type	Unstructured grid (Trimmer)
Pressure-Velocity coupling	Semi-implicit method for pressure linked equations

### 2.2 Definition of Target Vessels

WTIV and FPSO were the target vessels, and their specifications are listed in Table 2. A large difference in specifications was observed because the inherent purpose of the two vessels is different. In particular, there is a large difference in the width/draft ratio ( $B/T$ ) because WTIV has a relatively small draft compared to the width, resulting in a  $B/T$  value of 11.8. By contrast, FPSO has a relatively small value of 4.84, meaning that the draft is larger than WTIV. Fig. 2 shows target vessels, respectively.

Table 2 Main particulars of target vessels (WTIV and FPSO)

Vessel	WTIV (A)	FPSO (B)	Ratio (=A/B)
Length, $L$ (m)	126	294.6	0.4
Breadth, $B$ (m)	52	62	1.8
Design draft, $T$ (m)	4.4	12.8	0.3
$L / B$	2.42	4.75	0.5
$B / T$	11.8	4.84	2.4
Scale ratio	25.9	32.5	-

### 2.3 Performance Comparison of the Azimuth Thruster in a Single State

Azimuth thrusters were applied as the main propulsion system to all the above-mentioned vessels. The thrust calculated in a single state must be secured first before evaluating the thrust loss due to thruster-hull mutual interference in the actual target vessel. Therefore, this section discusses the single performance of the azimuth thruster predicted through numerical analysis. Table 3 lists the specifications of the model azimuth thruster manufactured for the model test. The thrust of an azimuth thruster is defined as the sum of three components because of its morphological characteristics. The total thrust ( $K_{TT}$ ) of the azimuth thruster is the sum of the thrust produced by the propeller

**Table 3** Specifications of model azimuth thruster

Item	Description
Duct	19A
Propeller	SP463
Model propeller diameter (mm)	140
Revolution of propeller	20

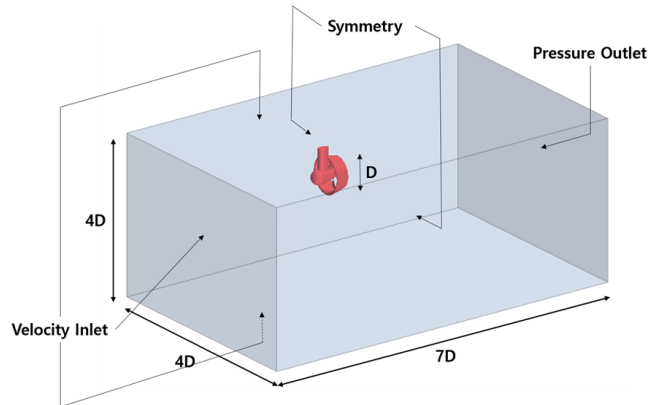


**Fig. 3** Computational domain and boundary condition for the Propeller Open Water of an azimuth thruster

( $K_{TP}$ ), the thrust produced by the duct ( $K_{TD}$ ), and the resistance ( $R$ ) of the remaining components (Housing, Leg, and Support). Numerical analysis was performed to construct a grid system so that the total thrust value calculated from the results of the single state of the azimuth thruster showed a <3% difference compared to the measured

value of the model test. This analysis was performed using the direct rotation method (sliding mesh) that directly rotates the propeller, and  $Y_1^+$ , the dimensionless grid size, was set to 50 near the wall to use the wall function. The total grid was approximately 1.5 million; other numerical analysis conditions are listed in Table 1. To perform the single state analysis, the computational domain was defined as  $7D \times 4D \times 4D$  based on the propeller diameter, and the velocity inlet condition, pressure outlet condition, and symmetry boundary condition were imposed, as shown in Fig. 3 (Song et al., 2013). In addition, the advance ratio ( $J$ ) considered was from 0.1 to 0.5. Fig. 4 shows the model azimuth thruster installed on the towing carriage, the shape defined for numerical analysis, and the grid system around the azimuth thruster. The results of a single test and numerical analysis are shown in Fig. 5 and Table 4 (Song et al., 2013).

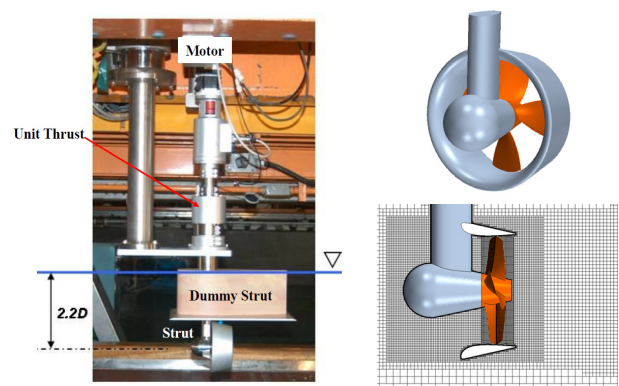


**Fig. 4** Model test for the Propeller Open Water of an azimuth thruster and geometry, grid system

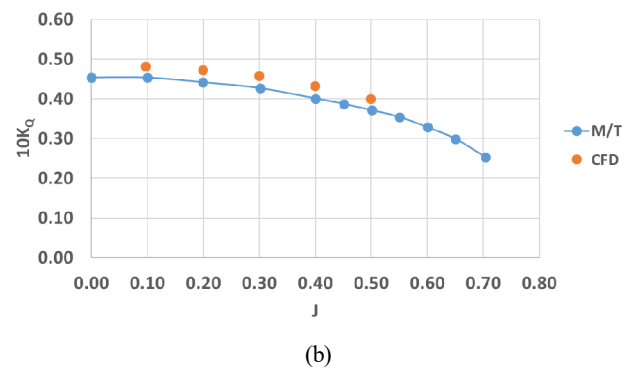
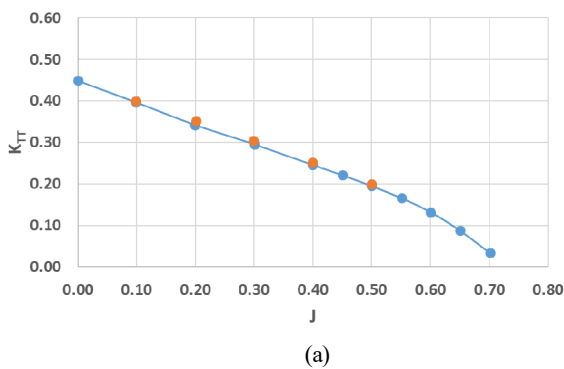


**Fig. 5** Comparison of the Propeller Open Water on azimuth thruster from the model test and CFD simulation: (a) Total thrust coefficient ( $K_{TT}$ ); (b) Torque coefficient ( $10K_Q$ )

**Table 4** Comparison of  $K_{TT}$  and  $10K_Q$  results from CFD and Mode test

$J$ (Advance ratio)	CFD (A)		Model Test (B)		Difference [1-(A)/(B)]	
	$K_{TT}$	$10K_Q$	$K_{TT}$	$10K_Q$	$K_{TT}$	$10K_Q$
0.1	0.399	0.482	0.397	0.453	0.65%	6.34%
0.2	0.352	0.473	0.342	0.441	2.88%	7.15%
0.3	0.304	0.458	0.295	0.427	2.90%	7.40%
0.4	0.252	0.432	0.246	0.400	2.38%	7.89%
0.5	0.200	0.400	0.195	0.371	2.56%	7.70%
Average	-	-	-	-	2.28%	7.30%

The total thrust of the azimuth thruster showed results within the target range of 3% in the area of an advance ratio where the analysis was performed, whereas the torque showed a consistent difference of approximately 7–8% overall. Because the purpose of this study was related to the thrust of the azimuth thruster, it was judged that the reliability of the numerical analysis for the single state of the azimuth thruster was secured based on the predicted thrust coefficient.

When the advance ratio,  $J = 0$ , the thrust coefficient under the bollard condition can be estimated and used as a reference thrust value when predicting the thrust reduction due to the actual thruster-hull interference effect.

2.4 Analysis Condition Definition

The computational domain was defined to numerically analyze the thrust reduction due to the thruster-hull interference effect, as shown in Fig. 6. The size of the computational area was defined based on the length ( $L$ ) of the target vessel and had sizes of  $3.0L$ ,  $3.0L$ , and  $1.2L$  in the X, Y, and Z directions, respectively (Song et al., 2013; Song et al., 2022). In this study, the free water surface was not considered, and the area below the waterline of the vessel was defined as the analysis area. Symmetric boundary conditions were also applied to the top and bottom surfaces of the computational area.

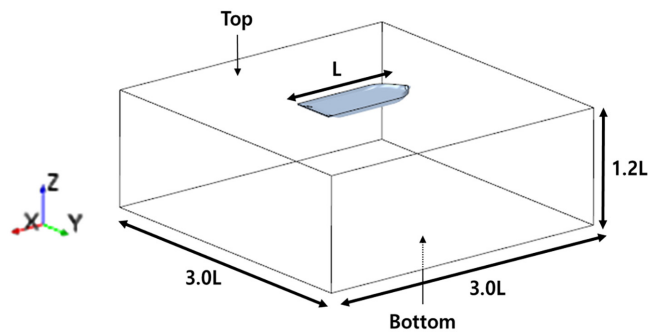


Fig. 6 Computational domain for target vessel

2.4.1 Target vessel 1: WTIV

For WTIV, studies have been conducted on thrust reduction due to the thruster-hull interference effect through model tests, and Fig. 7 shows a model vessel manufactured for model testing (Song et al., 2013). In this vessel, two azimuth thrusters were installed: one on the port and one on the starboard sides of the stern. In the model test, a thrust reduction due to the thruster-hull interference effect was found by measuring all the applied forces in the longitudinal direction (X) and the transverse direction (Y) of the vessel when the azimuth thrusters calculate the thrust for each operating direction while the vessel is stationary. In the model test, the longitudinal/lateral forces applied to the hull were measured under 24 conditions while rotating the azimuth angle of the port azimuth thrusters once at  $15^\circ$  intervals. Numerical analysis was performed under seven azimuth conditions ( $0^\circ$ ,  $45^\circ$ ,  $90^\circ$ ,  $135^\circ$ ,  $180^\circ$ ,  $225^\circ$ , and  $270^\circ$ ) where the thrust reduction result due to the thruster-hull interference effect can be known. Table 5 lists the reference coordinate system and the operating direction of the

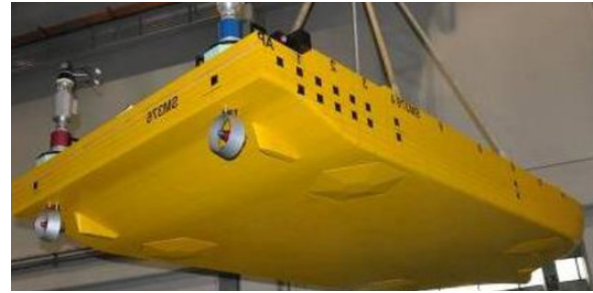


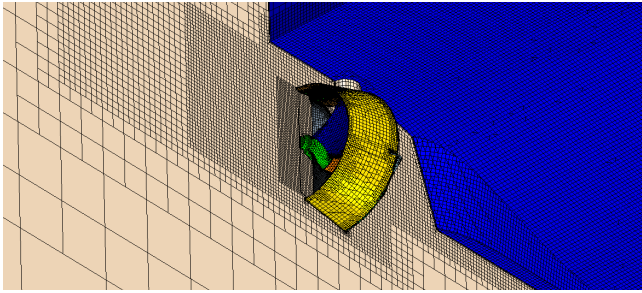
Fig. 7 Ship and azimuth thruster for model test

Table 5 Specifications of the coordinate system and simulation cases with respect to azimuthing angle on the port side

Geometry	
Coordinate system	$0^\circ$
$45^\circ$	$90^\circ$
$135^\circ$	$180^\circ$
$225^\circ$	$270^\circ$

port azimuth thrusters. Moreover, to perform the analysis under the same conditions as the model test, the analysis was conducted by changing the azimuth angle of the port azimuth thrusters while azimuth thrusters were modeled on both sides.

The grid system for numerical analysis was configured in the same way as the method applied to the single-state analysis of the azimuth thruster mentioned earlier. The thrust reduction due to the thruster-hull interference effect was ultimately caused by the wake of the azimuth thruster being attached to the hull surface by the Coanda effect, increasing the frictional resistance of the hull, or colliding with a part of the hull and increasing the pressure of the hull. Therefore, as the wake simulation of the azimuth thruster is important, the lattice system was densely constructed in this wake space, as shown in Fig. 8.













**Fig. 8** Grid system for CFD on target vessel, WTIV

Furthermore, if the direct rotation method of the propeller is applied, it is advantageous in terms of accuracy, but it takes a long time to calculate. Song et al. (2013) compared the thrust loss results by simulating propeller rotation. Based on their study, the moving reference frame (MRF) method was applied to this study. The total grid system defined for the two azimuth thrusters and the hull below the waterline was approximately 3.5 million (Song et al., 2022).

**2.4.2 Target vessel 2: FPSO**

For FPSO, there are three mounting parts (hereafter, head box) at the stern, and one azimuth thruster is located on each side of the head box, as shown in Fig. 2. In the case of this target vessel, a separate model test was not conducted. The thrust loss due to the thruster-hull interference effect was calculated using a numerical analysis method.

**Table 6** Simulation cases with respect to the azimuth angle

Azimuth thruster on the port side	Azimuth thruster on the center
 0°	 0°
 45°	 45°
 60°	 60°
 75°	 75°
 115°	 115°

For this, five azimuth angles (0°, 45°, 60°, 75°, and 115°) were defined while each azimuth thruster was installed independently on the port side or center of the head box, as shown in Table 6.

The azimuth thrusters installed on the FPSO have the same shape as those installed on the previous target vessel, WTIV. On the other hand, they have different capacities and different scale ratios between the target vessels. The diameter of the model azimuth thrusters installed on the FPSO was defined as 120mm, the parts related to numerical analysis were the same as in the case of Section 2.4.1, and the total number of grids was approximately 4.7 million.

**2.5 Definition of Boundary Condition**

The boundary conditions that can appropriately simulate the hydrodynamic situation of the analysis target must be defined before performing a reliable numerical analysis. This study defined the appropriate boundary conditions when the thrust loss due to the thruster-hull was predicted under the bollard condition where the advance ratio ( $J$ ) was zero, such as the DP operating situation, and the vessel was stationary. As mentioned by Funeno (2009), numerical analysis under the bollard condition is unstable with poor convergence, so an artificially small advance ratio must be defined for numerical stability. The value was defined as 0.05 in this study. With the symmetry boundary condition defined on the top and bottom of the computational domain, each of the four sides shown in Fig. 9 was intended to be imposed in the following two forms, as shown in Fig. 6. The first boundary condition imposition method always set the velocity-inlet condition on the bow-direction surface and the pressure-outlet condition on the stern-direction surface regardless of the direction of the azimuth thruster attached to the hull. A symmetry boundary condition was imposed on the remaining two surfaces, called Fixed BC. The second boundary condition imposition method was to impose inflow and outflow conditions to the side in the same operating direction as the azimuth thruster attached to the hull. This was called Directional BC. Table 7 lists the boundary conditions by selecting some of the azimuths mentioned in Tables 5 and 6 for one of the target vessels. In particular, when the inflow conditions were given for each azimuth angle, the velocity in the X direction and Y direction was decomposed into components and defined as much as the azimuth angle of the azimuth thruster.

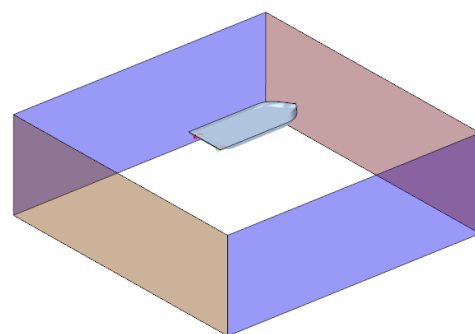
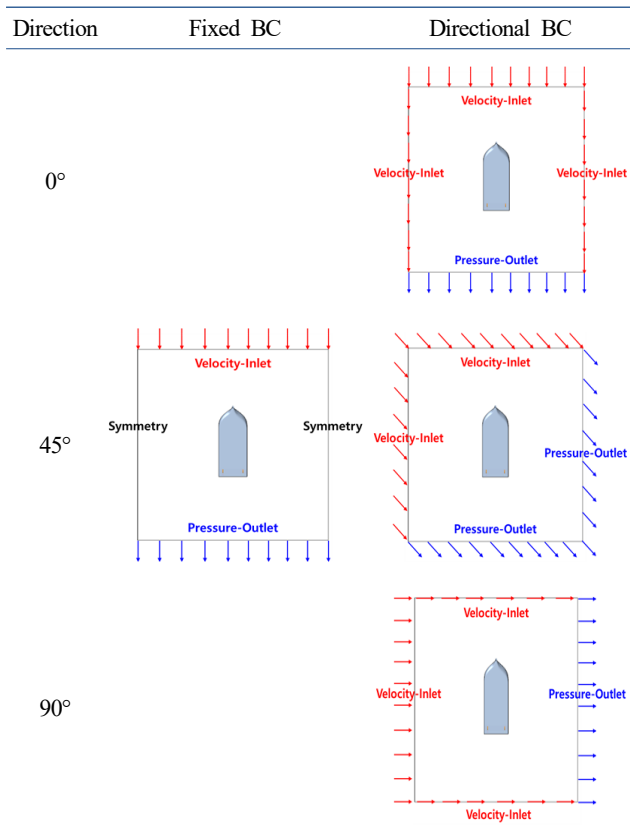


**Fig. 9** Computational domain for the definition of the boundary condition



**Table 7** Definition of different boundary condition



### 3. Numerical Analysis Result

#### 3.1 Target Vessel 1: WTIV

Fig. 10 presents the force in the X direction ( $F_x\_Hull$ ) and the force in the Y direction ( $F_y\_Hull$ ) measured across the entire hull, including the thruster, when the model azimuth thrusters attached to the port side operates in each azimuth direction under different boundary conditions, and the resulting force ( $F\_Total$ ) is shown according to the operating direction of the propeller. The resulting force ( $F\_Total$ ) is defined using Eq. (1).

$$F\_Total = \sqrt{(F_x\_Hull)^2 + (F_y\_Hull)^2} \tag{1}$$

Table 8 lists the values of  $F_x\_Hull$  and  $F_y\_Hull$  among the numerical analysis results calculated from the model test and imposed boundary conditions. Table 9 presents the degree of conformity between the  $F\_Total$  values and the model test. The numerical analysis results generally showed a similar trend to the test results. As shown in Fig. 10(c), for the force ( $F\_Total$ ), the thrust loss occurs due to the thruster-hull interference effect between approximately 75° and 240°. Comparing the differences according to the method of imposing boundary conditions, the resulting force ( $F\_Total$ ) calculated from Fixed BC showed a result closer to the model test result than the result calculated from Directional BC.

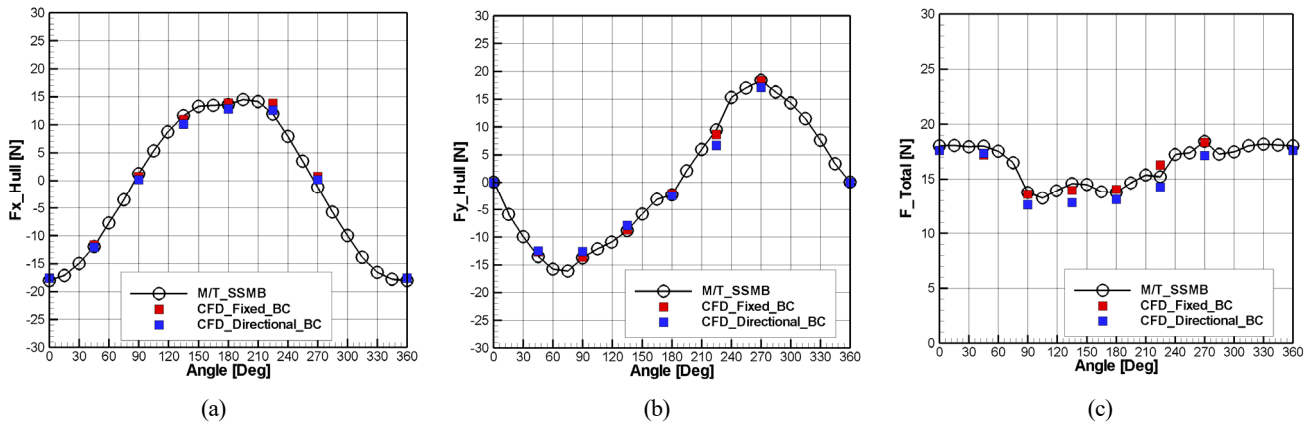


**Fig. 10** Comparison of  $F_x\_Hull$  (a),  $F_y\_Hull$  (b) and  $F\_Total$  (c) with respect to azimuthing angle from CFD and model test

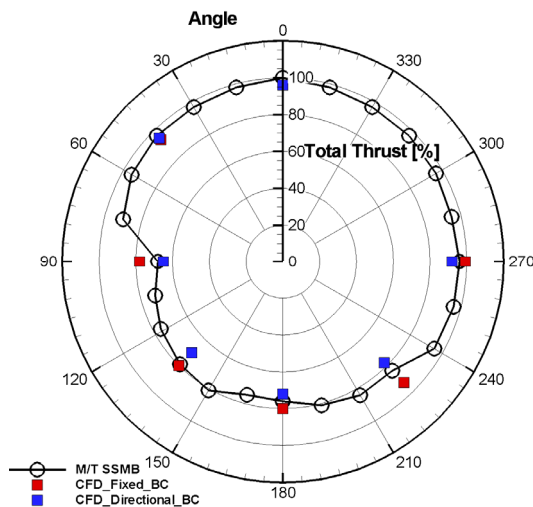
**Table 8** Comparison of  $F_x\_Hull$ ,  $F_y\_Hull$  from M/T and CFD

Method	M/T		CFD			
			Fixed BC		Directional BC	
Angle	$F_x\_Hull$ (N)	$F_y\_Hull$ (N)	$F_x\_Hull$ (N)	$F_y\_Hull$ (N)	$F_x\_Hull$ (N)	$F_y\_Hull$ (N)
0°	-18.1	0.1	-17.6	0.0	-17.6	0.0
45°	-12.0	-13.5	-11.6	-12.7	-12.1	-12.5
90°	1.2	-13.7	0.8	-13.6	0.2	-12.6
135°	11.6	-8.8	10.9	-8.7	10.1	-7.9
180°	13.6	-2.3	13.9	-2.1	12.9	-2.5
225°	11.9	9.5	13.8	8.6	12.6	6.7
270°	-1.2	18.4	0.7	18.3	0.2	17.2

**Table 9** Comparison of  $F_{Total}$  from M/T and CFD

Method	M/T		CFD			
			Fixed BC		Directional BC	
Angle	$F_{Total}$ (N)	%	$F_{Total}$ (N)	%	$F_{Total}$ (N)	%
0°	18.1	100.0	17.6	97.5	17.6	97.5
45°	18.0	100.0	17.2	95.5	17.4	96.4
90°	13.8	100.0	13.6	99.1	12.6	91.9
135°	14.6	100.0	14.0	95.7	12.8	87.8
180°	13.8	100.0	14.0	101.9	13.1	95.2
225°	15.2	100.0	16.3	107.2	14.3	94.0
270°	18.5	100.0	18.4	99.5	17.2	93.0

Fig. 11 shows the thrust loss due to the thruster-hull interference effect according to the operating azimuth of the port azimuth thrusters, and Table 10 lists the specific values. The model test showed that approximately 30% and 20% of the thrust loss occurs at 90° and 180°, respectively. Numerical analysis showed that the overall trend was similar to the test value, but the results of applying the Fixed BC at the remaining azimuth angles except for 90° and 225° were closer to the model test results than the results of applying the Directional BC. Moreover, the case of applying the Directional BC tends to predict a larger thrust loss than the case of applying the Fixed BC.


**Fig. 11** Normalized total thrust on the azimuth angle

**Table 10** Comparison of normalized total thrust on the azimuth angle from M/T and CFD

Azimuth angle	M/T	Fixed BC
0°	100%	96%
45°	97%	95%
90°	68%	78%
135°	79%	80%
180°	76%	80%
225°	84%	93%
270°	96%	99%

### 3.2 Target Vessel 2: FPSO

In the case of this target vessel, unlike the previous case, only numerical analysis was performed at the model scale without model tests. Three azimuth thrusters were attached to this target vessel (Table 6), and the analysis was performed on the thrust loss due to the thruster-hull interference effect targeting the azimuth thrusters located on the port side and in the center. At this stage, unlike the case of WTIV, where both azimuth thrusters were considered, the case of this target vessel was defined as a situation in which one azimuth thruster was installed independently on the port side and in the center, as shown in Table 6. In addition, five operating azimuth angles of the azimuth thrusters were considered in the numerical analysis: 0°, 45°, 60°, 75°, and 110°.

Similar to Fig. 10, Fig. 12 shows the force in the X direction ( $F_{x\_Hull}$ ) and the force in the Y direction ( $F_{y\_Hull}$ ) measured across the entire hull, including the thruster, when the model azimuth thrusters located independently at the port and center operates in each azimuth direction under different boundary conditions and the resulting force ( $F_{Total}$ ) is shown according to the operating direction of the propeller. Table 11 lists the specific values. Numerical analysis showed that the force in the X direction ( $F_{x\_Hull}$ ) was similar overall, even though there was a difference in the attachment position of the azimuth thrusters or the method of imposing boundary conditions. On the other hand, for the force in the Y direction ( $F_{y\_Hull}$ ), there was no significant difference according to the attachment position of the azimuth thrusters under the same boundary conditions. On the other hand, even when the azimuth thrusters were installed in the same position, the results showed a large difference according to the imposed boundary conditions method. In particular, in a situation where the Directional\_BC condition was imposed, the magnitude of the force in the Y direction ( $F_{y\_Hull}$ ) applied to the entire target vessel, including the hull and thruster, was reduced compared to the result of the Fixed\_BC condition, and was approximately twice as large under an azimuth angle of 75°. Thus, the distribution of the resulting force ( $F_{Total}$ ) of the entire target vessel according to the azimuth also showed a difference following the boundary condition imposition method. For the Fixed\_BC condition, a constant resulting force was predicted regardless of the attachment position of the

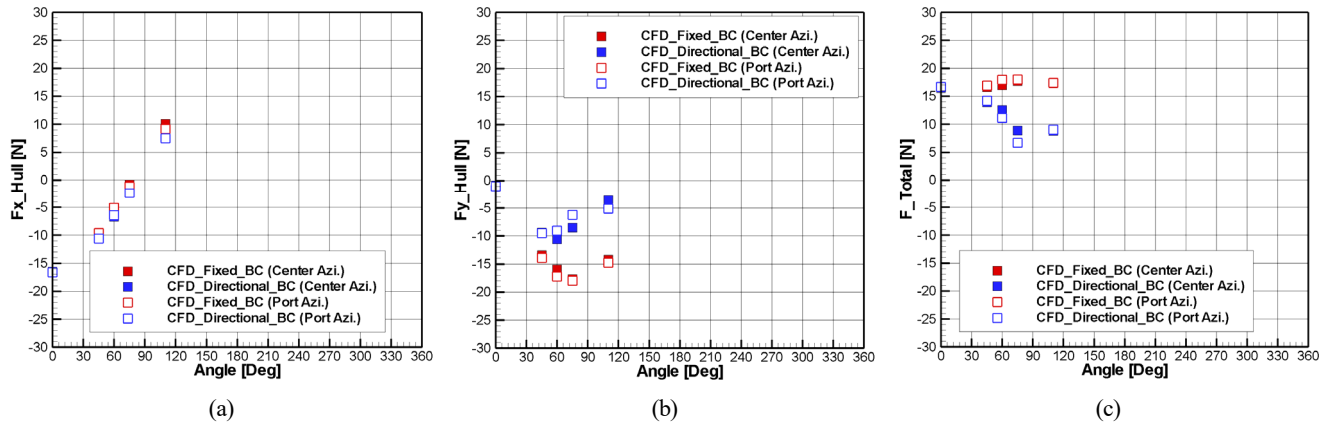


Fig. 12 Comparison of  $F_{X\_Hull}$  (a),  $F_{Y\_Hull}$  (b) and  $F_{Total}$  (c) with respect to azimuth angle from CFD

Table 11 Comparison of  $F_{X\_Hull}$ ,  $F_{Y\_Hull}$  from CFD

Method		CFD					
		Fixed BC			Directional BC		
Azimuth thruster	Azimuth angle	$F_{X\_Hull}$ (N)	$F_{Y\_Hull}$ (N)	$F_{Total}$ (N)	$F_{X\_Hull}$ (N)	$F_{Y\_Hull}$ (N)	$F_{Total}$ (N)
Center	0°	-16.5	-0.9	16.5	-16.5	-0.9	16.5
	45°	-9.8	-13.4	16.6	-10.3	-9.4	13.9
	60°	-5.7	-16.0	16.9	-6.7	-10.6	12.5
	75°	-0.8	-17.7	17.7	-2.4	-8.5	8.8
	110°	10.0	-14.2	17.4	8.0	-3.6	8.8
Port side	0°	-16.6	-1.0	16.7	-16.6	-1.0	16.7
	45°	-9.6	-13.9	16.9	-10.6	-9.5	14.2
	60°	-5.1	-17.2	18.0	-6.4	-9.1	11.1
	75°	-1.2	-18.0	18.0	-2.4	-6.2	6.7
	110°	9.1	-14.8	17.4	7.5	-5.1	9.1

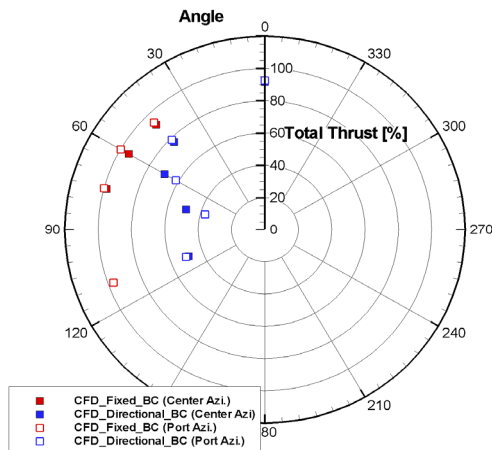


Fig. 13 Normalized total thrust on the azimuth angle

azimuth thruster. In contrast, the overall resulting force ( $F_{Total}$ ) decreased as the azimuth increased for the Directional\_BC condition.

Similar to Fig. 11, Fig. 13 shows the dimensionless thrust loss due to the thruster-hull interference effect according to the operating azimuth of the azimuth thruster located on the port side and the center; the specific values are listed in Table 12. Similar to Fig. 12(c), the dimensionless total thrust distribution also showed different tendencies according to the method of imposing boundary conditions. For the azimuth reviewed in this study, when Fixed\_BC was imposed,

a maximum of approximately 8% of thrust loss was expected to occur. In contrast, when the Directional\_BC condition was imposed, a maximum of approximately 63% of thrust loss was expected. In particular, when the operating azimuth of the azimuth thruster was 45°, the difference in thrust loss according to the boundary condition imposition method was approximately 15%, but under the condition of 60° or more, the difference in thrust loss estimated according to the boundary condition imposition method was steep, where the difference was approximately two times.

Table 12 Comparison of normalized total thrust on the azimuth angle from CFD

Method		CFD	
Azimuth thruster	Azimuth angle	Fixed_BC	Directional_BC
Center	0°	91.7%	91.7%
	45°	92.3%	77.2%
	60°	94.2%	69.5%
	75°	98.4%	49.1%
	110°	96.8%	48.8%
Port side	0°	92.6%	92.6%
	45°	94.0%	79.1%
	60°	99.9%	61.7%
	75°	100.0%	37.2%
	110°	96.6%	50.3%



#### 4. Discussion

Chapter 3 compared the predicted thrust loss according to the boundary condition imposition method based on the two target vessels. As shown in Tables 9 and 11 as a comparison result, the thrust loss differed according to the vessel type. In the case of WTIV, the influence of the imposed boundary condition was relatively small. On the other hand, in the case of FPSO, the influence of the boundary condition was large, and the predicted thrust loss was estimated to be approximately 60%, exceeding the generally known level. This chapter discusses the reasons for the large difference in the estimated thrust loss tendency according to vessel types or boundary conditions.

The directional BC mentioned above was a method in which the velocity-inlet and pressure-outlet conditions were imposed on each side of the computational area according to the azimuth angle of the azimuth thruster. Therefore, from the point of view of the target vessel, it is the same situation as a current flowing at a certain azimuth. An azimuth of  $0^\circ$  corresponds to a situation in which the vessel is going straight, and an azimuth of  $90^\circ$  means a situation in which the current flows from the port side of the vessel to the starboard side. The actual vessels generate load according to the direction of the current, which is called the current load. This study conducted a separate numerical analysis to obtain the load. Tables 13 and 14 show the  $C_x$ ,  $C_y$ , and the resulting force ( $C_{Total}$ ) for the target vessels, WTIV and FPSO, by classifying the current loads according to each azimuth in the X and Y directions. At this stage, the applied flow rate was the flow rate when the advance ratio was defined as 0.05, and the own current load of the vessel was calculated without the azimuth thruster attached. Fig. 14 shows the total dimensionless loads calculated for each azimuth based on the value of the resultant force ( $C_{Total}$ ) of the current load when the azimuth is  $0^\circ$  in each target vessel are shown together. As shown in Tables 13 and 14 and Fig. 14, the degree of increase in load varied greatly depending on the vessel type. In the case of WTIV, based on the resulting force ( $C_{Total}$ ), when the azimuth was  $0^\circ$ , it increased to approximately four times when the azimuth was  $90^\circ$ . On the other hand, in the case of the FPSO, based on the resulting force ( $C_{Total}$ ) when the azimuth was  $0^\circ$ , the load value was up to approximately 20 times greater when the azimuth was  $75^\circ$ . Moreover, the size of the load value itself according to the direction of the current also showed a large difference depending on the type of vessel. It was shown that FPSO is approximately 10 times larger than WTIV. These results showed that even if the azimuth thruster attached to the target vessel constantly calculates the thrust during numerical analysis. The total thrust ( $F_{Total}$ ) effective for the vessel is greatly reduced as the current load of the vessel becomes excessively large. In particular, the magnitude of the current load may vary greatly according to the vessel characteristics, e.g., the vessel type, hull shape, appendage, and draft. Fig. 15 shows the distribution of the dimensionless pressure coefficient of the hull calculated under the condition of the current at the  $45^\circ$  azimuth from the port side of each target vessel. The distribution form has different characteristics depending on the target

vessel. Therefore, when performing numerical analysis to predict thrust loss due to thruster-hull mutual interference, Fixed\_BC can be imposed on the side of the computational area rather than Directional\_BC, which unnecessarily causes a large current load of the target vessel to be induced and unrealistically large thrust loss to be estimated. When Fixed\_BC is imposed, a corresponding flow rate with a small advance ratio artificially defined for numerical stability was additionally imposed, and the effect of the current load can be minimized because this flow rate was very low. As shown in Table 10, when the target vessel is WTIV, the loss of thrust estimated through numerical analysis matches well with the model test results. Even when the target vessel is FPSO, the thrust loss according to the azimuth was estimated to be within 10% regardless of the attachment position of the azimuth thruster, as shown in Table 12. Moreover, when Fixed\_BC was imposed as a boundary condition, FPSO, one of

**Table 13** Current load with respect to azimuthing angle on WTIV

Angle	$C_x$ (N)	$C_y$ (N)	$C_{Total}$ (N)	[%]
$0^\circ$	0.064	0.000	0.064	100
$45^\circ$	0.056	0.149	0.159	250
$90^\circ$	0.003	0.241	0.241	378
$135^\circ$	-0.061	0.152	0.164	258
$180^\circ$	-0.069	0.000	0.069	109
$225^\circ$	-0.060	-0.152	0.163	256
$270^\circ$	0.003	-0.241	0.241	380

**Table 14** Current load with respect to the azimuth angle on FPSO

Angle	$C_x$ (N)	$C_y$ (N)	$C_{Total}$ (N)	(%)
$0^\circ$	0.532	0.000	0.532	100
$45^\circ$	0.396	4.959	4.975	935
$60^\circ$	-0.119	8.207	8.208	1,543
$75^\circ$	-0.862	10.673	10.708	2,013
$110^\circ$	0.329	9.760	9.765	1,836

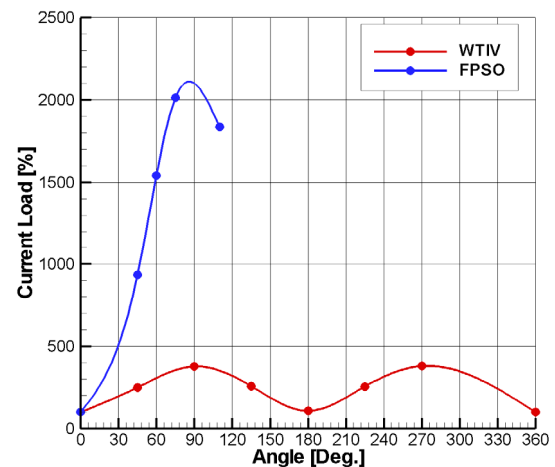


**Fig. 14** Comparison of the normalized current load with respect to the azimuth angle on WTIV and FPSO

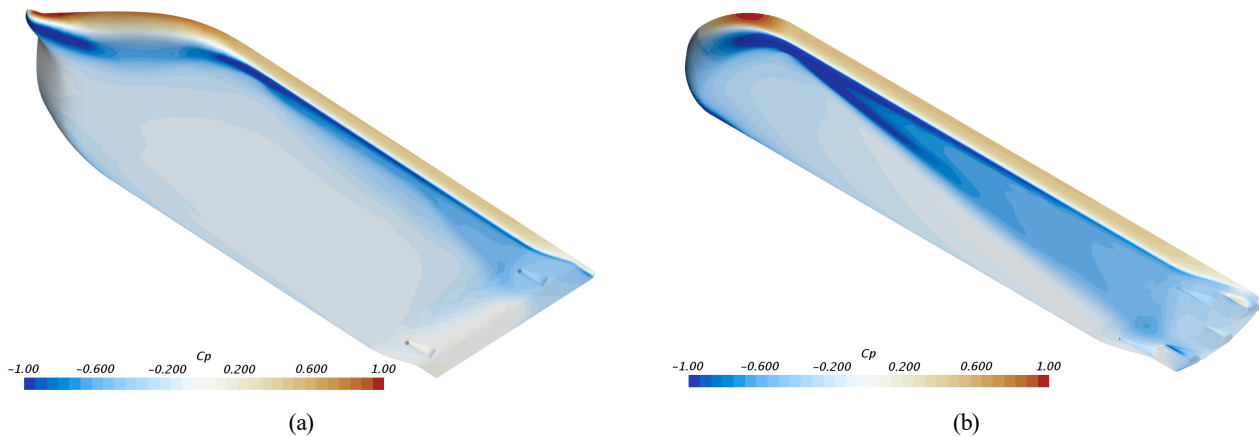


**Fig. 15** Distribution of pressure coefficient on 45° current condition (a) WTIV, (b) FPSO

the target vessels, was predicted to have relatively less thrust loss than the other target vessel, WTIV. The causes are as follows. The azimuth thruster was installed at the lower part of the head box protruding downward from the hull, so the distance from the hull was relatively far. Second, the duct of the azimuth thruster applied in this study rotated downward (tilt), which can reduce the Coanda effect. Third, the optimal arrangement of azimuth thruster that minimizes interference between the wake direction of the azimuth thruster and the hull, the selection of an azimuth thruster with appropriate capacity, and the advancement of DP control algorithms are fundamentally needed to prevent excessive thrust loss due to thruster-hull mutual interference in offshore facilities or special vessels.

## 5. Conclusion

The thrust loss due to thruster-hull mutual interference was estimated using the numerical analysis method. Different boundary conditions were imposed based on the two target vessels, and the predicted thrust loss was compared. Through this, the following conclusions could be drawn.

(1) When estimating the thrust loss due to thruster-hull interference by the numerical analysis, it is practical to impose inflow conditions and pressure outflow conditions in the computational domains in the bow and stern directions, such as the boundary condition at 0° azimuth. On the other hand, if the velocity inflow condition and the pressure outflow condition are imposed according to the direction of the operating direction of the azimuth thruster, an unintended current load of the hull may occur, which results in excessive thrust loss may be excessively predicted.

(2) Even if the aforementioned boundary conditions were imposed during the numerical analysis, the thrust loss due to the thruster-hull interference effect can show a difference depending on the vessel type, hull shape, various appendages, and arrangement of the azimuth thruster. In the case of the WTIV, a thrust loss of approximately 30% was expected. On the other hand, in the case of the FPSO, a thrust loss of less than 10% was expected at the azimuth angle of the azimuth thruster considered, and the differences in the azimuth thruster

attachment position (port or center of the vessel) were up to approximately 5%.

The foreseeable areas that require additional research include securing additional verification data through model tests, considering the motion performance of the target vessel, and estimating the interference effect between the thruster and the free surface in the case of a vessel with a small draft.

## Conflict of Interest

The authors declare that they have no conflict of interests.

## Funding

This thesis is research conducted with the support of the Korea Institute of Energy Technology Evaluation and Planning with financial resources from the government (Ministry of Trade, Industry, and Energy) in 2021 (No. 20213030020200, Development of an integrated load analysis program for floating offshore wind power systems).

## References

- Cozijn, H. Hallmann, R., & Koop, A. (2010). Analysis of the velocities in the wake of an azimuth thruster, using PIV measurements and CFD calculations. In *Dynamic Positioning Conference, Houston, USA*.
- Dang, J., & Laheij, H. (2004). Hydrodynamic aspects of steerable thrusters. In *Dynamic Positioning Conference, Houston, USA*.
- Funeno, I. (2009). Hydrodynamic optimal design of ducted azimuth thrusters. In *First International Symposium on Marine Propulsion, SMP09, Trondheim, Norway*.
- Lehn, E. (1980). *Thruster interaction effect* (NSFI Report-102.80). The Ship Research Institute of Norway.
- Nienhuis, U. (1992). *Analysis of thruster effectivity for dynamic positioning and low speed manoeuvring* [Doctoral dissertation, Technical University Delft].
- Ottens, H., van Dijk, R., Meskers, G. (2011). Benchmark study on

- thruster-hull interaction on a semi-submergible crane vessel. *Proceedings of the ASME 2011 30th International Conference on Ocean, Offshore and Arctic Engineering, Rotterdam, Netherlands*, 297–307. <https://doi.org/10.1115/OMAE2011-49433>
- Palm, M., Jurgens, D. & Bendl, D. (2010). Comparison of thruster axis tilting versus nozzle tilting on the propeller-hull interactions for a drillship at DP-condition. In *Dynamic Positioning Conference, Houston, USA*.
- Song, G. S., Kim, H. J., Park, H. G., Seo, J. S. (2013). The investigation for interaction phenomenon of azimuth thruster on ship. *Proceedings of the PRADS2013, Changwon, Korea*.
- Song, G. S., Kim, J. S., & Kim, H. J. (2022). The study of thrust loss by thruster-hull interaction on azimuth thruster. *Proceedings of the 12<sup>th</sup> National Congress on Fluids Engineering, Changwon, Korea*.

### Author ORCIDs

Author name	ORCID
Song, Gi Su	0000-0002-5424-4794
Lee, Seung Jae	0000-0001-8992-6915
Kim, Ju Sung	0000-0003-4719-4167

# Numerical Investigation of Countermeasure Effects on Overland Flow Hydrodynamic and Force Mitigation in Coastal Communities

Hai Van Dang<sup>1</sup>, Sungwon Shin<sup>2</sup>, Eunju Lee<sup>1</sup>, Hyoungsu Park<sup>3</sup> and Jun-Nyeong Park<sup>1</sup>

<sup>1</sup>Graduated Student, Department of Marine Science and Convergent Technology, Hanyang University ERICA, Ansan, Korea

<sup>2</sup>Professor, Department of Marine Science and Convergent Technology, Hanyang University ERICA, Ansan, Korea

<sup>3</sup>Assistant Professor, Department of Civil and Environmental Engineering, University of Hawaii at Manoa, US

**KEY WORDS:** Numerical simulation, Overland flow, Flooding mitigation structures, Hydrodynamic and force reduction, Tsunami

**ABSTRACT:** Coastal communities have been vulnerable to extreme coastal flooding induced by hurricanes and tsunamis. Many studies solely focused on the overland flow hydrodynamic and loading mechanisms on individual inland structures or buildings. Only a few studies have investigated the effects of flooding mitigation measures to protect the coastal communities represented through a complex series of building arrays. This study numerically examined the performance of flood-mitigation measures from tsunami-like wave-induced overland flows. A computational fluid dynamic model was utilized to investigate the performance of mitigation structures such as submerged breakwaters and seawalls in reducing resultant forces on a series of building arrays. This study considered the effects of incident wave heights and four geometrically structural factors: the freeboard, crest width of submerged breakwaters, and the height and location of seawalls. The results showed that prevention structures reduced inundation flow depths, velocities, and maximum forces in the inland environment. The results also indicated that increasing the seawall height or reducing the freeboard of a submerged breakwater significantly reduces the maximum horizontal forces, especially in the first row of buildings. However, installing a low-lying seawall closer to the building rows amplifies the maximum forces compared to the original seawall at the shoreline.

## 1. Introduction

The past few decades witnessed rapid population and socioeconomic development in coastal areas. However, low-lying coastal regions have been prone to extreme surges and high waves during hurricanes and tsunami events (Sun et al., 2020). Sweet et al. (2017) reported that the frequency and intensity of hazard events have increased significantly due to climate change, causing low-land areas to face unforeseeable damage. For instance, Hurricane Katrina (2005) resulted in destruction and severe damage to 133,000 houses in only the Mississippi area (Eamon et al., 2007). Hurricane Harvey (2017) severely damaged over 200,000 homes and businesses and induced massive rainfall that displaced over 30,000 people (Aghababaei et al., 2018). Significantly, the 2011 Japan earthquake-induced tsunami ( $M_w = 9$ ) damaged most countermeasures along the coasts and inundated further inland areas, ultimately causing a massive loss of approximately 15,844 human lives, 128,753 destroyed houses, and

245,376 partially destroyed houses (Aarup et al., 2012). Therefore, investigating mechanisms of overland flow driven by large waves and high surge levels in coastal regions is of great importance for minimizing its impacts and enhancing the resilience of coastal communities.

The hydrodynamic characteristics of coastal communities under inundation flow impacts have caused extensive concern over the last decade. Several previous studies have been conducted to investigate the flow patterns surrounding buildings under overland flow impacts. Park et al. (2013) used a 1:50 scaled physical model to represent an idealized coastal community in Seaside, Oregon. This study experimentally investigated the transformation of free surface elevation, velocity, and momentum flux in the built environment and compared them with the results of numerical modeling. Qin et al. (2018) performed a high-resolution computational fluid dynamics (CFD) model based on OpenFOAM to simulate the tsunami inundation in an idealization of Seaside, Oregon, which was validated

Received 24 October 2022, revised 28 November 2022, accepted 1 December 2022

Corresponding author Sungwon Shin: +82-31-400-5533, [sungwshin@hanyang.ac.kr](mailto:sungwshin@hanyang.ac.kr)

It is a recommended paper from the proceedings of 2022 spring symposium of the Korea Association of Ocean Science and Technology Societies (Dang et al., 2022).

© 2022, The Korean Society of Ocean Engineers

This is an open access article distributed under the terms of the creative commons attribution non-commercial license (<http://creativecommons.org/licenses/by-nc/4.0>) which permits unrestricted non-commercial use, distribution, and reproduction in any medium, provided the original work is properly cited.

using the experimental dataset from Park et al. (2013). The study pointed out the importance of considering the built environment in predicting forces on inland buildings rather than the traditional method by considering drag coefficients (with a recommended value of 2.0). Ishii et al. (2021) performed experimental and numerical investigations on the effects of different building arrangements on tsunami-induced overland flow hydrodynamics and the performance of shielding effects of macro-roughness on the lee side of the buildings. Moreover, Moris et al. (2021) examined the influence of the number of building rows providing shelter on inundation depth, velocity, and loading mitigation in coastal communities. This study indicated that maximum forces significantly decreased by four times when a tsunami propagated in the five most seaward building rows, but a slight decrease was observed from the fifth to the last building row.

Sogut et al. (2019) conducted a laboratory experiment and large-eddy simulation (LES) numerical model to quantify the effects of varied building layouts, including straight, staggered, and single building rows on solitary wave-generated flow hydrodynamics and maximum forces. Staggered layouts amplified maximum forces measured on the front face of buildings in the back row by 30% and 60% compared to only single row and straight layouts. Building rows spaced straightly had the most effective sheltering performance for the force mitigation in the back row (Sogut et al., 2019). Sogut et al. (2021) also investigated the interaction between solitary waves and a series of building arrays by considering the effects of following and opposing steady currents.

Kihara et al. (2021) conducted large-scale experiments with complex topography to represent an idealized coastal industrial site under tsunami-like waves with and without soliton fission. This study indicates that the blocking effects induced by macro-roughness significantly impact maximum inundation depth and suggests a relationship between the pressure and neighboring inundation depths. Generally, the previous experimental and numerical studies focused on understanding flow patterns in coastal communities under extreme overland flows without any mitigation measures. However, several flooding countermeasures are constructed and serve as the first barriers protecting coastal communities on natural coasts, which may influence the mechanisms of overland flow impacts in coastal communities. Therefore, considering the effects of mitigation structures on inundation flow characteristics and loadings on a series of building arrays is essential to provide helpful information for design standards and coastal community resilience planning.

A seawall is one of the most effective mitigation measures constructed worldwide against severe inundation events in residential coastal communities. Field observation was conducted after the Thailand tsunami (2004), and it was reported that houses protected by seawalls experienced minor damage compared to those without protection (Lukkunaprasit and Ruangrassamee, 2008). Oshnack et al. (2009) performed a laboratory experiment to investigate the performance of a seawall at different heights on tsunami bores-induced loadings on the back of a vertical rigid wall. Thomas and Cox (2012)

investigated the heights and positions of a finite-length seawall to mitigate tsunami-like wave forces on buildings. The finding shows that increasing seawall heights significantly reduced the runup height, maximum and averaged force with a percent reduction of up to 90% on vertical coastal buildings. Rahman et al. (2014) simultaneously investigated the effects of heights and positions of perforated and solid seawalls on force reduction. The study shows that the maximum force reduction was 41% when installing a higher seawall closer to the building model.

The previous studies reveal that an increase in seawall height is consistent with an increase in the force reduction. However, due to the financial investment or aesthetic issues along shorelines, the seawall height has been typically designed as lower than the overtopping heights generated by unusual events such as storms, hurricanes, and tsunamis (Raby et al., 2015). This limitation makes low-lying areas more vulnerable to extreme coastal flooding events. Thus, additional retrofitting structures may be helpful in maintaining the performance of existing seawalls against extreme overland flows. This study proposes an offshore submerged breakwater as an adaptation solution to lower the seawall height while enabling coastal communities to achieve expected protective levels. The submerged breakwater is a low-cost, environmentally friendly, and aesthetic structure that can effectively dissipate wave energies and alleviate damages from extreme events (Li and Zhang, 2019; Lee and Shin, 2011).

The objective of this study is to investigate the performance of a seawall and a submerged breakwater on hydrodynamics and loadings applied to a series of coastal building rows in coastal communities under overland flow caused by tsunami-like waves through a quantitative CFD model, *olaFlow* (Higuera et al., 2015). *OlaFlow* is developed based on an open-source flow solver, *OpenFOAM*, which was validated by a large-scale experimental dataset. The effect of a seawall and submerged breakwater on the force, velocity, and flow depth attenuation in a built environment was systematically analyzed by considering five prominent factors: incident wave heights, the height and position of seawalls, and the crest width and freeboard of submerged breakwaters.

Section 2 briefly describes the laboratory experiment setup, which was used for numerical validation. Section 3 introduces the *OpenFOAM*-based *olaFlow* model setup and presents the performance of a numerical model through verification with the laboratory data. The flow patterns and loading reduction in the building arrays defended by those mitigation measures are discussed in Section 4. Finally, Section 5 presents conclusions and points out limitations for further research.

## 2. Large-Scale Experimental Setup

A large-scale experiment was carried out in a Directional Wave Basin (DWB) at Oregon State University, USA. The wave basin is 48.8 m in height, 26.5 m in width, and 2.1 m in depth and has a piston-type wavemaker with 29 paddles. The hydraulic tests were

designed with a 1:20 length scale relative to the prototype scale. The bathymetry profile was composed of an 11.7-m flat concrete bottom followed by a uniform 1:20 sloping section and a 10-m elevated horizontal platform (Fig. 1). A wooden submerged breakwater was spaced in the slope section at  $x = 24.448$  m, and a full-length seawall was located at  $x = 31.7$  m in the elevated horizontal berm at  $z = +1.0$  m. The trapezoidal submerged breakwater has a crest width ( $W_B$ ) of 0.676 m, a 1:1 slope on both sides, and a freeboard ( $h_F$ ) of 0.064 m relative to the specific still water level ( $d = 0.98$  m). The rectangular seawall was designed with a cross-section of  $0.12 \text{ m} \times 0.036 \text{ m}$ .

100 building units of  $0.4 \text{ m} \times 0.4 \text{ m} \times 0.4 \text{ m}$  were installed to represent macro-roughness elements, which were organized into  $10 \times 10$  straight building rows. Individual building models were spaced at 1.0 m in the alongshore direction and 0.8 m in the cross-shore direction (center to center). The horizontal distance from the most seaward building row to the beginning of the elevated inland section ( $L_{sh}$ ) was 1.6 m, and the full length of the idealized landward coastal area ( $L$ ) was 10 m. A detailed description of bathymetry is available from Moris et al. (2021) because previous studies also used the same bathymetry.

Fig. 1 shows detailed information on instrumentation used in the experiment. Wave gauges (WGs), ultrasonic wave gauges (USWGs), acoustic Doppler velocimeters (ADV), pressure gauges (PGs), and horizontal load cells (LCs) were utilized to record incident water surface elevations, inland inundation depths, velocities, pressures, and forces in the built environment, respectively. Moreover, a six-degree-of-freedom loadcell was used in the building model in the most seaward building row to measure both forces and moments in three directions. Nine WGs were used to record the transformation of

incident water surface elevations over the sloping beach. WGs 1, 2, and 3 were installed at the same cross-shore distance  $x = 14.052$  m, while WGs 8 and 9 were at  $x = 19.246$  m away from the wavemaker at the zeroed position.

In the elevated flat section, USWGs 1, 5, 6, and 7 and ADVs 1, 5, 6, and 7 were installed in similar positions to measure flow depths and velocities when waves inundated the coastal communities. USWGs 1, 5, and 7 and ADVs 1, 5, and 7 were co-located in center side streets and spaced 0.1 m in the seaward from the first, third, and fifth building rows, respectively. USWG8 was positioned 0.1 m seaward from the tenth building row to examine the inundation depth at the end of the inland section.

The sampling frequency for water surface elevation and velocity data measured by ADVs, WGs, and USWGs was 100 Hz. Twelve PGs, a 6DOF loadcell, and five LCs were used in eight building elements in the built environment (Fig. 1(a)). Six sensors were installed with a spacing of 0.04 m in the centerline of the front face of an aluminum building to measure transient-wave-induced pressures in the first building row. In addition, five horizontal LCs were set up in the five most seaward building arrays to capture the variation of horizontal forces in the built environment (Fig. 1(a)). The 6DOF loadcell, LCs, and PGs recorded data at a sampling frequency of 1000 Hz. Dang et al. (2022) described the physical instrumentation used for numerical verification in this study in more detail.

Conventionally, a solitary wave is used to simulate tsunami-like waves; however, it underestimates overflow loadings on coastal communities due to the limited wavelengths and periods compared to the prototype model (Thomas and Cox, 2012). Therefore, tsunami-like waves were generated using the error function technique, which

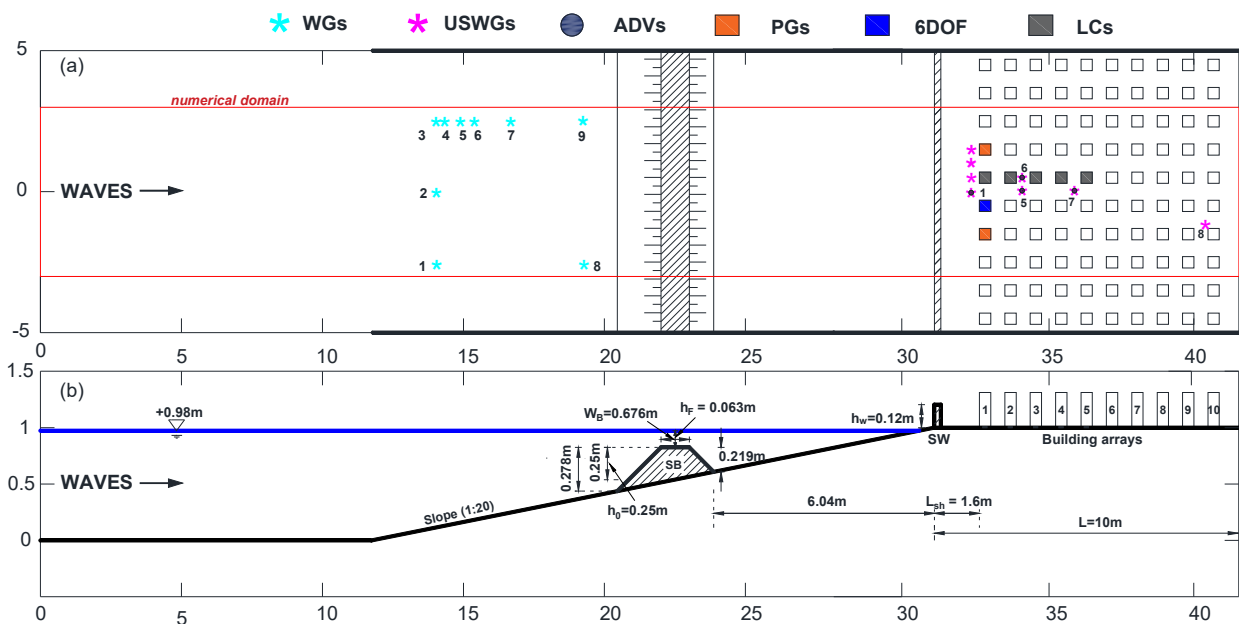


**Fig. 1** Schematic of the overland flow experiment: (a) plan view illustrating the combined structural configuration and instrumentation, including wave gauges (WGs - cyan pentagram), ultrasonic wave gauges (USWGs - magenta pentagrams), acoustic doppler velocimeters (ADV - black circle), inline loadcells (LCs - gray squares), six-degree-of-freedom loadcell (6DOF - blue square), pressure gauges (PGs - orange squares); (b) elevated view for a water level ( $d$ ) of 0.98 m (figure not to scale).



**Table 1** Water depth and wave conditions

Wave cases	Water depth $d$ (m)	Scale factor $S_f$ (s)	Wave amplitude $A$ (m)	Relative amplitude $A/d$
1	0.98	2.0	0.21	0.213
2	0.98	2.5	0.17	0.174
3	0.98	3.0	0.14	0.143
4	0.98	4.0	0.11	0.112

modifies the solitary wave method by using the time series of the error function in controlling paddle displacement. The history of wavemaker displacement  $x(t)$  can be defined as:

$$x(t) = 1 + \operatorname{erf}(t/S_f - 2.871) \quad (1)$$

in which  $t$  is time, and  $S_f$  is a scale factor expressed as time used to control how quickly the paddle moves over a full 2-m stroke (Moris et al., 2021). A lower scale factor generates a larger tsunami height. For this study, scale factors were selected as  $S_f = 2.0$  s, 2.5 s, 3.0 s, and 4.0 s corresponding to incident wave amplitudes of 0.21 m, 0.17 m, 0.14 m, and 0.11 m, respectively. The still water level ( $d$ ) in front of the wavemaker at the initial flat section was 0.98 m. Table 1 shows the wave conditions used in this study. In addition, the experiment was carried out with varying configurations: with a submerged breakwater only (SB), with a seawall only (SW), with a combined seawall and submerged breakwater (SWSB), and baseline conditions (without mitigation alternatives) under four wave conditions.

### 3. Numerical Model

For a deeper understanding of flow patterns and force mitigations in an idealized coastal area protected by varying structural configurations, this study performed computational simulations based on the olaFlow model, an enhanced version of IHFOAM model (Higuera et al., 2015) that was written in the platform Open-Source Fields Operation and Manipulation (OpenFOAM). OlaFlow uses the finite volume method (FVM) for spatial discretization and solves Reynolds averaged Navier-Stokes (RANS) equations for incompressible flows by using a PIMPLE algorithm (a mixture of the pressure implicit with splitting of operators (PISO) and semi-implicit method for pressure linked equations (SIMPLE)) (Park et al., 2017). The volume of fluid (VOF) approach was used to track the free surface displacement from water-air phases (Ishii et al., 2021). To model the turbulence, the  $k$  solver was selected for the current simulation because this turbulence closure solver is more effective than other turbulent closure solvers (e.g.,  $k-\epsilon$  model) in modeling partially separated flows when the overland flow propagates and then is separated by building rows in the constructed environment (Qin et al., 2018). In addition, olaFlow provides several options for wave generation and absorption, enabling the numerical model to replicate wave characteristics in a physical laboratory (Moris et al., 2021). A detailed explanation of the olaFlow

solver is on the olaFlow website (<https://olafloflow.github.io/>).

#### 3.1 Numerical Model Setup

To save computational resources and guarantee agreement between physical and numerical results, the boundary of the numerical tank was reduced slightly from 10 m to 6 m in the  $y$ -direction, which was enclosed by the solid red line in Fig. 1(a). However, the numerical tank in the  $x$ - and  $z$ -directions remained unchanged. In the numerical model, 10 building rows were also installed in the elevated flat section, but the number of buildings per building row was decreased from 6 buildings in the first four rows to 2 buildings in the most landward rows (Fig. 2). The boundary conditions of the numerical model were set up as follows. We assigned the bottom profiles and structures as wall functions with no-slip boundary conditions and considered slip boundary conditions for lateral walls of the 6-m-wide numerical domain. The top boundary was modeled as the atmosphere. The tsunami-like wave-induced overland flow was modeled using the piston-type wavemaker boundary (inlet) provided in olaFlow. The measured time series of water surface elevations (measured from wave gauges at the experimental wavemaker) and velocities (calculated based on wavemaker displacement data) were utilized for wave input in the numerical inlet to replicate the incident tsunami-like waves.

To achieve convergence of the spatial discretization, coarse (G1), medium (G2), and fine grid (G3) mesh conditions were utilized for model validation. Each mesh size is variable depending on the location of the wave basin. The finer mesh size was set up near the onset of an elevated landward area and building arrays. Fig. 2 illustrates the side and top views of the numerical model indicating the detailed information on the fine mesh (G3), in which  $dx$ ,  $dy$ , and  $dz$  are the grid sizes in the  $x$ ,  $y$ , and  $z$  directions, respectively. In the G3 condition, the mesh size was  $0.1 \text{ m} \times 0.05 \text{ m} \times 0.05 \text{ m}$  (length  $\times$  width  $\times$  height) at the flat section near the wavemaker. This size was gradually refined to the smallest mesh size of  $0.02 \text{ m} \times 0.02 \text{ m} \times 0.01 \text{ m}$  in the region near the start of the elevated flat section, in which strong nonlinear wave deformation induced by wave breaking was observed. Regarding the G1 and G2 conditions, the smallest mesh sizes were 0.04 m and 0.08 m in all directions near the onset of the landward section and reached a maximum of 0.2 m near the wavemaker.

It is noteworthy that all mesh sizes described above were structured sizes (blockMesh tool) of the box-type boundary. However, meshes for the 1:20 sloping section and elevated landward area section were also created by an unstructured mesh generator (snappyHexMesh tool), making mesh cell sizes near the structures smaller than the corresponding cells in blockMesh. The unstructured mesh tool further divided cells in the regions with an intersection between structures and boundary domains (such as buildings, seawalls, and submerged breakwaters).

The cells of intersect region were divided by half, meaning that each blockMesh cell became eight smaller cells. The total number of grid cells in G3 was approximately 9.5 million, which increased by 3 and 10 times from the G1 and G2 conditions. An individual case was computed with a tower server with 24-core parallel processors and

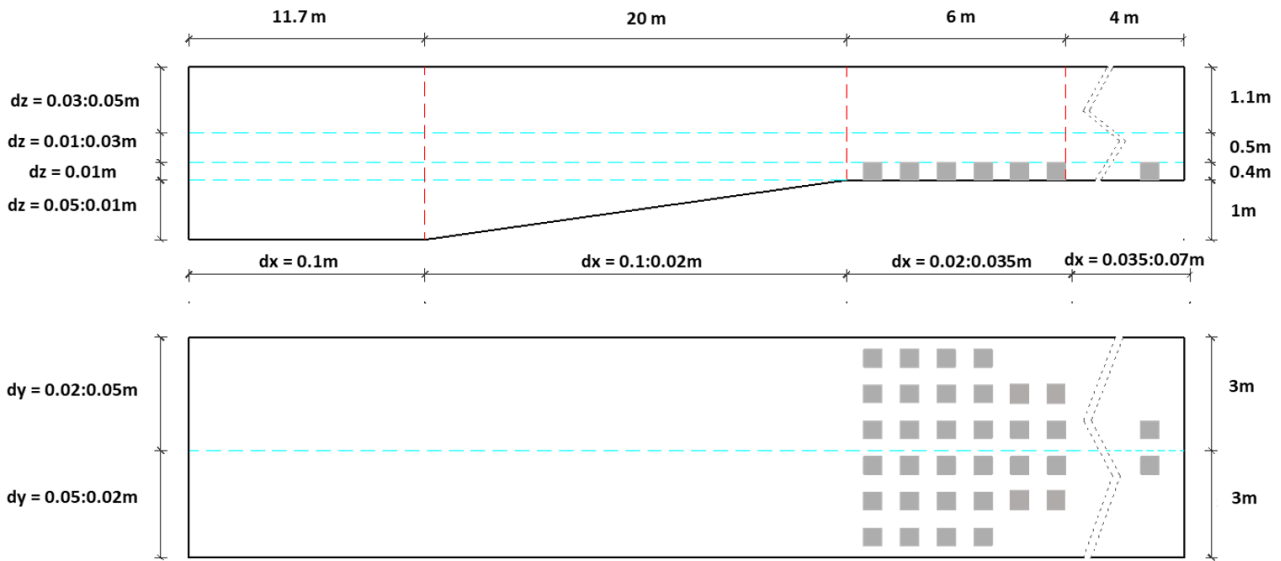


**Fig. 2** Cross-shore and top views of fine mesh condition set up (G3).

required average times of 2 hours, 8 hours, and 16 hours for G1, G2 and G3 and all configurations, respectively. The fine mesh condition was the finest mesh used in the convergent test. When the grid size was further refined, the results were not sufficiently improved when we consider the much larger computational expense and time requirements compared to the availability of computational resources.

### 3.2 Numerical Model Validation

The numerical model was validated with the physical experimental results. Overall, the results of the olaFlow model showed good agreement with the measured experimental results despite some minor inconsistencies in velocity and pressure. Fig. 3 shows the comparison between simulated and measured onshore and offshore free surface elevations, cross-shore velocities, and pressures in the combined structural configurations (SWSB) for wave case 1. Figs. 3 (a) and (b) present the time series of offshore water surface elevations at two wave gauges (WG2 and WG9). Simulated elevations for the three mesh size conditions are similar to measured elevations in both durations and peak magnitudes. However, the reflected waves overlapped a part of the incident waves measured at WG9 at  $t = 25.5$  s (Fig. 3(b)).

Figs. 3 (c) and (d) shows a comparison of the time series of measured and simulated flow depths located 0.1 m seaward from the first and third building rows. Although the three mesh-size conditions have slightly different peak flow depths and wider crest widths than measured elevations, the correlation between numerical and experimental results is generally reasonable. While the G1 condition generated a 10% larger peak flow depth compared to the measured one, both G2 and G3 conditions showed approximately a 5% difference for both USWG1 and USWG5.

Good agreement was observed for the cross-shore velocity from numerical data and available data measured by ADV1 and ADV5 in the physical experiment (Figs. 3 (e) and (f)). The missing experimental data is the leading edge of velocities that cannot be captured by ADV1

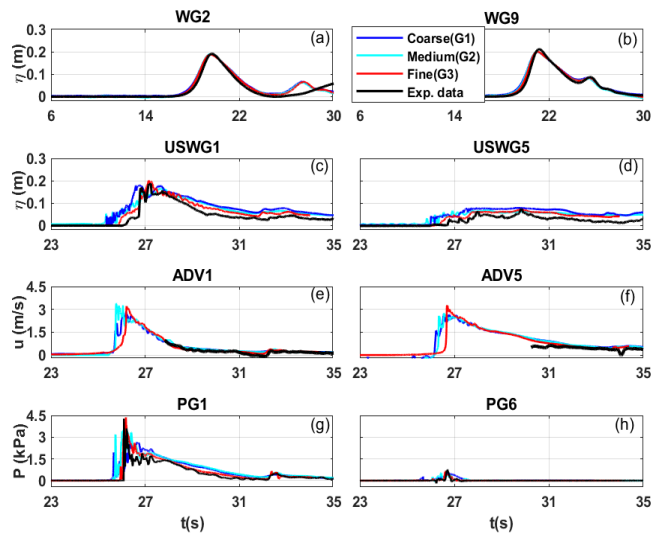


**Fig. 3** Time series of hydrodynamic parameters, including offshore water surface elevations, inland flow depths, cross-shore velocities and pressures between experimental and numerical data in three mesh conditions (coarse, medium, and fine grid sizes).

and ADV5 because the instruments were exposed to air first before the arrival of flows that were too shallow, causing poor data. Figs. 3 (g) and (h) indicate the time series of pressures measured by PG1 and PG6, in which the lowest pressure sensor PG1 was located 0.02 m above the flat bottom, and PG6 was at the highest elevation among the pressure sensors at  $z = +1.26$  m. For PG1, only a 1.3 % difference in maximum pressure was recorded, while the measured and simulated maximum pressures at PG6 were similar in the fine mesh condition (G3).

The current numerical model reproduced the time series of cross-shore wave-induced forces measured on the first five building rows well (Figs. 4 (a)–(e)). The fine mesh condition agreed with the experimental data well except for somewhat complex wave motions. The measured and simulated peak forces had differences of up to 24%



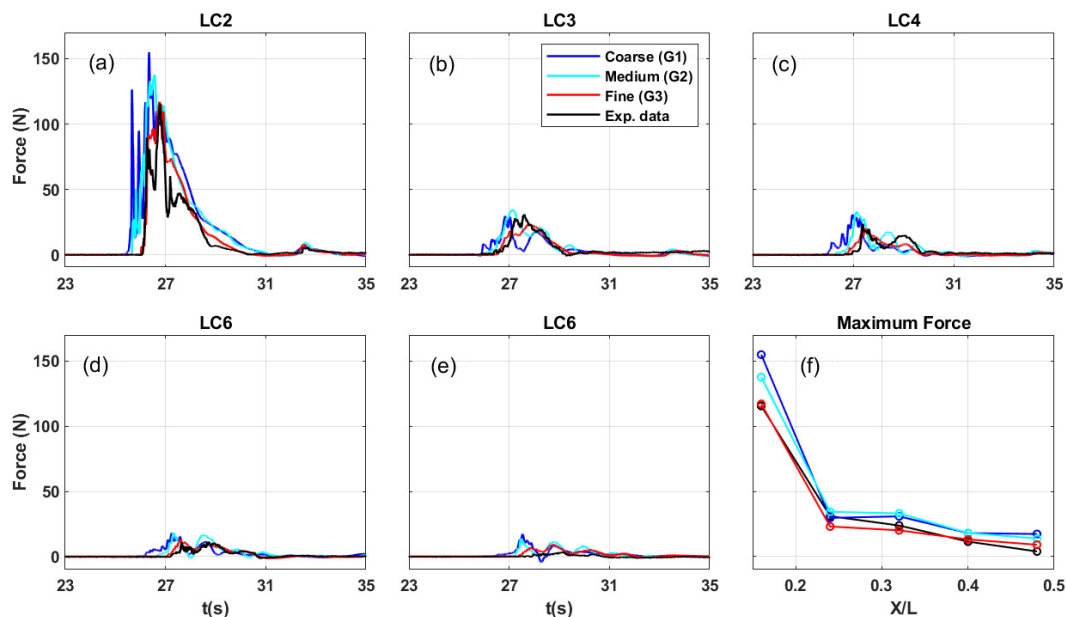


**Fig. 4** Time series of horizontal forces measured in five loadcells installed in the five most seaward building rows and their maximum forces as a function of relative distance  $X/L$ .

and 15% for the G1 and G2 conditions, respectively, but G3 generated only 0.3% larger peak horizontal forces than the measured ones in the first building row (Fig. 4(a)).

Maximum forces measured in the five most seaward building rows as a function of the relative distance  $X/L$  are shown in Fig. 4(f).  $X$  is the distance of each loadcell from the shoreline, and  $L$  is the total length of the idealized coastal constructed environment ( $L = 10$  m). For five building rows, the largest difference between measured and simulated maximum forces was observed in row 2 at less than 20% in the three mesh size conditions, but surprisingly, from row 3 to row 5, an improvement in the agreement between recorded and simulated maximum pressures can be observed with less than 15% difference in the G3 condition. In general, this numerical model effectively replicates the time series of flow depth, velocity, force, and pressure measured in the laboratory experiment.

## 4. Results and Discussion

In this section, a numerical investigation of the mechanism of overland flow propagation in the built environment over different wave conditions is conducted, in which the dimensions and locations of a seawall and submerged breakwater are kept unchanged from those conducted in the laboratory experiment. However, a series of other numerical simulations based on the physical experiment was also carried out to study the effects of geometrical factors and spacing of countermeasures on the performance of flooding mitigation structures in reducing hydrodynamic loads in the built environment. To analyze varying geometrical factors, the tsunami-like wave condition with the largest incident wave amplitude ( $A$ ) of 0.21 m and water level ( $d$ ) of 0.98 m was utilized.

### 4.1 Hydrodynamic Characteristics and Loadings in the Constructed Environment

The complex flow patterns surrounding the building rows in the constructed environment with the installation of only a seawall, only a submerged breakwater, a combined seawall and submerged breakwater, and no protection from the mitigation structures (baseline condition) were simulated and are illustrated in Fig. 5. Dimensions of flooding mitigation structures are the same as those used in the laboratory. The largest intensity of wave conditions with a water level of 0.98 m and an incident wave amplitude of 0.21 m (relative height:  $A/d = 0.213$ ) was selected to investigate the overland flow hydrodynamic characteristics. The time instants were chosen to allow us to compare each configuration's effects on the interaction of overland flows and a series of building arrays. After impinging on the front faces of building rows, overland flows were separated by individual building blocks, inducing jet-type channelized flows with shallower elevations and stronger velocities through the gaps between macro-roughness elements. For over configurations, diffracted waves from two sides of individual blocks directly impacted the sharp edges and merged into the center of each block in the back building rows, which generated runoff on the front face of the back buildings. Soon after runoff waves reached their maximum height, descending runoff in buildings in the back row caused an offshore-directed wave, which was trapped by front and back rows until full dissipation of the wave energy.

Figs. 5 (a) and (b) indicated that flow patterns were symmetric for the baseline and SB configurations, but the SB configuration slightly delayed the arrival time and had more velocity of the inundation flow than the baseline condition. The maximum velocity recorded in the baseline condition was approximately 4 m/s, compared to 2.7 m/s in the SB configuration. Symmetric vortices were formed at the sharp

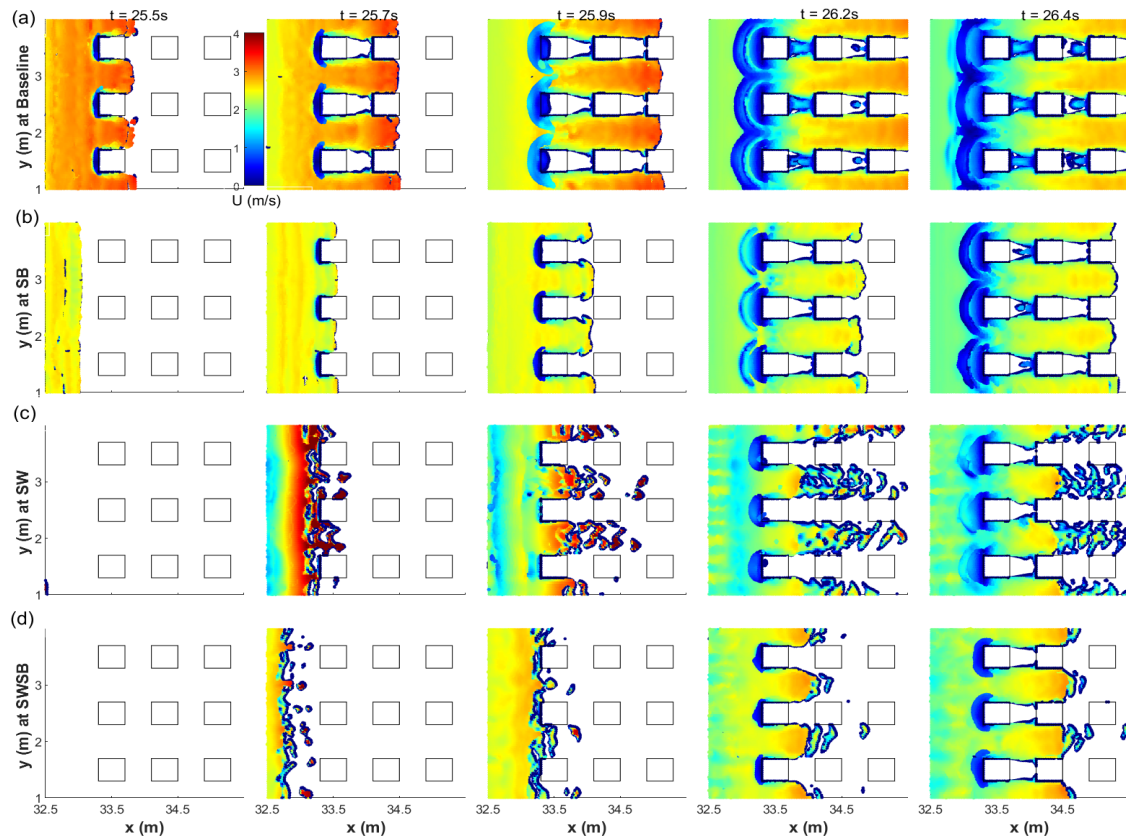


**Fig. 5** Instantaneous simulated surface velocity at time instants  $t = 25.5$  s,  $25.7$  s,  $25.9$  s,  $26.2$  s, and  $26.4$  s for (a) Baseline condition; (b) Submerged breakwater; (c) Seawall; (d) Combined seawall and submerged breakwater configuration.

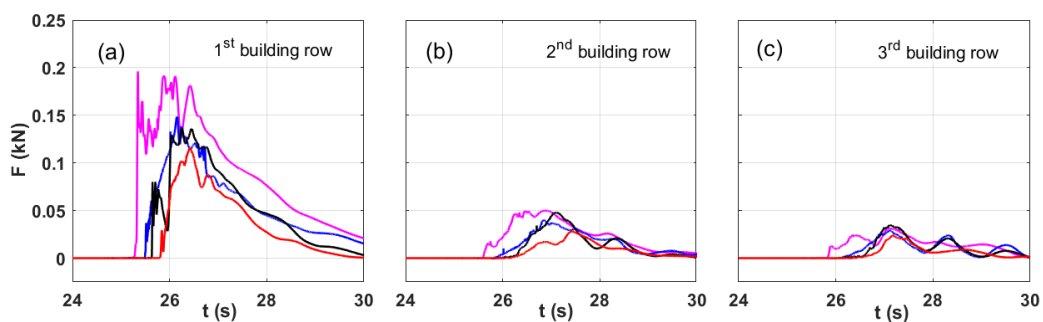


**Fig. 6** Comparisons of time series of forces on the three most seaward building rows for structural configurations and baseline condition.

edges of each individual building block in the two configurations.

Fig. 5(c) illustrates that the seawall induced asymmetric flow patterns due to its large energy dissipation. Water splashes with high velocities were created at the different time instants of  $t = 25.7$  s and  $25.9$  s, but the magnitudes of velocities were significantly reduced when passing the side streets. With the protection of the combined seawall and submerged breakwater countermeasures (SWSB), the tsunami-like wave impacts on the coastal areas were significantly delayed and generated overland flows with lower intensity compared to other configurations. The combined structures dramatically reduced the quantity of overtopped and reflected waves in the front faces of building elements (Fig. 5(d)). Waves impinged the first building row at  $25.9$  s with relatively large wave splashes in the front of the first building row, but the flow was similar to those in the baseline and SB

configurations.

Fig. 6 shows the comparisons of time histories of hydrodynamic forces on the first three building rows in the three structural configurations and the baseline condition. As shown in this figure, the maximum forces measured in structural configurations were significantly lower than the baseline force. The SB and SW configurations induced a relatively similar maximum force in the first building row, which accounted for approximately 75% of the maximum force (25% reduction) in the baseline configuration. In contrast, the maximum baseline force in the first building array was reduced by 38% with both a seawall and submerged breakwater. For the second and third rows, there was an insignificant difference in peak forces for all configurations, but SWSB induced the lowest maximum hydrodynamic forces, which were reduced by about 48% and 38%

relative to the baseline forces, respectively.

#### 4.2 Effects of Incident Wave Heights

This section examines the effects of different incident wave amplitudes on the performance of mitigation structures in reducing maximum flow depths and horizontal forces on the first building rows. Four wave conditions with relative wave ratios were selected:  $A/d = 0.213, 0.174, 0.143, \text{ and } 0.112$ . The water level ( $d$ ) was set at 0.98 m, and the dimensions of mitigation structures were kept unchanged from the experimental sizes described in section 2. Fig. 7 shows the variation of maximum flow depths and horizontal forces in the most seaward building rows for different wave conditions. Generally, the mitigation structures reduced the maximum flow depths and horizontal forces in the four wave conditions. In Fig. 7(a), a significant increase in the flow depth is seen during  $0.112 < A/d < 0.174$ , while there is little change at  $A/d > 0.174$  for structural configurations. As shown in Fig. 7(a), the seawall configuration is better than the submerged breakwater at reducing the flow depth. The SB configuration slightly reduced the maximum flow depths by 5% to 22%, and a significant reduction from 25% to 40% was seen in the SW configuration compared to the baseline condition. The multi-tiered configuration (SWSB) is more effective than these individual configurations at reducing flow depth by a maximum of 64% in the four wave height conditions.

Similar to the flow depth, a linear increase in maximum force recorded at the first building row, as shown in Fig. 7(b). Although the flow depth measured in the SB configuration is higher than in the SW condition, there is an insignificant difference in maximum forces in the two configurations. This happens because the velocity measured in the SW configuration is larger than in the SB configuration (Figs. 5 (b) and (c)). The SB-only and SW-only configurations decreased the horizontal baseline forces from 25% to 58%, respectively. SWSB conditions resulted in larger force reductions by 38% to 84% relative to the baseline at different wave heights.

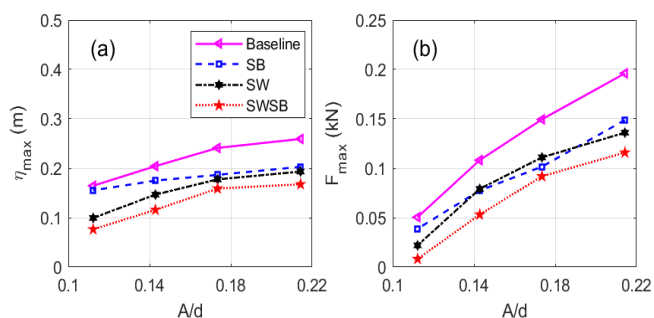


**Fig. 7** Variations of maximum flow depth (a) and horizontal forces (b) measured at the first building row for the four configurations

#### 4.3 Effects of Seawall Heights

The effects of seawall height ( $h_w$ ) on the performance of the seawall in reducing the overland flow-induced loads on a series of building

arrays have been investigated numerically. Four different seawall heights relative to incident wave amplitude were considered:  $h_w/A = 0.6, 0.7, 0.9 \text{ and } 1.0$ . Generally,  $h_w/A$  was less than or equal to 1 for all trials to ensure significant wave overtopping that can impact coastal communities. At a scale of 1:20, the prototype seawall height would be 2.4 to 4.2 m, which is a typical seawall height found along coasts worldwide. Diagrams of velocity contours at different time instants for the lowest seawall configuration ( $h_w/A = 0.6$ ) and the tallest seawall condition ( $h_w/A = 1.0$ ) for both the SW and SWSB configurations are shown in Figs. 8 and 9, respectively. The condition  $h_w/A$  of 0.6 is referred to as the low seawall, and  $h_w/A$  of 1.0 is considered as the tall seawall condition.

The left panels of Fig. 8 shows the water surface elevations corresponding to velocities as a function of cross-shore distances at different time instants for the low seawall condition ( $h_w/A = 0.6$ ), while the right panels of Fig. 8 illustrates the tall seawall condition ( $h_w/A = 1.0$ ) for the SW configuration. The contour data were collected at the cross-section at  $y = 2.5$  m. Firstly, a long wave propagates and starts shoaling at  $t = 24$  s with a steeper and more skewed wavefront along the sloping section, where the maximum velocity was approximately 2.3 m/s. Soon after that, a plunging breaker was generated and characterized by curling wave crests with a high velocity of 3.9 m/s at  $t = 24.5$  s. The snapshots at this time showed that the free surface elevation was entrapped by air, inducing turbulent bores that propagate onshore and then impact the seawall at 25 s.

In the low seawall configuration ( $h_w/A = 0.6$ ), tsunami-like wave overtops the buildings with regions of high velocities, but the tall seawall condition ( $h_w/A = 1.0$ ) induced strong reflected waves at 25.5 s. Runup on a taller seawall may significantly alleviate velocities more than those on the lower seawall. The overland flow inundated the flat area and caused similar runup heights on the front face of the first building row for both configurations at 25.9 s and 26.2 s for the low and tall seawall configurations, respectively. However, the low seawall condition resulted in higher flow depths impinging on the first building rows at  $t = 25.9$  s compared to the thin layer of flow depth for the tall seawall configuration at  $31.7 \text{ m} < x < 33.3$  m. This is attributed to the large amount of wave reflected from the tall seawall and propagated offshore.

Fig. 9 presents the effects of seawall heights in the combined structural configurations (SWSB) on the constructed environment. In the SWSB configurations, the dimensions of the submerged breakwater remain unchanged from the original structure in the laboratory experiment. With the installation of the submerged breakwater, the tsunami-like wave shoals and begins slightly breaking over the top crest of the submerged breakwater at  $t = 24.5$  s. At the initial breaking stage, the broken wave traveled down on the lee side of the submerged breakwater with significant surface elevation reduction to  $-0.015$  m (relative to still water level  $d = 0.98$  m) and velocities increasing to 1.5 m/s. Moreover, the lee side showed a hydraulic jump that disturbed the water level, forming turbulence bores propagating over the sloping section and impulsively impinging

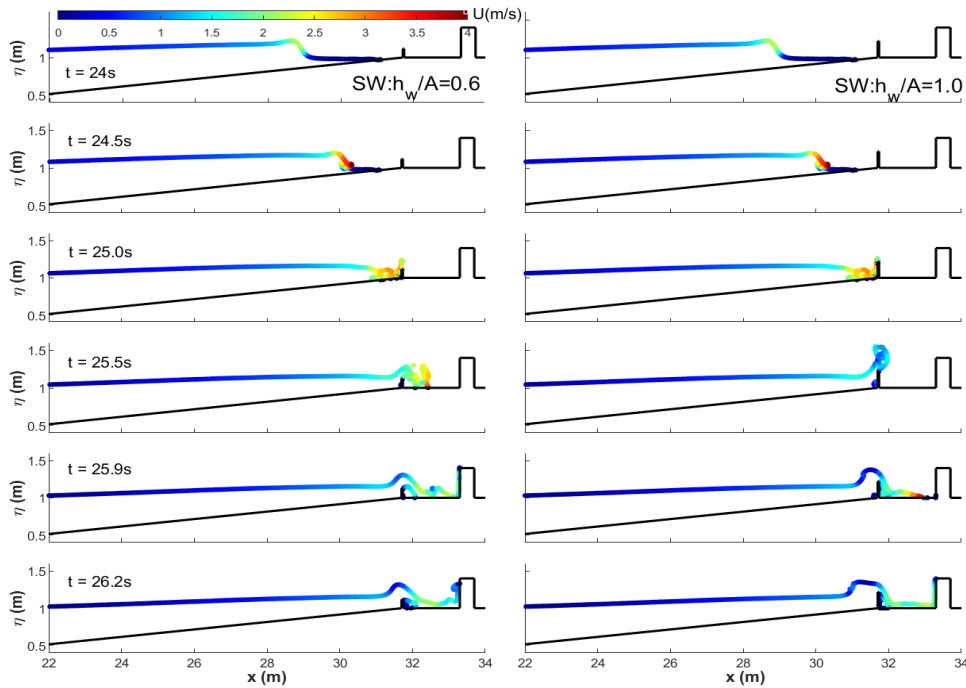


**Fig. 8** Velocity contours at different seawall heights at varied time instants in SW configurations:  $h_w/A = 0.6$  (left panels) and  $h_w/A = 1.0$  (right panels).

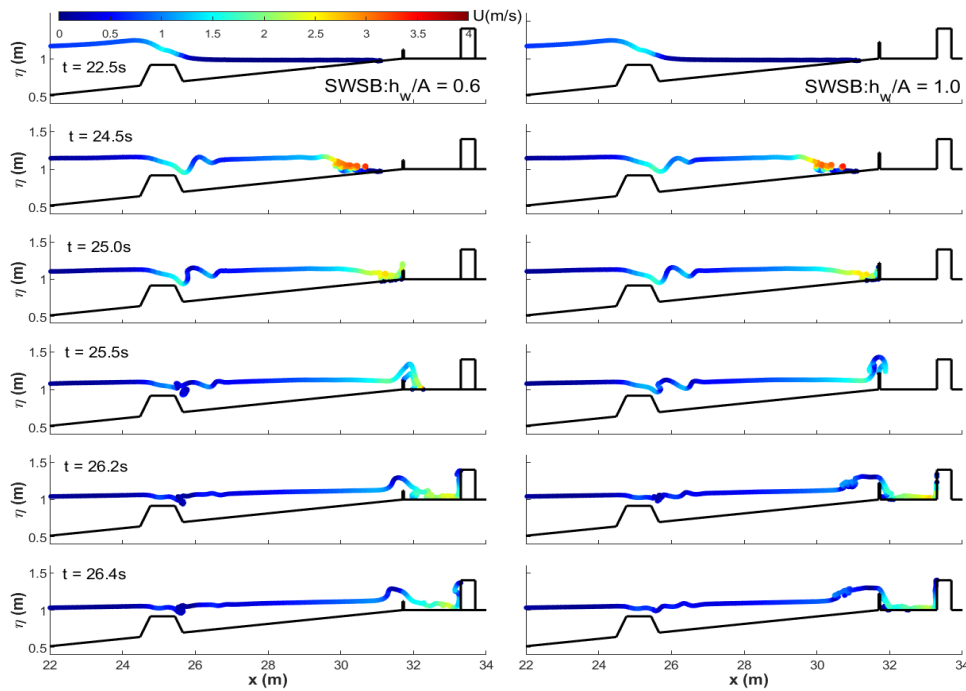


**Fig. 9** Velocity contours at different seawall heights at varied time instants in SWSB configurations:  $h_w/A = 0.6$  (left panels) and  $h_w/A = 1.0$  (right panels).

on the vertical wall.

The submerged breakwater significantly reduced velocities when wave runoff occurred on the seawall at  $t = 25$  s compared to the individual SW configuration in Fig. 9. The SWSB configurations induced similar flow propagation patterns to those in the SW configurations in the elevated inland area. However, the snapshots in Fig. 9 at  $t = 26.2$  s illustrate that the SWSB configurations with low

and tall seawalls resulted in lower flow depths exerted on vertical buildings than those in the SW-only configurations in the inland area.

Fig. 10 presents the maximum forces measured at the five most seaward building rows at different seawall heights for the SW and SWSB configurations as a function of relative distance  $X/L$ .  $X$  is the distance from the shoreline to each building array, and  $L$  is the full cross-shore length of the elevated coastal area ( $L = 10$  m). As shown in

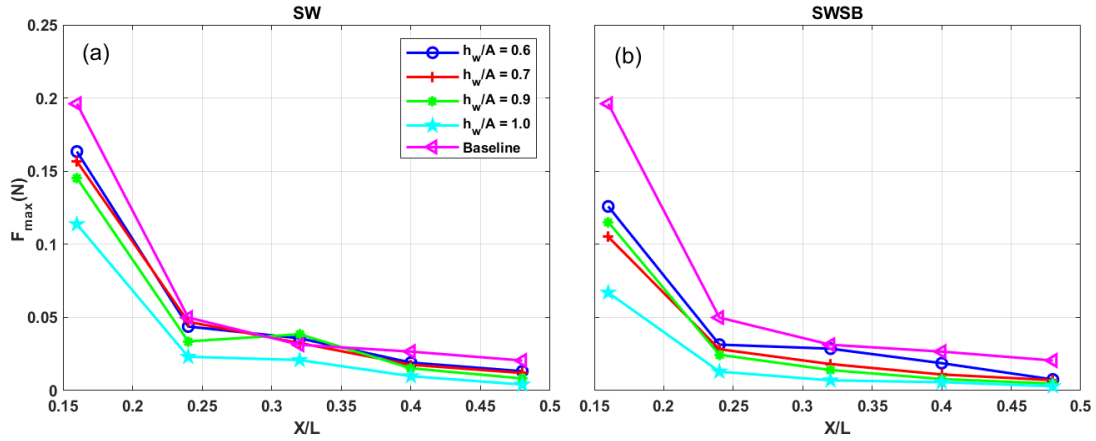


Fig. 10 Maximum forces in five building rows at different seawall heights for SW (a) and SWSB (b) configurations.

Fig. 10, with the same seawall height, the submerged breakwater can reduce the maximum force by over 20% relative to SW-only configurations in the first building row. Generally, increasing seawall height reduced the maximum baseline forces from 15% (for  $h_w/A = 0.6$ ) to 45% (for  $h_w/A = 1.0$ ), while the SWSB configuration resulted in reductions of maximum forces of between 35% and 65%.

Maximum forces monotonically decreased with increasing the relative distance  $X/L$ . From the first to the second row ( $0.16 < X/L < 0.24$ ), maximum forces significantly decreased because the first building row extensively dissipated wave energies of incident overland flows. However, there was a gradual alleviation in maximum forces recorded from the second row to the last row.

4.4 Effects of Seawall Positions

The effects of seawall positions between the shoreline and the first

building row on the performance of structural configurations in reducing hydrodynamics and forces exerted on building elements were numerically investigated by considering four locations of the seawall:  $L_w/L_{sh} = 0, 0.4, 0.5,$  and  $0.6$ .  $L_w$  is the distance from the shoreline to each position of the seawall ( $L_w = 0$  for the seawall located on the shoreline), and  $L_{sh}$  is the distance from the shoreline to the first building row ( $L_{sh} = 1.6$  m). Geometrical dimensions of the seawall and submerged breakwater are similar to those in the experiment.

The left panels of Figs. 11-12 compare the velocity contour at different time instants for the original seawall and closer location to the first building row (right panels of Figs. 11-12) in the SW-only and combined SWSB configurations. As shown in Figs. 11 and 12, there are different wave propagation characteristics in each configuration. For SW configurations with  $L_w/L_{sh} = 0$ , overland flow extensively broke in the flat area, and then the wave energies were significantly

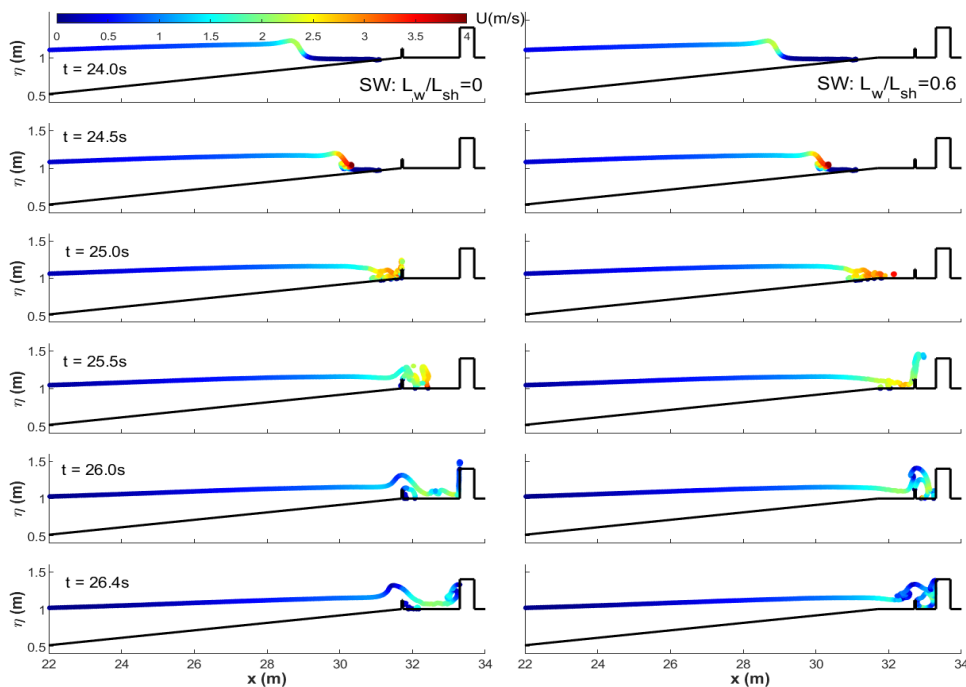


Fig. 11 Velocity contours at different seawall locations at varied time instants in SW configurations:  $L_w/L_{sh} = 0$  (left panels) and  $L_w/L_{sh} = 0.6$  (right panels).

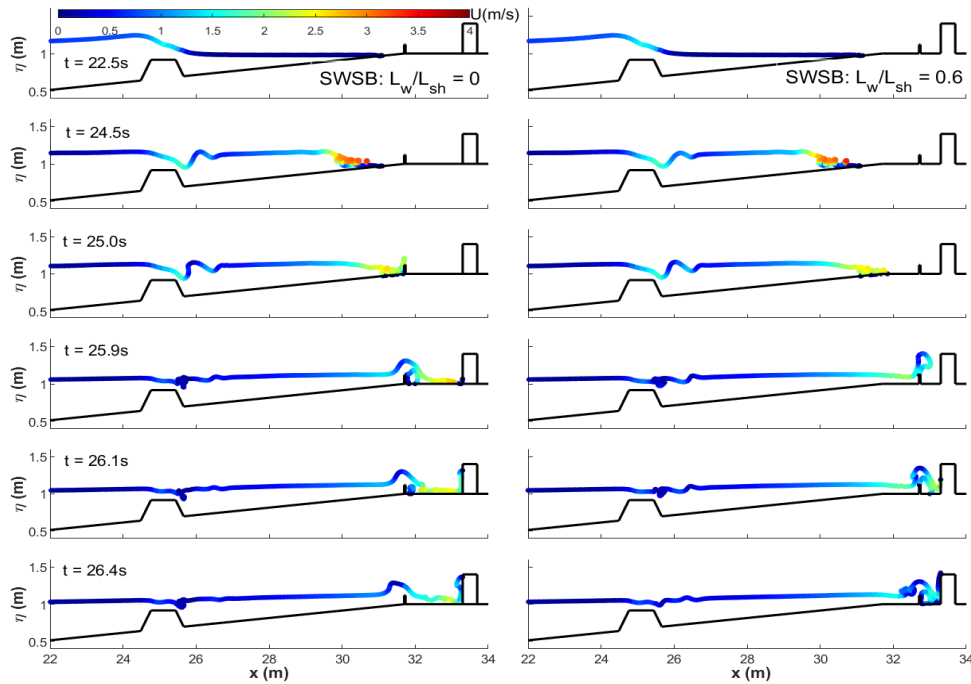


Fig. 12 Velocity contours at different seawall locations at varied time instants in SWSB configurations:  $L_w/L_{sh} = 0$  (left panels) and  $L_w/L_{sh} = 0.6$  (right panels).

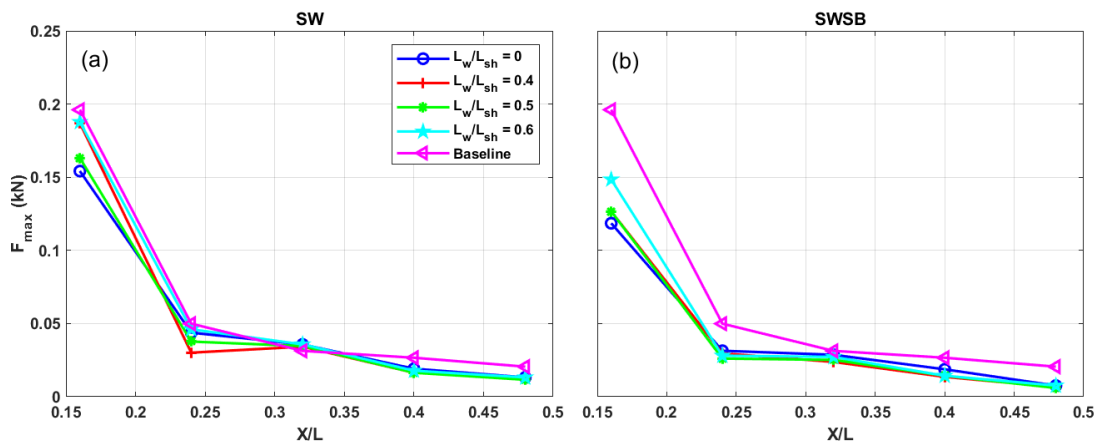


Fig. 13 Maximum forces in five building rows at different seawall locations for SW (a) and SWSB (b) configurations.

dissipated before reaching a building element. However, a closer seawall to the first building row ( $L_w/L_{sh} = 0.6$ ) resulted in larger wave overtopping from the seawall at 25.5 s, which directly impinged on the first building row ( $t = 26$  s) compared to the seawall at the shoreline location ( $L_w/L_{sh} = 0$ ). Therefore, a low-lying seawall located close to the building may induce a higher flow depth and velocity.

Fig. 13 shows the maximum force versus the relative distance  $X/L$  at the four varied seawall positions compared to the baseline condition in both the SW and SWSB configurations. Although the seawall can reduce the maximum baseline forces, installing the seawall near the most seaward building row may amplify maximum horizontal forces compared to the original seawall location on the shoreline. The closer seawall configuration resulted in amplifications of up to 21% and 25% at  $L_w/L_{sh} = 0.6$  for the SW-only and SWSB compared to the configurations with the seawall located at the shoreline. However,

these configurations reduced baseline forces by approximately 5% and 25%, respectively.

#### 4.5 Effects of Submerged Breakwater Freeboards

Four different freeboard ratios of submerged breakwater were selected to examine the effects of submerged breakwaters on reducing maximum forces in a series of building arrays:  $h_f/d = 0.064, 0.044, 0.024,$  and  $0$ . The water level ( $d$ ) was fixed at  $0.98$  m. The freeboard linearly decreased from the original freeboard used in the laboratory ( $h_f/d = 0.064$ ) to the still water level ( $h_f/d = 0$ ). The dimensions of the seawall in the SWSB are similar to the original seawall's ( $h_w = 0.12$  m) in the experiment.

Figs. 14 and 15 show snapshots of velocity contours at the original freeboard ( $h_f/d = 0.064$ ) and lowest freeboard ( $h_f/d = 0$ ) for the SB-only and SWSB configuration at six time instants. As seen in the



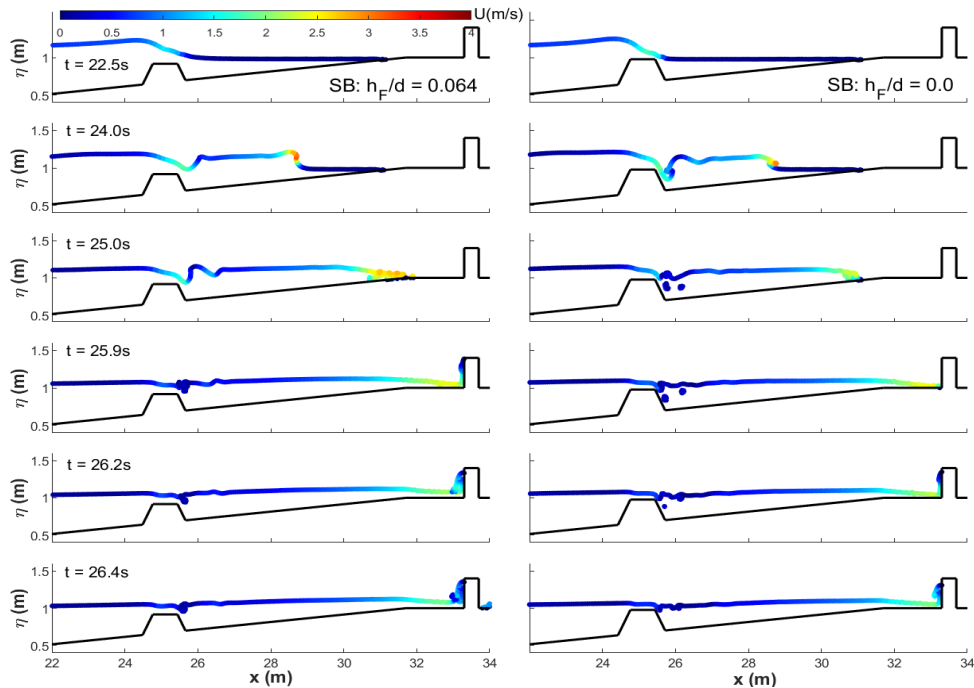


Fig. 14 Velocity contours at different submerged breakwater freeboards at varied time instants in SB:  $h_F/d = 0.064$  (left panels) and  $h_F/d = 0$  (right panels).

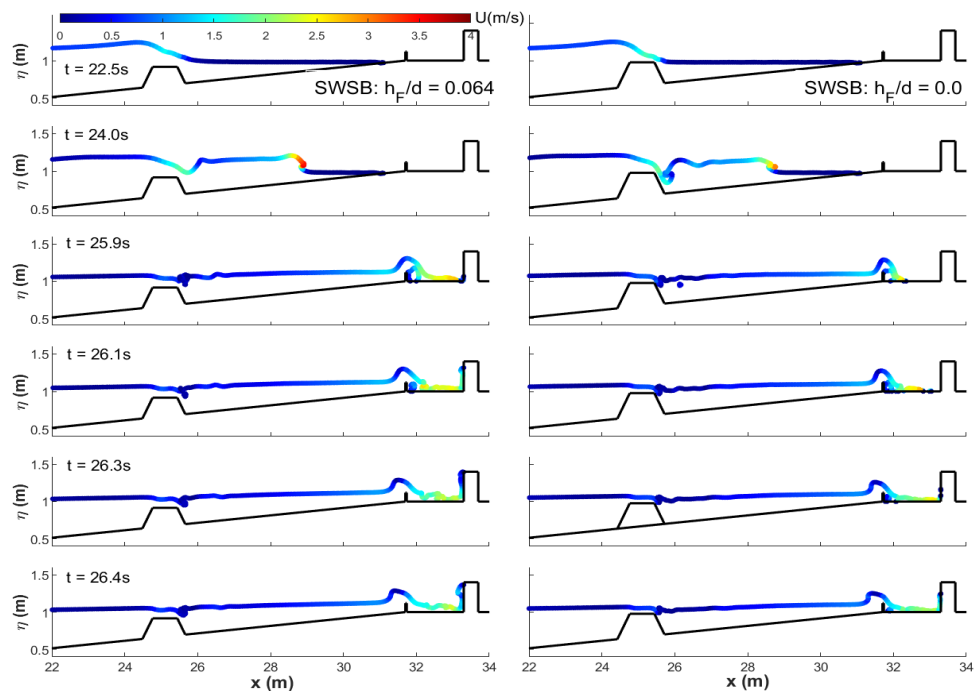
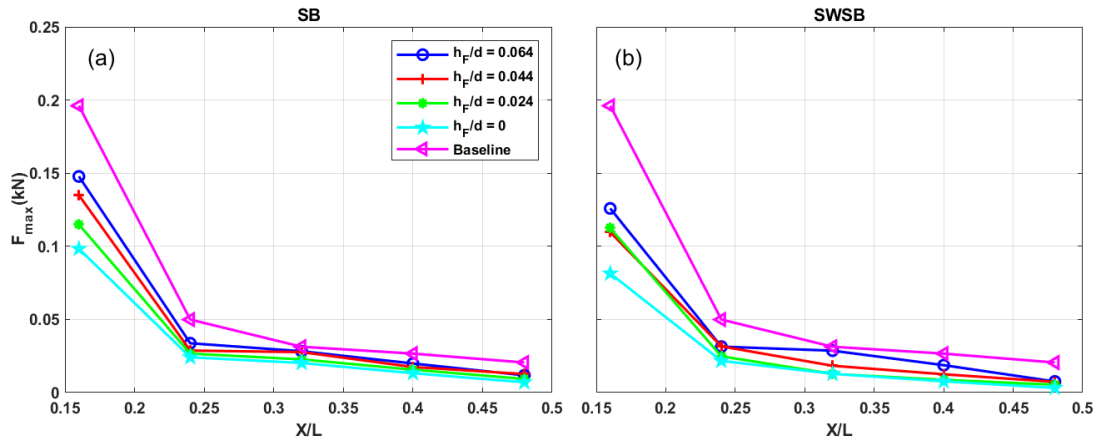


Fig. 15 Velocity contours at submerged breakwater freeboards at varied time instants in SWSB:  $h_F/d = 0.064$  (left panels) and  $h_F/d = 0$  (right panels).

figures, the freeboard significantly influences overland flow hydrodynamics. The lower freeboard condition (higher submerged breakwater) caused tsunami-like waves to travel down deeper on the lee side of the submerged breakwater, inducing turbulent bores with lower surface elevations of 0.17 m (relative to still water level) and velocities of 2.23 m/s, compared to 0.23 m, and 3.25 m/s in the original freeboard condition, respectively, at  $t = 24$  s. In the inland area, the

submerged breakwater with freeboard condition ( $h_F/d = 0$ ) caused a smaller wave runoff climbing up the front face of the first building array. Similarly, the addition of the seawall also diminished the inundation level influencing the vertical building (Fig. 15). Therefore, lowering the freeboard reduced flow depths and velocities in front of building rows.

Fig. 16 compares the maximum forces measured in different



**Fig. 16** Maximum forces in five building rows at different freeboards of the submerged breakwater for SW (a) and SWSB (b) configurations.

freeboard configurations. As discussed, shorter freeboards considerably reduced the onshore inundation depth and velocity, inducing lower maximum forces on a series of vertical building arrays. In the SB-only configuration, submerged breakwater reduced baseline forces by 24%, 28%, 42%, and 50% for the conditions of  $h_f/d = 0.064, 0.044, 0.024,$  and  $0,$  respectively. Moreover, the addition of the seawall can reduce them by approximately 20% more than the corresponding freeboard in the SB configuration. Therefore, the lowest freeboard condition in the SWSB configuration mitigated baseline forces by 70%.

#### 4.6 Effects of Submerged Breakwater Crest Widths

The influences of crest widths ( $W_b$ ) on the performance of submerged breakwater in reducing the overland flow loading on a

series of building arrays were studied. Four crest widths were selected:  $W_b/h_0 = 2.7, 3.0, 3.5,$  and  $4.0.$   $h_0$  is the height from the crest of the submerged breakwater to the middle of the bottom ( $h_0 = 0.25$  m) (Fig. 1). The incident wave height was kept at 0.21 m, the water level is set at 0.98 m, and the dimensions of the seawall remained the same.

As shown in Fig. 17, the influences of crest widths on hydrodynamics in the SB-only configuration at different time instants are very limited. Slight differences in hydrodynamic flow patterns occurred with the seawall as an additional shielding structure (Fig. 18). The overland flow was generated by long-period waves, but all crest widths of the submerged breakwater are significantly shorter compared to the period of flow, inducing a non-significant reduction for each crest width (Fig. 19). The submerged breakwater with different crest widths reduced maximum baseline forces by 25% and

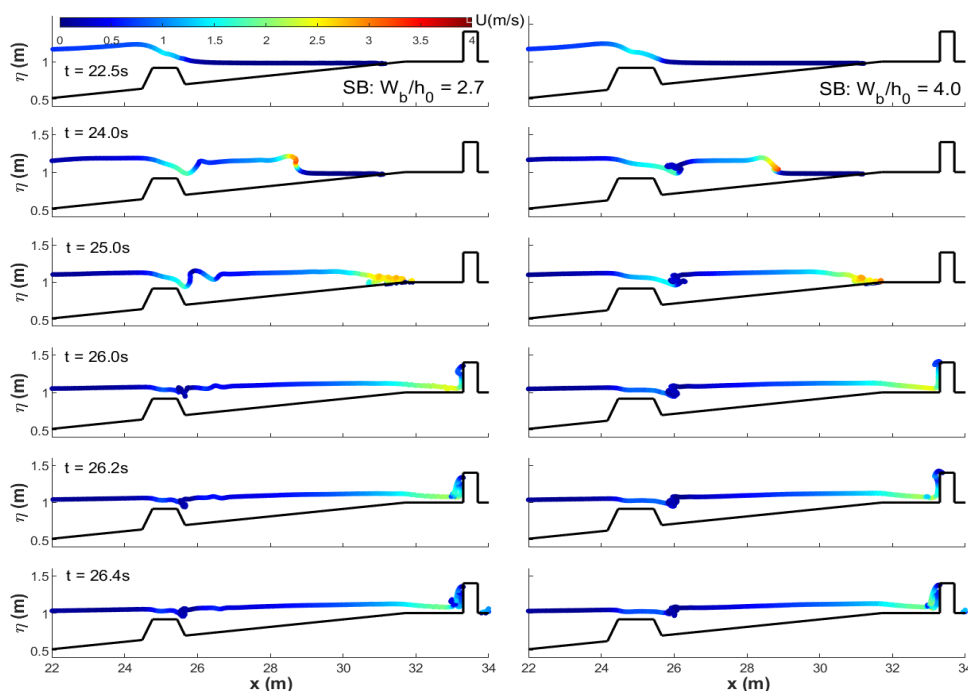


**Fig. 17** Velocity contours at different crest widths of submerged breakwater at time instants in SB:  $W_b/h_0 = 2.7$  (left panels) and  $W_b/h_0 = 4.0$  (right panels).



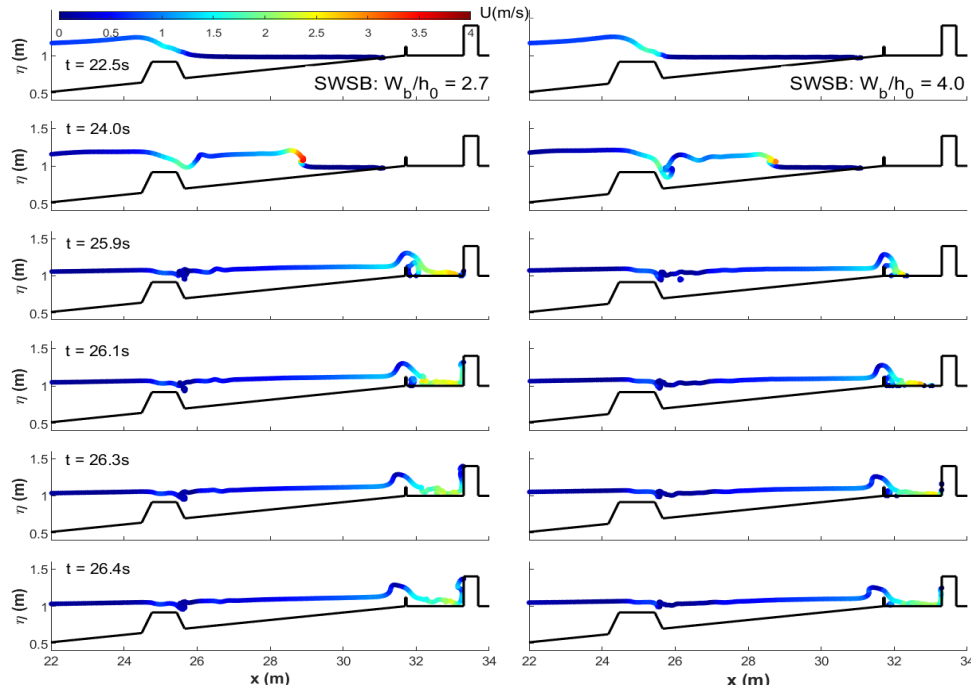


**Fig. 18** Velocity contours at different crest widths of submerged breakwater at time instants in SWSB:  $W_b/h_0 = 2.7$  (left panels) and  $W_b/h_0 = 4.0$  (right panels).

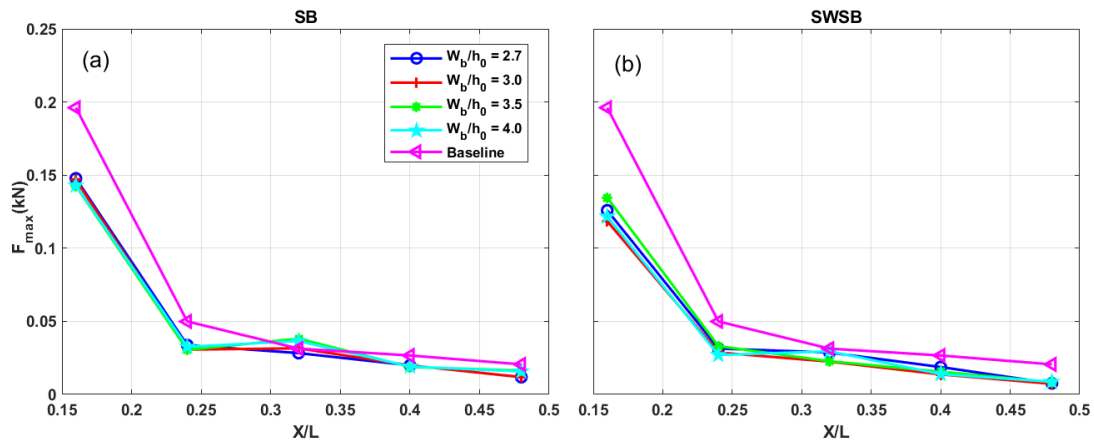


**Fig. 19** Maximum forces in five building rows at different crest widths of the submerged breakwater for SW (a) and SWSB (b) configurations.

38% in the SB-only and SWSB configurations, similar to the original structural conditions ( $W_b/h_0 = 2.7$ ) in the laboratory experiment.

## 5. Conclusions

This study numerically examined the effects of a seawall and submerged breakwater on flow depths, velocities, and forces on a series of building rows in the constructed environment respecting varied heights and positions of the seawall, elevations of freeboards, and crest widths of the submerged breakwater. The primary findings of this paper are summarized as follows:

(1) In general, installing a submerged breakwater and seawall can greatly reduce the intensity of tsunami-like wave-induced overland flow impacts on coastal communities. While the baseline and SB

configurations generated relatively symmetric flow propagating in the constructed environment, SW induced a large turbulent wave splash with high velocities in the built environment. Combined structural configurations significantly reduced cross-shore velocities, inundation depths, and maximum horizontal forces on the inland buildings.

(2) The maximum flow depth and horizontal force linearly increased with the amplitude of incident waves. The presence of both a seawall and submerged breakwater significantly reduced flow depths and forces by a maximum of 64% and 84% relative to the baseline in the four wave conditions, respectively.

(3) The maximum force dramatically decreased with increasing seawall height. The maximum force reductions ranged from 15% to 45% for the SW configuration at different heights in the first building row, but with the additional of a submerged breakwater (SWSB), the

rate of maximum force reduction only increased by 20% compared to the SW configuration.

(4) A low-lying seawall located closer to the first building row induced larger wave overtopping that directly impacted the front face of the first building rows, amplifying the maximum force by up to 25% for the seawall position of  $L_w/L_{sh} = 0.6$  compared to the seawall at the shoreline at  $L_w/L_{sh} = 0$ .

(5) Effects of crest widths of submerged breakwaters on reducing maximum forces were very limited. The SB-only and SWSB configurations resulted in reductions of 25% and 38% of maximum baseline forces in the first building array, respectively.

(6) The freeboard of submerged breakwaters greatly influenced hydrodynamics and maximum forces in the constructed environment. Lower freeboard significantly dissipated tsunami-like wave energies, generating lower turbulent bore impacts on vertical buildings. A submerged breakwater with its crest at the still water level can reduce baseline forces by 50% and 70% for the SB-only and SWSB configurations.

This study comprehensively analyzed the hydrodynamic and force mitigation in an idealized constructed community, which was protected by seawalls and submerged breakwaters with varied dimensions and locations, but there is room for improvement. For example, this study only investigated single tsunami-like wave conditions. However, further investigation is required to consider various wave conditions in random and regular wave conditions with and without currents.

### Conflict of Interest

Sungwon Shin serves as an editor of the Journal of Ocean Engineering and Technology but does not decide about the publication of this article. No potential conflicts of interest relevant to this study are reported.

### Funding

This study was supported by the National Research Foundation of Korea (grant number: 2022R1F1A1071641) and the Korea Evaluation Institute of Industrial Technology (KEIT) grant, which is funded by the Korean government (KCG, MOIS, NFA) [RS-2022-001549812, Development of technology to respond to marine fires and chemical accidents using wearable devices].

### References

- Aarup, T., Aliaga, B., Elliot, T., Kodijat, A., & Yamamoto, M. (2012). *Summary Statement from the Japan – UNESCO – UNU Symposium on The Great East Japan Tsunami on 11 March 2011 and Tsunami Warning Systems: Policy perspectives 16 – 17 February 2012*. UNESCO/IOC: Paris. <https://www.vliz.be/en/imis?refid216585>
- Aghababaei, M., Koliou, M., & Paal, S. G. (2018). Performance assessment of building infrastructure impacted by the 2017 Hurricane Harvey in the Port Aransas region. *Journal of Performance of Constructed Facilities*, 32(5), 4018069. [https://doi.org/10.1061/\(ASCE\)CF.1943-5509.0001215](https://doi.org/10.1061/(ASCE)CF.1943-5509.0001215)
- Dang, H.V., Park, J.-N., Ha, T., Park, H., Shin, S., & Cox, D. (2022). Numerical investigation of countermeasure effects on tsunami inundation hydrodynamic and force mitigation in the coastal communities. *Proceedings of 2022 spring symposium of the Korea Association of Ocean Science and Technology Societies*.
- Dang, V. H., Park, H., Lee, D., Shin, S., Lee, E., Cox, D., & Lomonaco, P. (2022). Physical modeling of hard structure effects on tsunami force reduction in urban coastal environment. In *Ports 2022* (pp. 417–427). <https://doi.org/10.1061/9780784484395.042>
- Eamon, C. D., Fitzpatrick, P., & Truax, D. D. (2007). Observations of structural damage caused by hurricane Katrina on the Mississippi Gulf coast. *Journal of Performance of Constructed Facilities*, 21(2), 117–127. [https://doi.org/10.1061/\(ASCE\)0887-3828\(2007\)21:2\(117\)](https://doi.org/10.1061/(ASCE)0887-3828(2007)21:2(117))
- Higuera, P., Losada, I., & Lara, J.L. (2015). Three-dimensional numerical wave generation with moving boundaries. *Coastal Engineering*, 101, 35–47. <https://doi.org/10.1016/j.coastaleng.2015.04.003>
- Ishii, H., Takabatake, T., Esteban, M., Stolle, J., & Shibayama, T. (2021). Experimental and numerical investigation on tsunami run-up flow around coastal buildings. *Coastal Engineering Journal*, 63(4), 485–503. <https://doi.org/10.1080/21664250.2021.1949920>
- Kihara, N., Arikawa, T., Asai, T., Hasebe, M., Ikeya, T., Inoue, S., Kaida, H., ··· Watanabe, M. (2021). A physical model of tsunami inundation and wave pressures for an idealized coastal industrial site. *Coastal Engineering*, 169, 103970. <https://doi.org/10.1016/j.coastaleng.2021.103970>
- Lee, H- J., & Shin, M- S. (2011). Study of wave absorbing effect of submerged breakwater. *Journal of Ocean Engineering and Technology*, 25(6), 29–34. <https://doi.org/10.5574/KSOE.2011.25.6.029>
- Li, X., & Zhang, W. (2019). 3D numerical simulation of wave transmission for low-crested and submerged breakwaters. *Coastal Engineering*, 152, 103517. <https://doi.org/10.1016/j.coastaleng.2019.103517>
- Lukkunaprasit, P., & Ruangrassamee, A. (2008). Building damage in Thailand in the 2004 Indian Ocean tsunami and clues for tsunami-resistant design. *The IES Journal Part A: Civil & Structural Engineering*, 1(1), 17–30. <https://doi.org/10.1080/19373260701620162>
- Moris, J. P., Kennedy, A. B., & Westerink, J. J. (2021). Tsunami wave run-up load reduction inside a building array. *Coastal Engineering*, 169, 103910. <https://doi.org/10.1016/j.coastaleng.2021.103910>
- Oshnack, M. E., Aguiñiga, F., Cox, D., Gupta, R., & Van de Lindt, J. (2009). Effectiveness of small onshore seawall in reducing forces

- induced by Tsunami bore: large scale experimental study. *Journal of Disaster Research*, 4(6), 382–390. <https://doi.org/10.20965/jdr.2009.p0382>
- Park, H., Cox, D. T., Lynett, P. J., Wiebe, D. M., & Shin, S. (2013). Tsunami inundation modeling in constructed environments: A physical and numerical comparison of free-surface elevation, velocity, and momentum flux. *Coastal Engineering*, 79, 9–21. <https://doi.org/10.1016/j.coastaleng.2013.04.002>
- Park, S., Song, S., Wang, H., Joung, T., & Shin, Y. (2017). Parametric study on scouring around suction bucket foundation. *Journal of Ocean Engineering and Technology*, 31(4), 281–287. <https://doi.org/10.26748/KSOE.2017.08.31.4.281>
- Qin, X., Motley, M. R., & Marafi, N. A. (2018). Three-dimensional modeling of tsunami forces on coastal communities. *Coastal Engineering*, 140, 43–59. <https://doi.org/10.1016/j.coastaleng.2018.06.008>
- Raby, A., Macabuag, J., Pomonis, A., Wilkinson, S., & Rossetto, T. (2015). Implications of the 2011 Great East Japan Tsunami on sea defence design. *International Journal of Disaster Risk Reduction*, 14, 332–346. <https://doi.org/10.1016/j.ijdr.2015.08.009>
- Rahman, S., Akib, S., Khan, M., & Shirazi, S. (2014). Experimental study on tsunami risk reduction on coastal building fronted by sea wall. *The Scientific World Journal*, 2014, 729357. <https://doi.org/10.1155/2014/729357>
- Sogut, D. V., Sogut, E., & Farhadzadeh, A. (2021). Interaction of a solitary wave with an array of macro-roughness elements in the presence of steady currents. *Coastal Engineering*, 164, 103829. <https://doi.org/10.1016/j.coastaleng.2020.103829>
- Sogut, E., Sogut, D. V., & Farhadzadeh, A. (2019). Effects of building arrangement on flow and pressure fields generated by a solitary wave interacting with developed coasts. *Advances in Water Resources*, 134, 103450. <https://doi.org/10.1016/j.advwatres.2019.103450>
- Sun, W., Qu, K., Kraatz, S., Deng, B., & Jiang, C. (2020). Numerical investigation on performance of submerged porous breakwater to mitigate hydrodynamic loads of coastal bridge deck under solitary wave. *Ocean Engineering*, 213, 107660. <https://doi.org/10.1016/j.oceaneng.2020.107660>
- Sweet, W. V., Kopp, R. E., Weaver, C. P., Obeysekera, J., Horton, R. M., Theiler, E. R., & Zervas, C. (2017). *Global and Regional Sea Level Rise Scenarios for the United States* (NOAA Technical Report NOS CO-OPS 083). National Oceanic and Atmospheric Administration / National Ocean Service. <https://pubs.giss.nasa.gov/abs/sw01000b.html>
- Thomas, S., & Cox, D. (2012). Influence of finite-length seawalls for tsunami loading on coastal structures. *Journal of Waterway, Port, Coastal, and Ocean Engineering*, 138(3), 203–214. [https://doi.org/10.1061/\(ASCE\)WW.1943-5460.0000125](https://doi.org/10.1061/(ASCE)WW.1943-5460.0000125)

### Author ORCIDs

Author name	ORCID
Dang, Hai Van	0000-0002-5922-6624
Shin, Sungwon	0000-0002-4564-2627
Lee, Eunju	0000-0001-8939-1391
Park, Hyoungsu	0000-0002-4412-4406
Park, Jun-nyeong	0000-0003-0080-0414

# An Analysis of the Impact of Building Wind by Field Observation in Haeundae LCT Area, South Korea: Typhoon Omais in 2021

Byeonggug Kang<sup>1</sup>, Jongyeong Kim<sup>2</sup>, Yongju Kwon<sup>2</sup>, Joowon Choi<sup>1</sup>, Youngsu Jang<sup>3</sup> and Soonchul Kwon<sup>4</sup>

<sup>1</sup>Master Course Student, Department of Civil & Environmental Engineering, Pusan National University, Busan, Korea

<sup>2</sup>Ph.D Course Student, Department of Civil & Environmental Engineering, Pusan National University, Busan, Korea

<sup>3</sup>Associate Research Engineer, Green Land & Water Management Research Institute, Busan, Korea

<sup>4</sup>Vice professor, Department of Civil & Environmental Engineering, Pusan National University, Busan, Korea

**KEY WORDS:** Building wind, High-rise building, Typhoon, Field observation, Wind ratio, Beaufort wind scale

**ABSTRACT:** In the Haeundae area of Busan, South Korea, damage has continued to occur recently from building wind from caused by dense skyscrapers. Five wind observation stations were installed near LCT residential towers in Haeundae to analyze the effect of building winds during typhoon Omais. The impact of building wind was analyzed through relative and absolute evaluations. At an intersection located southeast of LCT (L-2), the strongest wind speed was measured during the monitoring. The maximum average wind speed for one minute was observed to be 38.93 m/s, which is about three times stronger than at an ocean observation buoy (12.7 m/s) at the same time. It is expected that 3 to 4 times stronger wind can be induced under certain conditions compared to the surrounding areas due to the building wind effect. In a Beaufort wind scale analysis, the wind speed at an ocean observatory was mostly distributed at Beaufort number 4, and the maximum was 8. At L-2, more than 50% of the wind speed exceeded Beaufort number 4, and numbers up to 12 were observed. However, since actual measurement has a limitation in analyzing the entire range, cross-validation with computational fluid dynamics simulation data is required to understand the characteristics of building winds.

## 1. Introduction

As higher concentrations of high-rise buildings in urban areas cause changes in the air flow patterns of the surrounding areas, wind gusts moving over the walls of tall buildings occur and have a negative impact on the wind environment for pedestrians. Building wind refers to the phenomenon in which wind blows against tall buildings in urban areas and generates strong gusts. In the Haeundae area of Busan, which has the highest density of high-rise buildings in South Korea, various damages caused by building winds have continuously occurred in recent years, such as falling building attachments, the spread of wind-born debris, and noise generated by wind. Building wind is caused by an increase in wind speed and wind pressure among buildings. As damages caused by building wind have become a social issue, this phenomenon has gathered increasing attention as a new type of urban disaster.

Building wind also has a positive aspect of decreasing the urban heat-island effect through winds that facilitate the circulation of heat

trapped in urban areas, but its negative impacts emerged as a serious concern when powerful typhoons recently hit South Korea. When Typhoon Maysak and Typhoon Haishen occurred in South Korea in 2020, they caused dangerous situations, including damage to the exterior wall tiles of buildings and glass windows of high-rise buildings in Haeundae.

In countries such as the U.K., Canada, the Netherlands, and Japan, when a high-rise building is constructed, it is mandatory to conduct an assessment of building wind around the construction site in the design or planning stage of a building construction project. In recent years, building wind has been recognized as a social problem in South Korea and other countries, so the central and local governments of South Korea have been trying to establish measures to prevent or mitigate the impact of building wind. However, there is a lack of basic research data for the development of measures suitable for South Korean situations.

In previous studies in South Korea, Roh (2008) carried out a computational fluid dynamics (CFD) analysis for two apartment

Received 10 August 2022, revised 14 September 2022, accepted 26 September 2022

Corresponding author Soonchul Kwon: +82-51-510-7640, [sckwon@pusan.ac.kr](mailto:sckwon@pusan.ac.kr)

© 2022, The Korean Society of Ocean Engineers

This is an open access article distributed under the terms of the creative commons attribution non-commercial license (<http://creativecommons.org/licenses/by-nc/4.0>) which permits unrestricted non-commercial use, distribution, and reproduction in any medium, provided the original work is properly cited.



complexes in Cheonan-si to derive alternative construction techniques and present design standards. Shin et al. (2005) investigated the wind environment and methods for reducing wind disasters by performing field observation and CFD analysis. Choi and Cho (2012) conducted an analysis of the wind corridor of apartment buildings by using CFD analysis.

A number of numerical studies on the impact of building wind have been done. Cho et al. (2012) pointed out that research on the reliability of numerical analysis should be conducted prior to a study of the applicability of numerical methods and stated that there is a need to conduct research on measured data as a criterion for evaluation of the reliability of numerical analysis.

Against this background, we conducted a quantitative analysis of changes in the wind environment caused by the impact of building wind. We performed field monitoring of building wind near the ground surface in areas around high-rise buildings in Haeundae, Busan, when the area was directly affected by Typhoon Omais in 2021.

## 2. Field Monitoring

### 2.1 Research Site

The area selected as a research site in this study was around an apartment complex named LCT in Haeundae in Busan, which is South Korea's largest port city (Fig. 1). When field observations of building

wind are conducted, it is necessary to measure winds that are influenced by buildings, so monitoring points are generally in areas greatly influenced by the surrounding environment, such as areas around high-rise buildings or residential areas. LCT consists of three buildings: the landmark tower and towers A and B. Since the surrounding buildings have much lower heights, strong local winds or scattered winds occur in the LCT area. In addition, since it is located in a coastal area that is vulnerable to wind and flood hazards, the area around LCT is frequently affected by building winds.

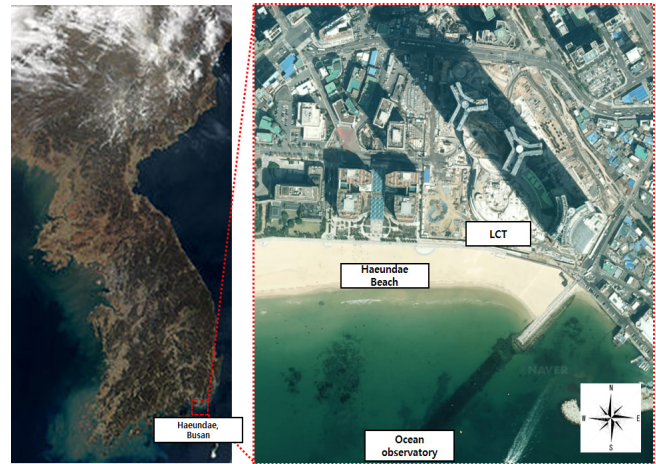


Fig. 1 Location and drone photo of research site

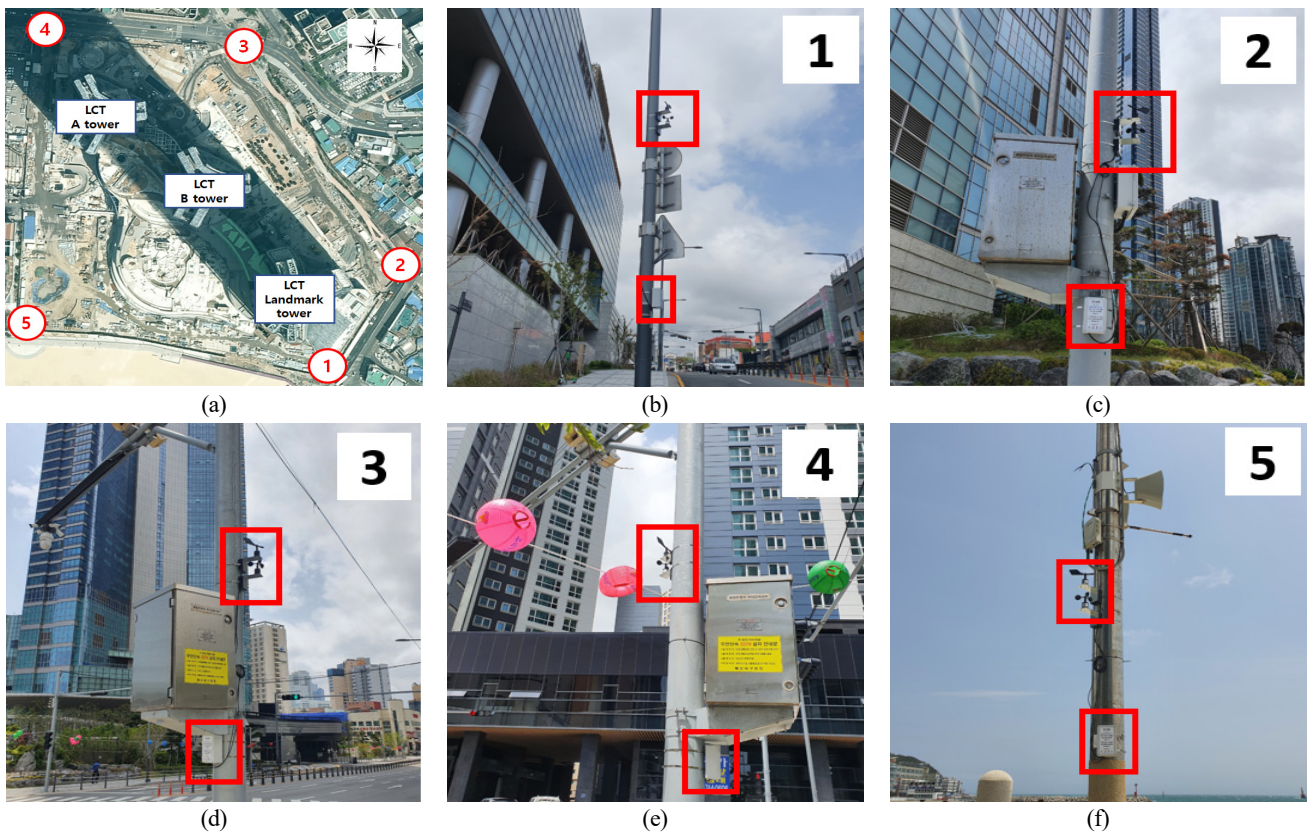


Fig. 2 Installation point of wind speed and wind direction observation equipment: (a) Installation point (L1-5); (b) View of point L-1 (height: 5 m); (c) View of point L-2 (height: 6 m); (d) View of point L-3 (height: 4 m); (e) View of point L-4 (height: 4.6 m); (f) View of point L-5 (height: 4 m)

The landmark tower of LCT is the second tallest building in South Korea with a maximum height of 411.6 m. To observe building wind in the areas around high-rise buildings, five fixed anemometers were installed at scattered points in the research site. More specifically, the monitoring points included locations where strong winds are expected to blow from the open sea (L-1, 5), where strong winds were observed during a preliminary field investigation (L-1, 2, 3), and intersections (L-2, 3, 4). The observation equipment was installed at a height of 4.0 to 8.0 m in consideration of field situations. The locations of monitoring points are shown in Fig. 2 (●).

2.2 Observation Equipment

The monitoring equipment used to observe the impact of building wind (Fig. 3) was designed in accordance with the standard specifications for an automatic weather station (AWS) (Korea Meteorological Administration, 2018). The equipment specifications are presented in Table 1. Data were collected at 0.25-second intervals, so 4 data per second (345,600 data/day) were collected according to the standard specifications of an AWS (Korea Meteorological Administration, 2018). The average wind direction and wind speed for 1 minute were obtained by calculating the average values of the past 240 data collected for 1 minute.



Fig. 3 Observation equipment

Table 1 Specifications of observation equipment

Wind speed	Range	0-70 m/s
	Accuracy	± 2 %
	Resolution	0.1 m/s
Wind direction	Range	0-360°
	Accuracy	±1°
	Resolution	1°
Temperature	Range	-40-85 °C
Atmospheric pressure	Range	300-1100 hPa
Humidity	Range	0-100%

2.3 Haeundae Ocean Observatory

The Haeundae ocean observation buoy is located at Haeundae Beach about 400 m south of the LCT area and is shown in Fig. 4 (●). The Haeundae ocean observation buoy is the meteorological observatory in the area that is closest to the research site and is located in an area with relatively little interference. For these reasons, it was selected as a reference point for comparative analysis of building wind. The reference data were the one-minute average wind speed and wind direction data from the Haeundae ocean observatory. Since building wind characteristically generates local gusts in a short time, the one-minute average data were set as the reference data based on the shortest time unit of the data provided by the ocean observatory.

2.4 Typhoon Omais

Typhoon Omais was the 12th typhoon in 2021. It was a tropical storm with a central pressure of 1004 hPa, a maximum wind speed of 18 m/s, and a strong wind radius of 110 km. It occurred at 21:00 on August 23 in 2021 in the sea about 850 km south-southeast of



Fig. 4 Haeundae ocean observatory



Fig. 5 Path of Typhoon Omais



Okinawa, Japan (Fig. 5). Typhoon Omais was the first typhoon that landed on South Korea in 2021 and started to affect it in the afternoon on August 23. The typhoon disappeared at 09:00 on August 24 according to the Japan Meteorological Agency. Therefore, the monitoring period was set as 00:00 on August 23 to 00:00 on August 25, and measured data collected for a total of 48 hours were used for this study.

### 3. Analysis of the Impact of Building Wind

The methods for assessing the impact of building wind include evaluation in terms of the rate of increase in wind speed (relative evaluation method), evaluation in terms of the allowed wind speed (absolute evaluation method), and a probabilistic evaluation method based on wind-occurrence probability (Kim, 2018). In this study, relative and absolute evaluation methods were employed to evaluate building winds. For the relative evaluation method, the wind speed from Haeundae ocean observatory was set as the reference wind speed, and the wind speed ratio of each monitoring point was calculated by Eq. (1) to examine the rate of increase or decrease in wind speed due to the impact of building wind.

$$WindSpeedRatio(R) = \frac{wind\ speed_{L_i} (m/s)}{wind\ speed_{Ocean\ Observatory} (m/s)} \quad (1)$$

In Eq. (1), *WindSpeedRatio* (*R*) denotes the wind speed ratio of at each monitoring point, *wind speed<sub>L<sub>i</sub></sub>* (m/s) is the wind speed of at each monitoring point, and *wind speed<sub>Ocean Observatory</sub>* (m/s) is the wind speed of at the ocean observatory. Although this method is a convenient method that allows objective comparisons, evaluation using the wind speed ratio is not an appropriate method if there is no meteorological station in the vicinity or if the observation location and the surrounding environment have completely different locational

**Table 2** Beaufort wind scale

Beaufort scale number	Wind speed (m/s)	Expression
0	0-0.3	Calm
1	0.4-1.5	Light air
2	1.6-3.3	Light breeze
3	3.4-5.4	Gentle breeze
4	5.5-7.9	Moderate breeze
5	8.0-10.7	Fresh breeze
6	10.8-13.8	Strong breeze
7	13.9-17.1	Moderate gale
8	17.2-20.7	Gale
9	20.8-24.4	Strong gale
10	24.5-28.4	Storm
11	28.5-32.6	Violent Storm
12	32.7-	Hurricane

characteristics. However, since there is was the an ocean observatory in an area adjacent to the LCT observation points, and it could be used as a comparison group for comparison, and the method was considered as an adequate evaluation method. As Ffor the absolute evaluation method, the Beaufort wind scale presented by Penwarden was used. Table 2 shows the wind speed classified from as 0 to 12 on the Beaufort wind scale and the impact on the human body for each Beaufort number (National Wweather Sservice, 2016).

#### 3.1 Ocean Observatory

Fig. 6 shows the one-minute average wind speed data (●) at the ocean observatory during the study period. At the observatory, a maximum average wind speed of 18.5 m/s was recorded at 01:07 on August 24. After that, the wind speed decreased, but it started to increase again at 12:00 on August 24. Then, a maximum average wind speed of 15.5 m/s (west-southwest) was observed at 12:26 on August 24, and high wind speed was maintained until 16:00. The prevailing wind directions at the ocean observatory during the monitoring period were west-southwest(24.77%) and southwest (18.64%).

#### 3.2 The Wind Speed and Wind SpeedRatio of the LCT Area (Relative Evaluation Method)

Fig. 6 shows the one-minute average wind speed (■) measured at 5 monitoring points (L-1-L-5) in the LCT area. In addition, the wind speed ratio (▲) of each monitoring point is shown in Fig. 7. The speed ratio is the ratio of the wind speed at each monitoring point to the wind speed at the ocean observatory.

A large amount of wind speed data was missing at points L-1 and L-2 due to mechanical defects, and the missing rate is shown in Table 3. In the calculation of the wind speed ratio, missing wind speed data were excluded. Some wind speed ratios obtained were excessively high values of 5-25, which may be attributed to the fact that wind speed measured at the ocean observatory were much lower, even though the wind speeds at each monitoring point were low. Therefore, in this study, the wind speed ratio was calculated only for cases where the wind speed at the ocean observatory was 2 m/s or more to derive wind speed ratios for only cases where significant wind speed values were observed.

The one-minute average wind speeds at L-1 are shown in Fig. 6(a). The maximum average wind speed recorded at L-1 during the monitoring period was 35.23 m/s at 01:35 on August 24. At this time, the wind speed at the ocean observatory was 15.5 m/s (west-southwest). The maximum wind speed at L-1 was 2.27 times stronger than the wind speed measured at the ocean observatory during the

**Table 3** Missing rate at each point (L1-5)

Point	L-1	L-2	L-3	L-4	L-5	Ocean observatory
Missing rate (%)	52.05	27.60	0.63	0.38	4.03	0.35

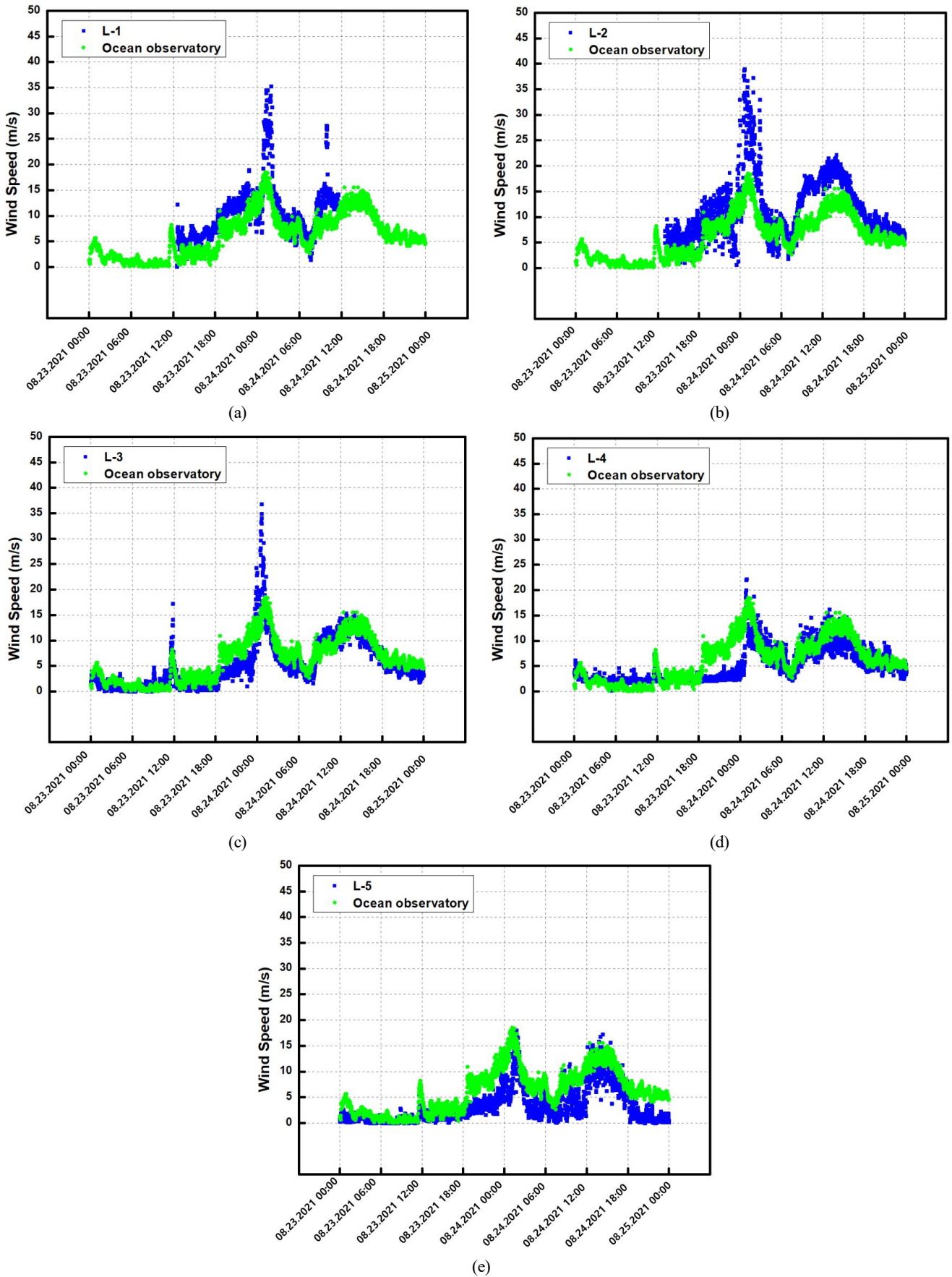


**Fig. 6** Wind speed comparison (LCT ■ vs. Ocean observatory ●). (a) L-1 vs. Ocean observatory; (b) L-2 vs. Ocean observatory; (c) L-3 vs. Ocean observatory; (d) L-4 vs. Ocean observatory; (e) L-5 vs. Ocean observatory



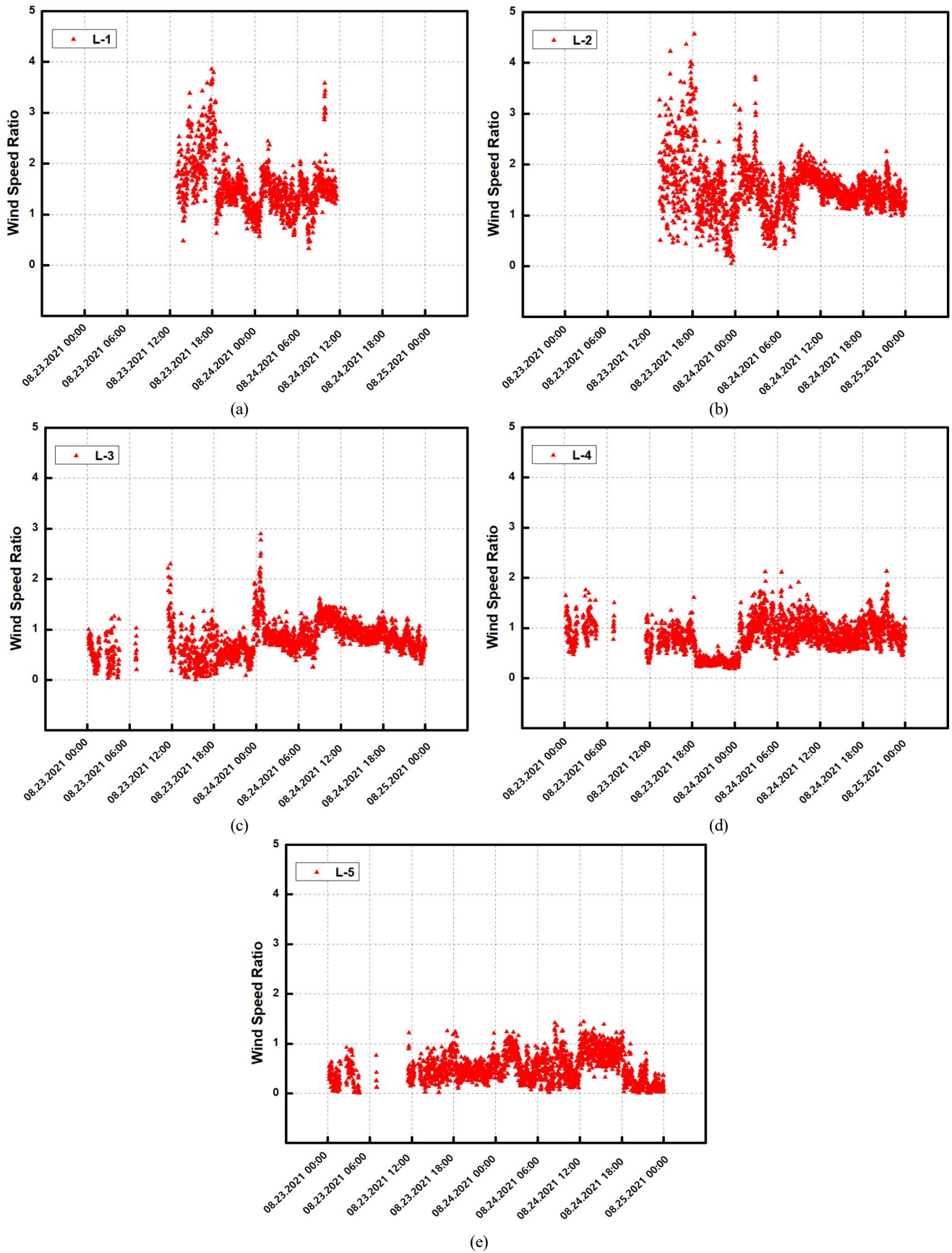


**Fig. 7** Frequency distribution of wind speed ratio (LCT vs. Ocean observatory); ( $\text{Windspeed}_{\text{LCT}}/\text{Windspeed}_{\text{Oceanobservatory}}$  ▲). (a) L-1 vs. Ocean observatory; (b) L-2 vs. Ocean observatory; (c) L-3 vs. Ocean observatory; (d) L-4 vs. Ocean observatory; (e) L-5 vs. Ocean observatory

same period of time. The wind speed ratio of L-1 is shown in Fig. 7(a) and ranges from 0 to 3.86. The maximum wind speed ratio of 3.86 was observed at 17:56 on August 23. At this time, the wind speed at L-1 was 7.71 m/s, and the wind speed at the ocean observatory was 2 m/s (north).

The one-minute average wind speed at L-2 is shown in Fig. 6(b). The maximum average wind speed measured at L-2 was 38.93 m/s (south), and it was observed at 00:37 on August 24. At the time, the wind speed at the ocean observatory was 12.7 m/s (south-southwest). The maximum wind speed at L-2 was 3.07 times stronger than the wind speed measured at the ocean observatory at the same time point.

The wind speed ratio of L-2 is shown in Fig. 7(b) and it ranges from 0 to 4.57. The maximum wind speed ratio of 4.47 was observed at 18:13 on August 23. At this time, the wind speed at L-2 was 9.59 m/s, and the wind speed at the ocean observatory was 2.1 m/s (northeast).

The one-minute average wind speed of L-3 are shown in Fig. 6(c). The maximum average wind speed measured at L-3 was 36.77 m/s (south), and it was observed at 00:37 on August 24. At this time, the wind speed at the ocean observatory was 12.7 m/s (south-southwest). The maximum wind speed at L-3 was 2.89 times stronger than the wind speed measured at the ocean observatory during the same period of time.

The wind speed ratio of L-3 is shown in Fig. 7(c) and it ranges from 0 to 2.89. The maximum wind speed ratio of 2.89 was observed at 00:37 on August 24. At this time, the wind speed at L-3 was 36.77 m/s (south), and the wind speed at the ocean observatory was 12.7 m/s (south-southwest).

The one-minute average wind speed of L-4 are shown in Fig. 6(d). The maximum average wind speed measured at L-4 was 22.21 m/s (southwest), and it was observed at 00:52 on August 24. At this time, the wind speed at the ocean observatory was 17.9 m/s (south-southwest). The maximum wind speed at L-4 was 1.24 times stronger than the wind speed measured at the ocean observatory during the same period of time.

The wind speed ratio is shown in Fig. 7(d). It ranges from 0 to 2.13, and the maximum wind speed ratio of 2.13 was observed at 21:23 on August 24. At this time, the wind speed at L-4 was 8.73 m/s (south-southwest), and the wind speed at the ocean observatory was 4.1 m/s (west).

The one-minute average wind speed of L-5 are shown in Fig. 6(e). The maximum average wind speed measured at L-5 was 18.0 m/s (southwest), and it was observed at 01:44 on August 24. At this time, the wind speed at the ocean observatory was 16.3 m/s (southwest). The maximum wind speed at L-5 was 1.10 times stronger than the wind speed measured at the ocean observatory during the same period of time.

The wind speed ratio of L-5 is shown in Fig. 7(e). It ranges from 0 to 1.44, and the maximum wind speed ratio of 1.44 was observed at 12:34 on August 24. At this time, the wind speed at L-5 was 14.27 m/s (west-southwest), and the wind speed at the ocean observatory was 9.9 m/s (west).

### 3.3 Beaufort Wind Scale (Absolute Evaluation Method)

Since wind damage generally occurs due to strong wind speed, it is necessary to assess the absolute value of the increase in wind speed due to the impact of building wind. Thus, wind speed was measured at the five monitoring points of the LCT area (■) and at the Haeundae ocean observatory (■) and are presented in a graph to show the frequencies of the wind speed by applying the Beaufort wind scale (Table 2), as shown in Fig. 8. A comparative analysis was performed by excluding missing data and Beaufort numbers of 0 (calm) from the analysis for convenience.

The Beaufort number of wind speed observed at the ocean observatory ranged from 1 to 8, and the frequencies of Beaufort numbers 1 to 8 were 14.44, 15.17, 13.91, 20.95, 17.76, 12.02, 3.82, and 0.60 %, respectively. The mode was 4 (moderate breeze), and the highest Beaufort number was 8 (gale). We performed a comparative analysis between the Beaufort number at the ocean observatory and those at each monitoring point in the LCT area, as shown in Figs. 8(a)–8(e). The Beaufort numbers observed at L-1 are shown in Fig. 8(a). The Beaufort number ranged from 1 to 12, and the frequencies of the Beaufort numbers 1 to 12 were 0.22, 1.59, 11.30, 21.80, 19.55, 30.63, 7.89, 0.72, 1.59, 3.19, 0.94, and 0.51%, respectively. The mode was 6 (strong breeze), and the highest Beaufort number was 12 (hurricane). The Beaufort numbers observed at L-2 are shown in Fig. 8(b). The Beaufort numbers ranged from 1 to 12, and their frequencies of the were 0.34, 2.97, 8.78, 21.29, 20.48, 13.76, 13.76, 12.47, 2.06, 1.29, 1.73, and 1.06%, respectively. The mode was 4 (moderate breeze), and the highest Beaufort number was 12 (hurricane).

The Beaufort numbers observed at L-3 are shown in Fig. 8(c). The Beaufort numbers ranged from 1 to 12, and their frequencies were 18.94, 16.98, 23.06, 11.39, 9.96, 11.18, 2.55, 0.73, 0.38, 0.38, 0.21, and 0.17%, respectively. The mode was 3 (gentle breeze), and the highest Beaufort number was 12 (hurricane). The Beaufort numbers observed at L-4 are shown in Fig. 8(d). The Beaufort numbers ranged from 1 to 9, and their frequencies were 0.56, 45.59, 13.84, 17.01, 16.35, 5.44, 0.77, 0.24, and 0.07%, respectively. The mode was 2 (light breeze), and the highest Beaufort number was 9 (severe gale). The Beaufort numbers observed at L-5 are shown in Fig. 8(e). The Beaufort numbers ranged from 1 to 8, and their frequencies were 29.41, 24.46, 13.06, 8.39, 8.86, 5.07, 1.37, and 0.07%, respectively. The mode was 1 (light air), and the highest Beaufort number was 8 (gale).

## 4. Discussion

In this study, we conducted field monitoring of Typhoon Omais by installing 5 anemometers to examine the impact of building wind in the area around LCT, an area with a high density of high-rise buildings. The analysis of the measured data was conducted by both the relative evaluation method by the estimation of wind speed ratios (the rates of increase in wind speed) and the absolute evaluation method using the Beaufort wind scale, and the following conclusions were drawn based on the analysis results. The comparative analysis

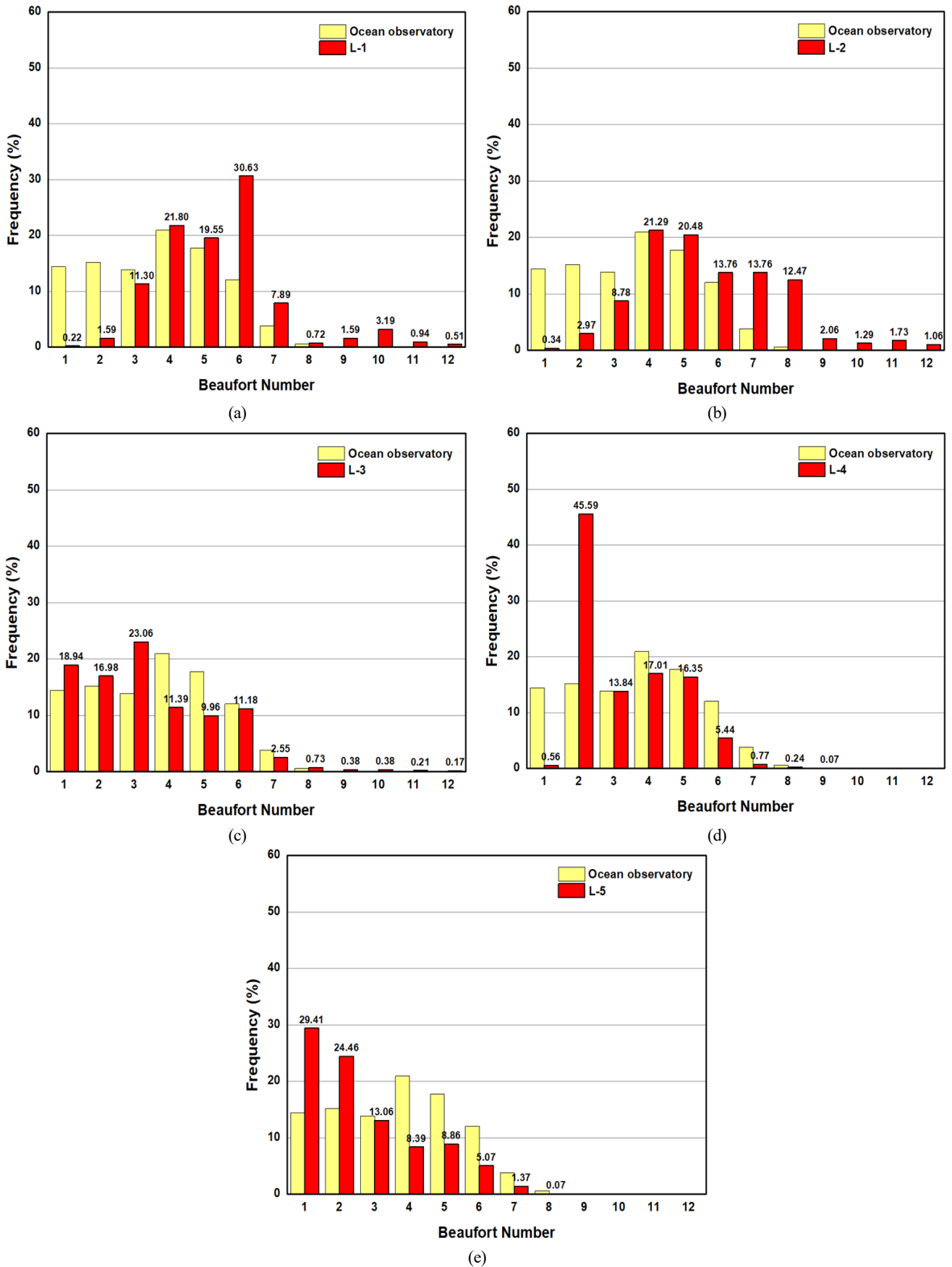


Fig. 8 Frequency distribution of Beaufort wind scale (LCT ■ vs. Ocean observatory ■ ). (a) L-1 vs. Ocean observatory; (b) L-2 vs. Ocean observatory; (c) L-3 vs. Ocean observatory; (d) L-4 vs. Ocean observatory; (e) L-5 vs. Ocean observatory

between the measured data at each observation point and those at the ocean observatory revealed different building wind patterns depending on the locational characteristics at each observation point. At L-1, a maximum wind speed of 35.25 m/s and a maximum wind speed ratio of 3.86 were measured. L-1 was located near the side of the landmark tower building of LCT and adjacent to the seashore of Haeundae. In view of these characteristics of L-1, high wind speeds observed at L-1 are thought to be due to the fact that sea breeze blowing from the sea towards land flows over the walls of the tall building without any interference, generating separated flow and downslope wind.

At L-2, a maximum wind speed of 38.93 m/s and maximum wind speed ratio of 4.57 were observed. The highest maximum wind speed and wind speed ratio were observed at L-2 among the five monitoring points. It is presumed that since L-2 was located at the corner of an LCT building, the separated flow and downslope wind of the building were combined, so this location showed a significant impact of building wind. At L-3, a maximum wind speed of 36.77 m/s and maximum wind speed ratio of 2.89 were measured. Strong wind speed observed at L-3 are thought to be due to the fact that this monitoring point was located at an intersection surrounded by buildings and on bare ground without obstacles around the monitoring location.

On the other hand, L-4 showed a maximum wind speed of 22.21 m/s and maximum wind speed ratio of 1.24, even though it was situated at an intersection among high-rise buildings like L-3. In other words, L-4 showed less impact of building wind compared to L-1, L-2, and L-3. These results are believed to reflect the impact of trees planted around L-4. In a previous study, Cheong and Ryu (2013) performed CFD analysis to investigate the windbreak effects of trees. The results of their study showed that planted trees decreased the maximum wind speed at the level of pedestrians around buildings from Beaufort force 11 to Beaufort force 9. In addition, Kim et al. (2013) demonstrated the windbreak effects of vegetation through a wind tunnel experiment. In the present study, L-4, which had surrounding areas with planted trees, showed lower maximum wind speed than other monitoring locations. In consideration of the previous studies on the windbreak effects of trees, the lower wind speed of L-4 can be attributed to the impact of trees.

L-5 was located in front of LCT buildings, where there was a small impact of building wind. As a result, L-5 showed the lowest maximum wind speed of 18.00 m/s and the lowest maximum wind speed ratio of 1.10 among the five monitoring points. In addition, there was a low-rise structure with the height of a three-story building between L-5 and LCT buildings. Because this low-rise structure acted as a set-back structure that offset building winds such as downslope wind, the building wind had less impact on L-5. Set-back structures are effective in reducing downslope winds and separated flows (City of Toronto, 2013). In this study, the data of L-5 confirmed this.

At L-1 and L-2, the frequency of Beaufort wind scale 6 or higher was found to be about 50%. In addition, at L-2, where the highest maximum wind speed was observed during the monitoring period, the frequency of Beaufort wind scale 8 or higher was about 20%. At

Beaufort wind scale 6, pedestrians feel uncomfortable when walking outside, and at Beaufort wind scale 8 or higher, pedestrians are likely to fall since they have difficulty in maintaining balance. In other words, the measured data of L-1 and L-2 indicate that the areas near these points have a very poor wind environment for pedestrians.

At L-1, L-2, and L-3, the highest value on the Beaufort wind scale of 12 was observed. Compared to the maximum Beaufort wind scale value of 8 at the Haeundae ocean observatory, these results indicated that there was a large increase in wind speed at L-1, L-2, and L-3. These increases in wind speed are thought to show that wind speeds at these monitoring points were greatly affected by building wind. At L-4 and L-5, which were influenced by trees and a set-back structure, the highest Beaufort numbers observed were 9 and 8, respectively, and they are close to the Beaufort numbers at the Haeundae ocean observatory. This result confirmed again that L-4 and L-5 were less affected by building wind compared to L-1, L-2, and L-3.

Kim et al. (2021) investigated building wind through field monitoring data of the Marine City area of Haeundae during the landfall of Typhoon Omais. A maximum wind speed of 28.99 m/s and maximum wind speed ratio of 2.92 were measured. The highest Beaufort number was 11. In the present study, the location where the strongest building wind was observed was L-2 with a maximum wind speed of 38.93 m/s and maximum wind speed ratio of 3.07. The highest Beaufort number observed in the LCT area was 12, and it was observed at L-1, L-2, and L-3.

The height of the tallest building in the Marine City area is 301 m, which is lower compared to the maximum height of the buildings of LCT. This seems to be the reason why the impact of building wind was smaller in the Marine City area than in the LCT area. As in L-4, where planted trees were found to function as a wind-breaking forest, the two points with planted trees in the Marine City area showed a lower building wind impact. This demonstrates that a wind-breaking forest is effective in reducing the impact of building wind.

This study has some limitations. First, we could not analyze the risk of building wind for a broad range of the research site because there was not a sufficient number of observation points, and measurements of wind speed at different altitudes were not performed. Therefore, a follow-up study should be conducted with CFD simulation for the entire range and cross-validation between measured data and CFD simulation data.

## Conflict of Interest

Soonchul Kwon serves as an editor of the Journal of Ocean Engineering and Technology but had no role in the decision to publish this article. No potential conflict of interest relevant to this article was reported.

## Funding

This research was supported by a grant (20011068) from the

Regional Customized Disaster-Safety R&D Program, which is funded by the Ministry of Interior and Safety (MOIS, Korea).

## References

- Cheong, C. H., Ryu, S. R. (2013). An analysis on the building Wind variation in the Residential Community Pedestrian Area by the Planting Method. *Journal of the Architectural Institute of Korea*, 29(11), 253–262. [https://doi.org/10.5659/JAIK\\_PD.2013.29.11.253](https://doi.org/10.5659/JAIK_PD.2013.29.11.253)
- Cho, J. H., Yim, S. R., Lee, K. S., Han, S. E. (2012). A study on the evaluation of wind environment and analytical Method using CFD analysis. *Journal of the Architectural Institute of Korea Structure & Construction*, 28(7), 99–106. [https://doi.org/10.5659/JAIK\\_SC.2012.28.7.99](https://doi.org/10.5659/JAIK_SC.2012.28.7.99)
- Choi, C. H., Cho, M. K. (2012). A study on apartment ventilation path using the CFD. *Journal of Korean Institute of Architectural Sustainable Environment and Building Systems*, 6(2), 93–98.
- City of Toronto. (2013). *Tall building design guidelines*. City of Toronto.
- Kim, H. J., Kim, H. S., Jung, S. H., Lee, S. H. (2013), Analysis on effects of protection against eind according to tree species and planting methods of the wind break forest based on the wind tunnel experiment. *Proceedings of 2013 Forest Science Joint Conference*, 791–794.
- Kim, H. L. (2018). *Building and wind dynamics*. Ilgwang.
- Korea Meteorological Administration. (2018). *Standard specification for automatic weather observation equipment (2018-3)*. <https://www.law.go.kr/LSW/admRulLsInfoP.do?admRulSeq2100000112610>
- Kim, J., Kang, B., Kwon, Y., Lee, S., and Kwon, S. (2021). A review on the building wind impact through on-site monitoring in Haeundae Marine City: 2021 12<sup>th</sup> typhoon OMAIS case study. *Journal of Ocean Engineering and Technology*, 35(6), 414–425. <https://doi.org/10.26748/KSOE.2021.079>
- National weather service. (2016). *Beaufort wind scale*. <https://www.weather.gov/mfl/beaufort>
- Roh, J. W., (2008). Example study on building wind of apartment complex by computational fluid dynamics. *Journal of the KIEAE*, vol(8), no. 4, 37–42.
- Shin, J. W., Lee, Y. J., Kim, T. Y., Lee, K. H. (2005). A study on the windbreak facilities design for reducing building wind damage to pedestrian area. *Proceeding of conference of Architectural Institute of Korea*, 25(1), 147–150.

## Author ORCIDs

Author name	ORCID
Kang, Byeonggug	0000-0003-4057-4386
Kim, Jongyeong	0000-0001-6642-8622
Kwon, Yongju	0000-0001-7935-8416
Choi, Joowon	0000-0003-1333-6040
Jang, Youngsu	0000-0002-3261-4731
Kwon, Soonchul	0000-0003-3764-331X



# Motion Analysis of A Wind-Wave Energy TLP Platform Considering Second-order Wave Forces

Hongbhin Kim<sup>1</sup>, Eun-hong Min<sup>2,3</sup>, Sanghwan Heo<sup>2,3</sup> and WeonCheol Koo<sup>4</sup>

<sup>1</sup>Graduate student, Department of Naval Architecture and Ocean Engineering, Inha University, Korea

<sup>2</sup>Post doctor, Department of Naval Architecture and Ocean Engineering, Inha University, Korea

<sup>3</sup>Visiting fellow, Department of Ocean Engineering, Texas A&M University, USA

<sup>4</sup>Professor, Department of Naval Architecture and Ocean Engineering, Inha University, Korea

**KEY WORDS:** Floating offshore wind turbine, Wave energy converter, Power take-off, 2nd-order wave load, Motion analysis, Nonlinear Froude-Krylov force

**ABSTRACT:** Offshore wind energy has become a major energy source, and various studies are underway to increase the economic feasibility of floating offshore wind turbines (FOWT). In this study, the characteristics of wave-induced motion of a combined wind-wave energy platform were analyzed to reduce the variability of energy extraction. A user subroutine was developed, and numerical analysis was performed in connection with the ANSYS-AQWA hydrodynamic program in the time domain. A platform combining the TLP-type FOWT and the Wavestar-type wave energy converter (WEC) was proposed. Each motion response of the platform on the second-order wave load, the effect of WEC attachment and Power take-off (PTO) force were analyzed. The mooring line tension according to the installation location was also analyzed. The vertical motion of a single FOWT was increased approximately three times due to the second-order sum-frequency wave load. The PTO force of the WEC played as a vertical motion damper for the combined platform. The tension of the mooring lines in front of the incident wave direction was dominantly affected by the pitch of the platform, and the mooring lines located at the side of the platform were mainly affected by the heave of the platform.

## 1. Introduction

Energy consumption is increasing rapidly with population growth and technological development. In particular, the excessive development and use of fossil energy cause a global pollution problem, and excessive greenhouse gas emissions, including carbon dioxide, leads to global warming and various environmental problems. Therefore, it is essential to develop technologies for renewable energy, which is a sustainable and eco-friendly energy source (Muliawan et al., 2013; Ullah et al., 2020).

Among renewable energy sources, offshore wind energy, wave energy, and current energy, which are representative offshore energy sources, require future-oriented and continuous technology development. In particular, many technologies have been developed for offshore wind energy because it has benefits in terms of wind homogeneity and speed as well as the installation location compared to onshore wind energy (land-based wind energy). Large-scale commercial power generation is also possible because it is free of the

restrictions of many wind turbine installation spaces and noise (Bae and Kim, 2013). As offshore wind turbine technology has grown into a major energy source worldwide, including in Europe, many studies have been conducted to increase the economic feasibility of offshore wind turbine platforms (Global Wind Energy Council Global, 2019).

A combined wind-wave energy platform in which wave energy converters (WECs) are attached to floating wind turbines has been reported as one way to increase the economic feasibility of floating offshore wind turbine (FOWT) in many studies. The combined energy platform is based on the typical characteristics of ocean environments: relatively high waves accompany high wind speeds. Moreover, using two energy sources makes it possible to reduce the energy extraction variability of a single offshore wind turbine and increase the economic effects (Kim et al., 2015). As a combined wind-wave energy platform type, there is a combined platform model that combines the OC4 model (Robertson et al., 2014), a semi-submersible wind turbine structure disclosed by the National Renewable Energy Lab (NREL) in the United States, with Wavestar-type WECs (Hansen et al., 2013). Si et al. (2021)

Received 13 September 2022, revised 27 October 2022, accepted 16 November 2022

Corresponding author WeonCheol Koo: +82-32-860-7348, [wckoo@inha.ac.kr](mailto:wckoo@inha.ac.kr)

© 2022, The Korean Society of Ocean Engineers

This is an open access article distributed under the terms of the creative commons attribution non-commercial license (<http://creativecommons.org/licenses/by-nc/4.0>) which permits unrestricted non-commercial use, distribution, and reproduction in any medium, provided the original work is properly cited.

analyzed the motion performance and power generation efficiency of this platform. A study also proposed a model by combining OC (Jonkman, 2010), a Spar-type wind turbine of NREL, with Wavestar-type WEC and analyzed its motion performance and power generation efficiency (Ghafari et al., 2021). In South Korea, many studies have been conducted, including a study on the conceptual design of a large combined wind-wave energy platform based on a semi-submersible (Kim et al., 2015), a study on the hydrodynamic interaction between a combined energy structure and the attached WECs (Lee et al., 2016), and a study on the design of a motion reduction device for a combined energy platform (Park et al., 2018).

Few studies have examined the performance of combined energy platforms based on a tension-leg platform (TLP), a representative offshore structure with excellent motion performance on waves. TLP is very stable in terms of heave, pitch, and roll compared to a semi-submersible or Spar platform (Oguz et al., 2018), and the platform construction cost is relatively low (Tsouroukdisian et al., 2016). In addition, when a large-scale offshore wind farm is constructed, the installation area of mooring lines is smaller than that of catenary mooring lines because they are installed vertically downward, causing less interference with nearby structures or maritime fishing activities. Therefore, various studies have been conducted worldwide on TLP-type offshore wind turbine platforms (Adam et al., 2014; Kim et al., 2016; Chung et al., 2021; Ren et al., 2022). A previous study reported that the TLP platforms are economical because their life-cycle cost (LCC) is relatively lower than that of Spar platforms (Pantusa et al., 2020). For TLP platform, however, the natural frequency of the platform motion is high because of the high stiffness of mooring lines. A relatively large motion response occurs under high-frequency wave loads, such as 2<sup>nd</sup>-order sum-frequency wave loads. This leads to an increase in the fatigue of mooring lines (Kim, 1991). Therefore, it is necessary to identify the motion response characteristics of a combined wind-wave energy platform precisely based on the TLP platform. In particular, understanding the motion characteristics of TLP platform under 2<sup>nd</sup>-order wave loads provides the basic knowledge required for designing combined energy platforms in the future; it makes it possible to secure the diversity of platforms to be designed.

Therefore, this study analyzed the motion characteristics under 2<sup>nd</sup>-order wave loads to identify the precise motion response of a combined wind-wave energy platform based on the TLP structure. A platform that combined MIT-NREL TLP (Matha et al., 2010), a TLP-type offshore wind turbine model disclosed by NREL, with Wavestar-type WECs was set as a numerical model. As mentioned above, this is to present a new type of combined wind-wave energy platform to which a movable body-type WEC is attached while utilizing the excellent motion response performance of TLP on waves and the advantages of installing multiple WECs. In particular, the wind load acting on the wind turbine was excluded, and focus was given to the analysis of the motion by the wave load to identify the motion response characteristics of the structure that combined TLP with

hemispherical WECs under 2<sup>nd</sup>-order wave loads. The motion characteristics of the combined platform were compared according to the application of the 2<sup>nd</sup>-order sum-frequency wave load and the attachment of WECs. The power take-off (PTO) model was applied to WECs.

In this study, ANSYS AQWA (AQWA-NAUT module), a hydrodynamic program, was used to calculate the motion performance of the combined energy platform. In order to apply the 2<sup>nd</sup>-order wave loads and the nonlinear Froude-Krylov force that changes every time step due to body motion to the platform and apply the PTO damping force to the WECs, a user-subroutine was developed and numerical analysis was performed in connection with the AQWA program.

## 2. Numerical Analysis Model

The motion response of the combined wind-wave energy platform was calculated by performing numerical modeling for the platform combining four hemispherical Wavestar-type WECs with a single TLP-type wind turbine model. Figs. 1 and 2 show the geometry of each

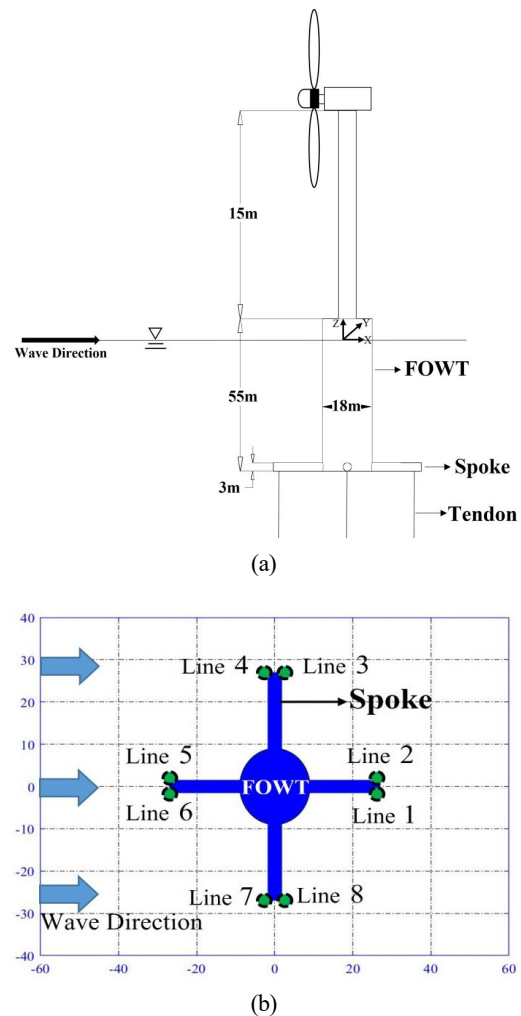


**Fig. 1** Numerical model of a single FOWT and mooring line layout: (a) Single platform (FOWT-Only); (b) Mooring line layout (Top view)

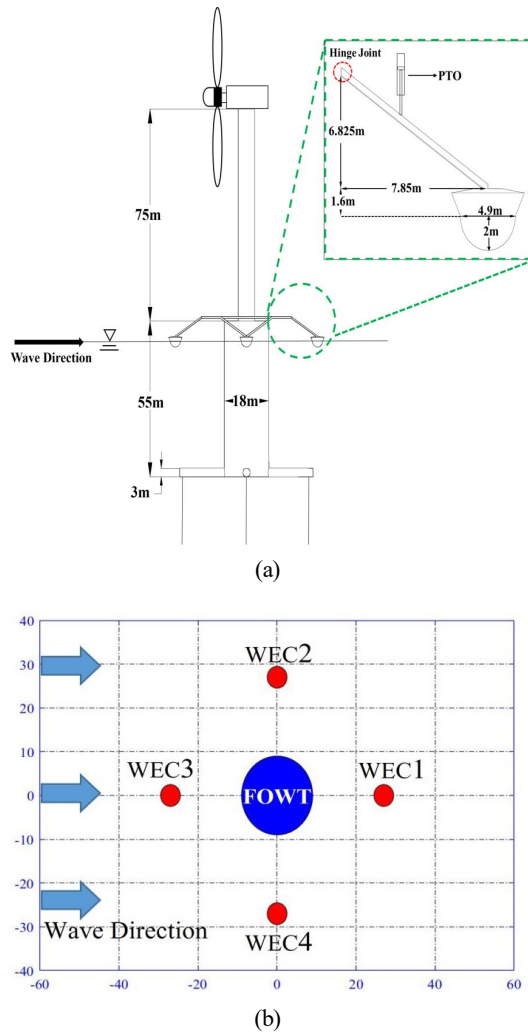


**Fig. 2** Numerical model of a combined energy platform and top view of WEC location: (a) Combined energy platform (FOWT+4WECs); (b) WEC layout (Top view)

numerical model and its main dimensions. Fig. 1(a) shows the single FOWT model, while Fig. 1(b) shows the mooring line layout. For this TLP-type structure, eight vertical tendons are connected from the spokes of the platform to the seabed. Fig. 2(a) shows the combined platform with WECs, while Fig. 2(b) shows the WEC layout. WEC3 is located in front of the incident wave direction, while WEC2 is located on the side of FOWT. In this study, the motion response of WEC3 and WEC2 and their interaction with FOWT were investigated because they are affected most significantly by the incident wave. The combined platform model and single platform model are the same TLP-type structures, and a 5MW-class wind turbine is attached to the top of the platform. As for the main dimensions of the wind turbine, the specifications provided by NREL (Jonkman et al., 2009) were used. In this study, however, the wind load was not considered, and the wind turbine and tower were assumed rigid bodies to identify the motion response characteristics of the platform under the 2<sup>nd</sup>-order wave loads.

Considering the specifications of TLP, the buoyancy of the floating body is larger than its weight, which causes the pretension of mooring

**Table 1** Main properties of FOWT and WEC

Floating offshore wind turbine (FOWT)	
Water depth (m)	200
Diameter (m)	18
Draft (m)	47.89
Mass (kg)	9,300,000
Center of gravity (m)	32.76 (below SWL)
Moment of inertia (Roll) ( $\text{kg} \cdot \text{m}^2$ )	7,796,082,917
Moment of inertia (Pitch) ( $\text{kg} \cdot \text{m}^2$ )	7,796,082,917
Moment of inertia (Yaw) ( $\text{kg} \cdot \text{m}^2$ )	363,384,838
Mooring system type	Tension-leg
Number of mooring lines	8 (4 pairs)
Mooring line diameter(m)	0.127
Mooring line mass per unit length (kg)	116
Mooring line extensional stiffness (kN)	1,500,000
Mooring line pretension (N)	4,500,000
Wave energy converter (WEC)	
Diameter (m)	4.9
Draft (m)	2.0
Length of the arm (m)	10.4
Floater and arm mass (kg)	27,500
Moment of inertia (Pitch) ( $\text{kg} \cdot \text{m}^2$ )	2,450,000

**Table 2** Natural frequencies of the combined platform and single FOWT

Mode	Model Case	Natural frequency (rad/s)
Surge	FOWT + 4WECs	0.11
	FOWT-Only	0.11
Heave	FOWT + 4WECs	2.53
	FOWT-Only	2.55
Pitch	FOWT + 4WECs	1.72
	FOWT-Only	1.76
Rotational response (Pitch) (One-dimensional motion)	Hinged WEC	1.26

lines. In other words, buoyancy can be expressed as the sum of the pretension of mooring lines and the weight of the floating body. Table 1 lists the mass properties of each structure and the specifications of mooring lines (Matha et al., 2010).

The natural frequencies of the combined and single FOWT models used in this study for surge, heave, and pitch were calculated through the free decay test, as listed in Table 2.

For the combined energy platform, four hemispherical buoy-type (Wavestar type) WECs were attached around the tower (FOWT). Each WEC was constrained with a hinge joint, so only one-dimensional rotational motion could be possible with respect to FOWT. A hydraulic cylinder was used as PTO acting on WEC; Table 3 lists its

**Table 3** Hydraulic cylinder condition for WEC PTO

Hydraulic cylinder area (m <sup>2</sup> )	0.0196
Hydraulic pressure difference (kPa)	0-32,000

main specifications (Hansen et al., 2013). The hydraulic cylinder was installed at the 1/3 position of the arm. Coulomb damping force was used for the modeling of PTO system.

### 3. Numerical Analysis Method

Fig. 3 shows the process for calculating the motion response of the combined energy platform in the time domain. The WEC attached to FOWT is a hemispherical buoy-type (Wavestar type) that changes its wetted body surface depending on the wave motion. Therefore, it is important to calculate nonlinear external force considering the wetted surface of the floating body at each time step (Giorgi and Ringwood, 2018). In other words, the wave force is divided into a diffraction force and Froude-Krylov force, and a nonlinear Froude-Krylov force that considers the change in the wetted surface of the floating body was considered in this study. Therefore, the motion response of the platform was calculated by applying a nonlinear external force, and the AQWA-NAUT program capable of multi-body dynamics analysis was used to calculate the constraint force acting on FOWT due to the motion of the attached WEC.

In addition, a user subroutine was developed and calculated to apply the 2<sup>nd</sup>-order wave force that cannot be considered in the AQWA-NAUT program to the platform in time domain analysis. The time-series data of the 2<sup>nd</sup>-order wave force acting on FOWT were calculated by substituting the quadratic transfer function (QTF) of the external force calculated in AQWA-LINE into AQWA-DRIFT. They were applied to the combined energy platform at each time step to calculate its motion response. In addition, the Coulomb damping equation (Kim et al., 2021) was substituted by setting WEC PTO as a hydraulic cylinder model. In the section below, specific calculation formulas were described.

### 3.1 Hydrodynamic Force Calculation Process

A 2<sup>nd</sup>-order transfer function was obtained using AQWA-LINE to calculate the 2<sup>nd</sup>-order wave force acting on the platform. The boundary integral equation to solve the diffraction and radiation problems for deriving the 1<sup>st</sup>-order hydrodynamic coefficient is as follows. In addition, the boundary conditions of the platform are given by Eq. (2).

Diffraction problem boundary integral equation

$$2\pi\phi_s + \iint_{S_b} \phi_s \frac{\partial G}{\partial n} ds = - \iint_{S_b} \phi_o \frac{\partial G}{\partial n} ds + 2\pi\phi_o \quad (1)$$

$$\frac{\partial \phi_D}{\partial n} = 0, \quad \phi_O + \phi_S = \phi_D \quad (2)$$

where  $\phi_o$  is the incident wave potential;  $\phi_s$  is the diffracted wave potential, and  $S_b$  is the wetted surface area of the structure.  $G$  indicates the Green function and  $n$  is the normal vector perpendicular to the surface of the body. The Green function used is expressed as Eq. (3).

$$G(\vec{X}; \vec{X}_0) \quad (3)$$

$$= \frac{1}{r} + \frac{1}{r'} + \frac{2K}{\pi} \int_0^\infty \frac{(k+K) \cosh k(z+h) \cos(z_o+h)}{k \sinh kh - K \cosh kh} e^{-kh} J_0(kR) dk$$

$$r = \sqrt{(x-x_o)^2 + (y-y_o)^2 + (z-z_o)^2}$$

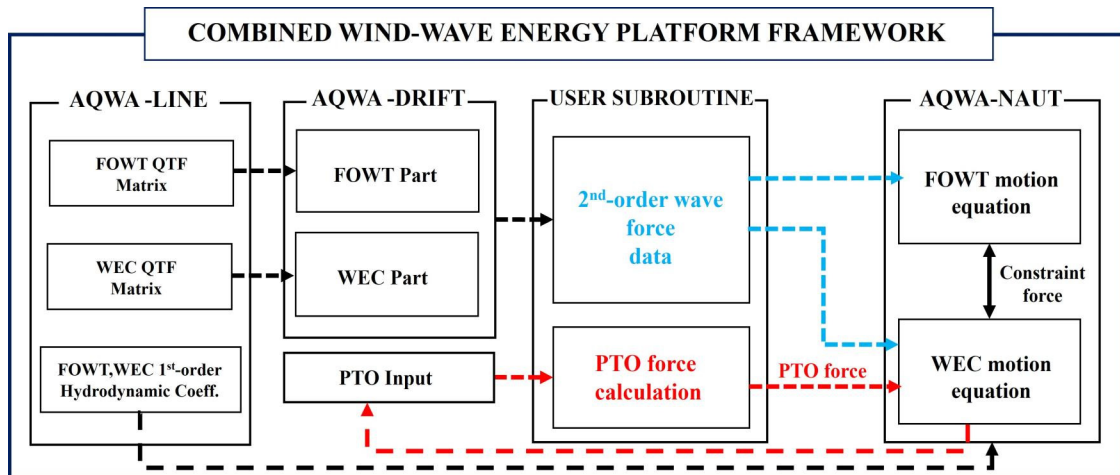
$$r' = \sqrt{(x-x_o)^2 + (y-y_o)^2 + (z+z_o+2h)^2}$$

$$R = \sqrt{(x-x_o)^2 + (y-y_o)^2}$$

$$K = \frac{\omega^2}{g}, \quad k = \text{wavenumber}$$

Radiation problem boundary integral equation

$$2\pi\phi_j + \iint_{S_b} \phi_j \frac{\partial G}{\partial n} ds = - \iint_{S_b} n_j G ds \quad (4)$$


**Fig. 3** Framework of a calculation process for motion analysis of a combined wind-wave energy platform

$$\frac{\partial \phi_R}{\partial n} = \vec{v} \cdot \vec{n}, \quad \phi_R = i\omega \sum_{m=1}^M \sum_{j=1}^6 \epsilon_{jm} \phi_{jm} \quad (5)$$

The integral boundary equation to obtain the 1<sup>st</sup>-order radiation force coefficient is given by Eq. (4). In this case, the boundary conditions of the floating body are given by Eq. (5).  $\phi_R$  is the radiated wave potential and  $\phi_j$  is the radiated wave potential of the body according to each motion mode.  $\epsilon_j$  is the unit amplitude of the body motion and  $j$  is the motion mode.  $j = 1$  and 3 indicate the translational directions of the x-axis and z-axis, while  $j = 4$  and 6 indicate rotational directions. In addition, when there are  $m$  floating bodies, including FOWT and multiple WECs, the radiated wave potential in consideration of the hydrodynamic interaction between each floating body can be expressed as a coupling term as in Eq. (5) through linear superposition.

### 3.2 Second-order Hydrodynamic Coefficient Calculation

The 2<sup>nd</sup>-order wave force of the combined platform ( $F_{EX}^2$ ) was calculated in the time domain by substituting the 2<sup>nd</sup>-order transfer function calculated in AQWA-LINE into AQWA-DRIFT through Eqs. (6) and (7).

$$F_{EX}^2 = \sum_{j=1}^{N_m} \sum_{k=1}^{N_n} F_{jk}^2 \quad (6)$$

$$\begin{aligned} F_{jk}^2 &= a_j a_k (P_{jk}^+ \cos[(\omega_j + \omega_k)t - (\alpha_j + \alpha_k)] \\ &\quad + Q_{jk}^+ \cos[(\omega_j + \omega_k)t - (\alpha_j + \alpha_k)] \\ &\quad + P_{jk}^- \cos[(\omega_j + \omega_k)t - (\alpha_j + \alpha_k)] \\ &\quad + Q_{jk}^- \cos[(\omega_j + \omega_k)t - (\alpha_j + \alpha_k)]) \end{aligned} \quad (7)$$

where  $P_{jk}^+$  and  $Q_{jk}^+$  are the real and imaginary parts of the 2<sup>nd</sup>-order sum-frequency wave load generated between the  $j$ -th and  $k$ -th wave components.  $P_{jk}^-$  and  $Q_{jk}^-$  are the real and imaginary parts of the 2<sup>nd</sup>-order difference-frequency wave load.  $a_j$  and  $a_k$  are the amplitudes of the  $j$ -th and  $k$ -th wave components.  $\omega_j$  and  $\omega_k$  are the frequencies of the  $j$ -th and  $k$ -th wave component.  $\alpha_j$  and  $\alpha_k$  are the phase angles of the  $j$ -th and  $k$ -th wave components, respectively.

### 3.3 Equation of Motion of the Platform

To calculate the equation of motion of the combined energy platform in the time domain, the input values obtained through the user subroutine were substituted into AQWA-NAUT program. Eqs. (8) and (9) are the equations of motion that include all loads acting on FOWT and WECs.

$$\begin{aligned} (m_F + m_{F,a})\ddot{x} &= F_{F,FK}^1 + F_{F,DIFF}^1 + F_{F,EX}^2 \\ &\quad + F_{F,R} + F_{F,STIFF} + F_{MOOR} + F_{F,CONS} \end{aligned} \quad (8)$$

$$\begin{aligned} (m_W + m_{W,a})\ddot{x} &= F_{W,FK}^1 + F_{W,DIFF}^1 \\ &\quad + F_{W,EX}^2 + F_{W,R} + F_{W,CONS} + F_{PTO} \end{aligned} \quad (9)$$

where  $m_F$  and  $m_W$  are the masses of FOWT and WEC, respectively.  $m_{F,a}$  and  $m_{W,a}$  are the added masses of FOWT and WEC.  $F_{F,FK}^1$  and  $F_{W,FK}^1$  indicate the Froude-Krylov forces,  $F_{F,DIFF}^1$  and  $F_{W,DIFF}^1$  are the diffraction forces of FOWT and WEC, respectively. In addition,  $F_{F,EX}^2$  and  $F_{W,EX}^2$  indicate the 2<sup>nd</sup>-order wave forces, and  $F_{F,R}$  and  $F_{W,R}$  denote the radiation-damping forces.  $F_{F,STIFF}$  and  $F_{W,STIFF}$  are the restoring forces acting on each structure, and  $F_{W,STIFF}$  is the mooring load acting on FOWT due to mooring line motion. Finally,  $F_{F,CONS}$  and  $F_{W,CONS}$  are constraint forces acting on FOWT and WEC, respectively, due to the motion of FOWT and WEC. These constraint forces are acting at the hinge joint where FOWT and WEC are connected.

In addition, the Froude-Krylov force, which can be expressed as the incident wave force, is calculated for the wetted surface of the floating body that changes at each time step through the incident wave potential and Bernoulli equation, as shown in Eq. (10). The diffraction force was calculated considering the mean wetted surface area of the floating body through the diffracted wave potential and Bernoulli equation, as shown in Eq. (11).

$$F_{F,FK}^1 = -i\omega\rho \iint_{S_{FB}} \phi_o n_i dS, \quad F_{W,FK}^1 = -i\omega\rho \iint_{S_{WB}} \phi_o n_i dS \quad (10)$$

$$F_{F,DIFF}^1 = -i\omega\rho \iint_{S_{FBMEAN}} \phi_s n_i dS, \quad F_{W,DIFF}^1 = -i\omega\rho \iint_{S_{WBMEAN}} \phi_s n_i dS \quad (11)$$

In the time domain, the radiation-damping force can be calculated as a convolution integral, as shown in Eq. (12).  $\dot{x}_F(\tau)$  and  $\dot{x}_W(\tau)$  are the velocities of FOWT and WEC at time  $\tau$ , respectively. The retardation function  $R(t)$  can be calculated using the radiation damping coefficient  $B(\omega)$  as shown in Eq. (13). The radiation damping force can be calculated in the same way for both FOWT and WEC, which was calculated by applying each radiation damping coefficient.

$$F_{F,R} = - \int_0^t (R(t-\tau) \cdot \dot{x}_F(\tau)) d\tau, \quad (12)$$

$$F_{W,R} = - \int_0^t (R(t-\tau) \cdot \dot{x}_W(\tau)) d\tau$$

$$R(t) = \frac{2}{\pi} \int_0^\infty B(\omega) \frac{\sin(\omega t)}{\omega} d\omega \quad (13)$$

The restoring force of FOWT consists of  $k_{hydrostatic}$ , which is the restoring force by the hydrostatic force acting on the floating body, and  $k_{mooring}$ , which is the mooring restoring force caused by the mooring lines, as shown in Eq. (14). The restoring force of WEC includes the restoring force by a hydrostatic force and the PTO force (Eq. 21), as



shown in Eq. (15).  $x_F(t)$  and  $x_W(t)$  are the displacements of FOWT and WEC at time  $t$ .

$$F_{F,STIFF} = -(k_{F,hydrostatic} + k_{mooring}) x_F(t) \quad (14)$$

$$F_{W,STIFF} = -(k_{W,hydrostatic}) x_W(t) \quad (15)$$

The translational and rotational forces acting on FOWT due to the motion of mooring lines are given by Eqs. (16) and (17) (Ran, 2000).  $[K^L]$  is the linear stiffness matrix between FOWT and mooring lines, and  $[\tilde{P}]$  is the position matrix between FOWT and mooring lines.  $[K^R]$  is the rotational stiffness matrix between FOWT and mooring lines, and  $[\tilde{R}]$  is the rotation matrix between FOWT and mooring lines. In addition,  $[\tilde{C}]$  and  $[\tilde{D}]$  are the translational and rotational motion matrices of FOWT.

$$F_{MOOR/translation} = -[K^L][\tilde{P}] \quad (16)$$

$$F_{MOOR/moment} = -[K^R][\tilde{R}][\tilde{C}] + [k^R][\tilde{R}][\tilde{D}] \quad (17)$$

FOWT and WEC are constrained by a hinge joint, as mentioned above. This causes  $F_{F,CONS}$  and  $F_{W,CONS}$ , which are constraint forces acting on FOWT and WEC, affecting the motion of FOWT and WEC, respectively. The constraint forces occur at the joint of FOWT and WEC, can be calculated using Eq. (18) (Ansys, 2016).  $F_j$  and  $F_k$  are the resultant forces acting on FOWT and WEC, excluding the constraint forces.  $[U_j]$  and  $[U_k]$  indicate the six-degree-of-freedom motions of FOWT and WEC, respectively.  $\begin{bmatrix} K_{jj} & K_{jk} \\ K_{kj} & K_{kk} \end{bmatrix}$  is the stiffness matrix between the two floating bodies.  $H$  is the boundary condition matrix for the constraints.  $R_j$  and  $R_k$  are the local coordinate system vectors at the joint of FOWT and WEC, respectively.  $E$  is the unit position coordinate matrix at the joint.  $G$  is a matrix for defining hinge constraints (ANSYS, 2016).

$$\begin{bmatrix} K_{jj} & K_{jk} & -H_j^T \\ K_{kj} & K_{kk} & H_k^T \\ H_j - H_k & 0 & 0 \end{bmatrix} \begin{bmatrix} U_j \\ U_k \\ F_{F,CONS} \end{bmatrix} = \begin{bmatrix} F_j \\ F_k \\ 0 \end{bmatrix}, \quad \begin{bmatrix} K_{kk} & K_{kj} & -H_k^T \\ K_{jk} & K_{jj} & H_j^T \\ H_k - H_j & 0 & 0 \end{bmatrix} \begin{bmatrix} U_k \\ U_j \\ F_{W,CONS} \end{bmatrix} = \begin{bmatrix} F_k \\ F_j \\ 0 \end{bmatrix} \quad (18)$$

$$H_j = \begin{bmatrix} E^T & E^T R_j \\ 0 & G^T \end{bmatrix}, \quad H_k = \begin{bmatrix} E^T & E^T R_k \\ 0 & G^T \end{bmatrix} \quad (19)$$

$$E = \begin{bmatrix} e_{11} & e_{12} & e_{13} \\ e_{21} & e_{22} & e_{23} \\ e_{31} & e_{32} & e_{33} \end{bmatrix}, \quad G = \begin{bmatrix} 0 & e_{12} & e_{13} \\ 0 & e_{22} & e_{23} \\ 0 & e_{32} & e_{33} \end{bmatrix} \quad (20)$$

The PTO force acting on WEC was implemented through the Coulomb damping force equation (Kim et al., 2021).  $G_{pto}$  is the Coulomb damping force gradient according to the velocity of WEC.  $\Delta p$  and  $S_c$  are the pressure difference and cross-sectional area of the hydraulic cylinder of the PTO system, respectively.

$$F_{PTO} = -\min(G_{pto}|\dot{z}|, \Delta p S_c) \text{sign}(\dot{z}) \quad (21)$$

where  $\dot{z}$  is the vertical velocity of WEC.

## 4. Numerical Analysis Results

### 4.1 Verification of the Motion Analysis of the Single Platform Model (FOWT-Only)

Before motion analysis of the combined energy platform model and the single platform model (FOWT-Only), the motion response of the single platform model to regular waves in the time domain was compared with the calculation results of FAST (Jonkman and Buhl, 2005), an open-source program provided by NREL, as shown in Fig. 4. The comparison was performed under the following conditions, and the validity of the calculation was verified: the representative condition of the target sea state (a wave height of 4 m and a wave period of 8 seconds) and the long wave condition (a wave height of 6 m and a wave period of 15 seconds) were considered in this study. In addition, the response of the platform for surge, heave, and pitch was compared while the wind load acting on the wind turbine was not considered, and the turbine and tower were assumed to be rigid bodies. The results were in good agreement with the FAST calculation results. The heave response, however, is slightly different from the FAST results. This result appears to be because the buoyancy of the spokes, which was not considered in the FAST model, was included in the TLP structures of the combined and single platform models. Therefore, the initial tension of mooring lines to offset this effect was increased by approximately 10% compared to the FAST model. In other words, the initial tension difference corresponding to the offset of the buoyancy of the appendage for the same calculation conditions partially affected the calculation results. In addition, each response is slightly different from the FAST results under the conditions of a wave height of 4 m and a wave period of 8 seconds. This result was attributed to the external force acting on the platform being slightly different from the nonlinear Froude-Krylov force. The nonlinear restoring force by the floating body motion was also included in this study. Nevertheless, there is no significant difference between the two calculation results, indicating that the analysis method used in this study is reliable.

### 4.2 Analysis of the Motion Responses of the Combined Energy Platform

Calculations were performed according to each load condition and WEC attachment to examine the effect of 2<sup>nd</sup>-order wave loads on the motion response of the combined energy platform. The wind load acting on the wind turbine was excluded in the analysis to precisely identify the influence of 2<sup>nd</sup>-order wave loads on the platform motion response. In this study, the following three load conditions were used: 1<sup>st</sup>-order wave load (LC1), 2<sup>nd</sup>-order difference-frequency wave load in addition to the 1<sup>st</sup>-order wave load (LC2), and both 2<sup>nd</sup>-order difference-frequency and sum-frequency wave loads in addition to the 1<sup>st</sup>-order wave load (LC3). Detailed load conditions are described in

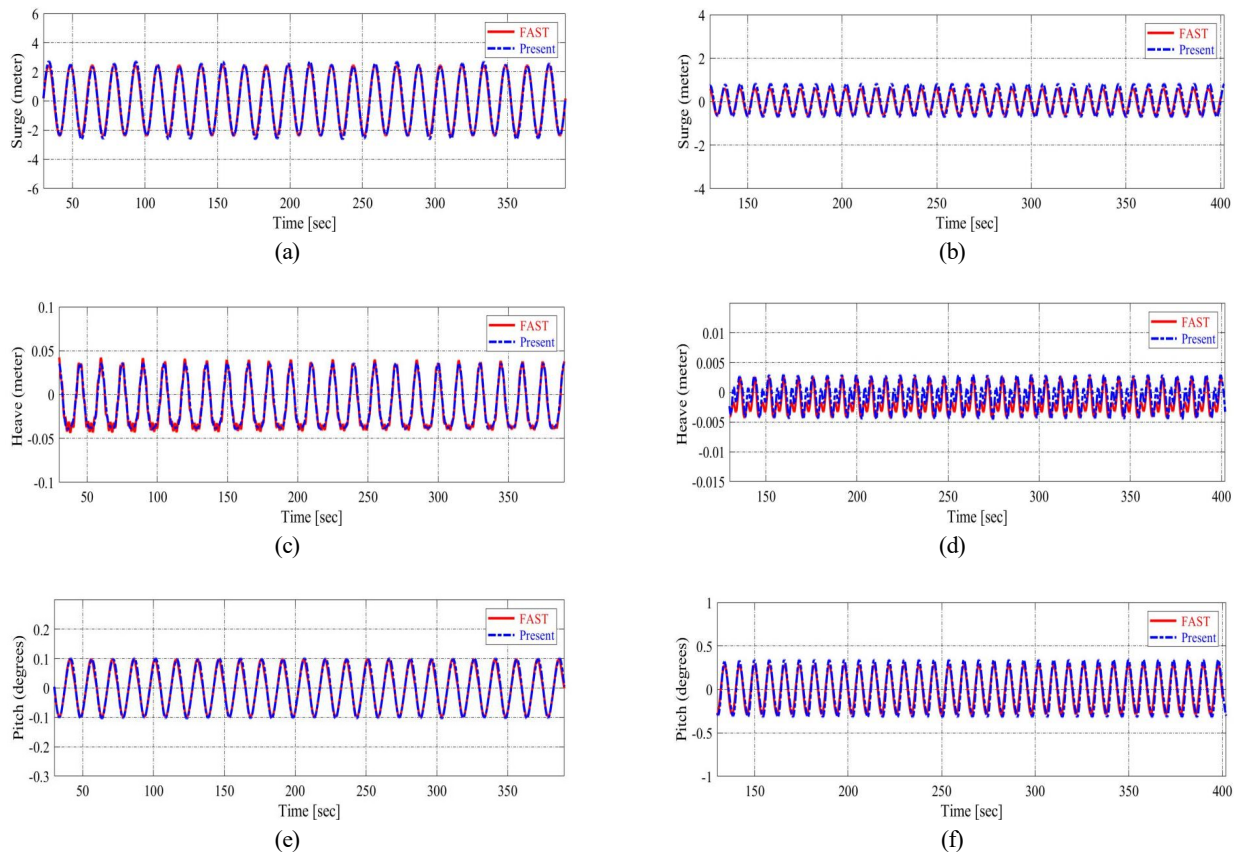


**Fig. 4** Comparison of motion response of FOWT-Only between the present and FAST results (No wind condition): (a) Surge ( $H = 6$  m,  $T = 15$  s); (b) Surge ( $H = 4$  m,  $T = 8$  s); (c) Heave ( $H = 6$  m,  $T = 15$  s); (d) Heave ( $H = 4$  m,  $T = 8$  s); (e) Pitch ( $H = 6$  m,  $T = 15$  s); (f) Pitch ( $H = 4$  m,  $T = 8$  s)

**Table 4** List of load cases

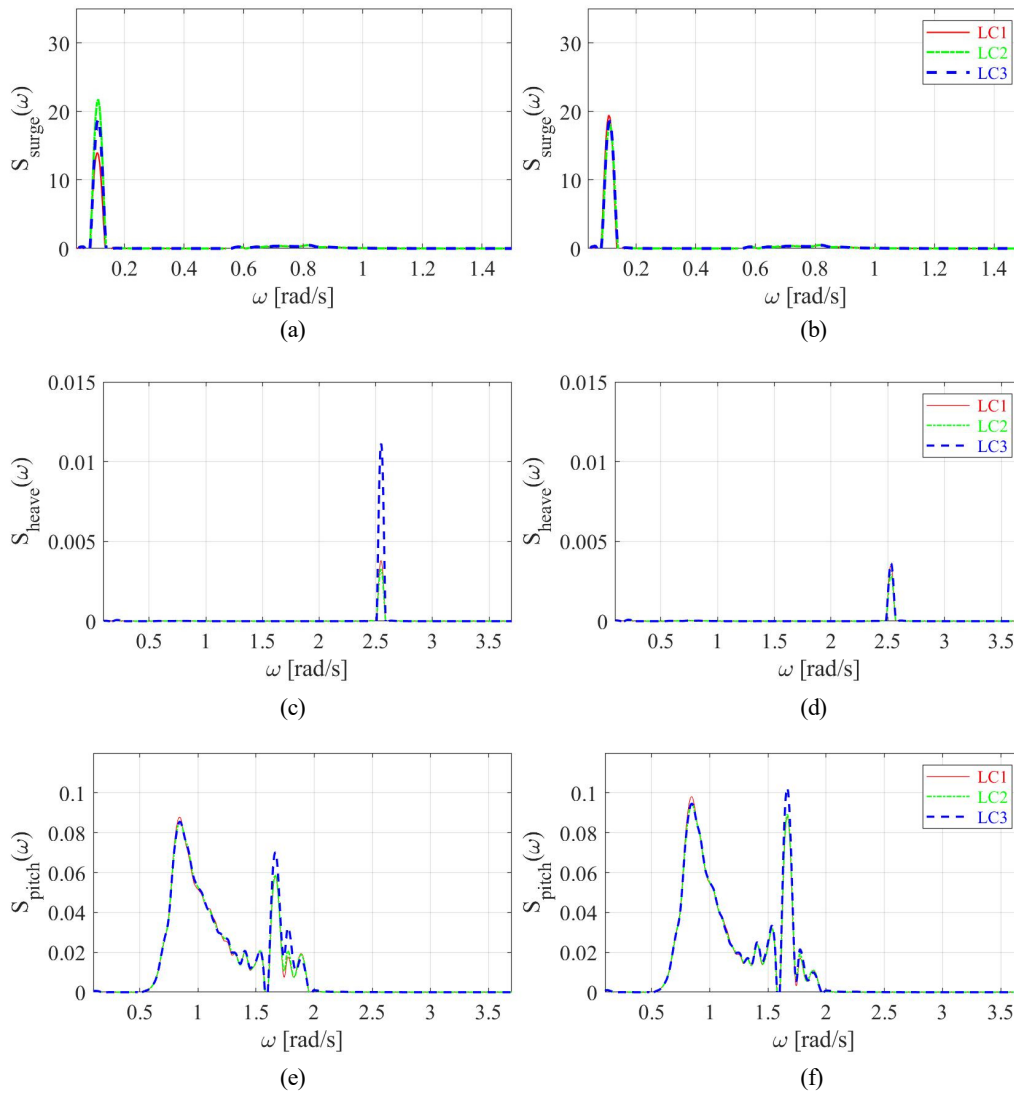
Load case	Forces applied
LC1	1 <sup>st</sup> -order wave excitation force
LC2	1 <sup>st</sup> -order wave excitation force + 2 <sup>nd</sup> -order difference-frequency wave force
LC3	1 <sup>st</sup> -order wave excitation force + 2 <sup>nd</sup> -order difference- and sum-frequency wave force

Table 4. These load conditions were applied to the combined and single platform models. Mooring line tension changes and characteristics of the motion response were mainly compared. The environmental conditions were selected by referring to a previous study that performed TLP analysis with specifications similar to this numerical model. The environmental conditions used were the JONSWAP spectrum with a significant wave height of 4 m, a peak period of 7.5 seconds, and a gamma of 2 (Bae and Kim, 2013). In addition, all incident waves were introduced in the x-axis direction.

The time-series data of motion response of the combined and single platform models were calculated in the time domain. They were converted to motion response spectra and compared in Fig. 5. Fig. 5(a) and 5(b) show the results of the surge responses of the platforms. For both the combined and single platforms, a large motion response

occurred near the natural frequency (0.11 rad/s), while the response in the peak frequency of the incident wave ( $7.5$  s = 0.83 rad/s) was negligible. When only the 1<sup>st</sup>-order wave load (LC1) was applied to the combined platform, the surge response was larger than that of the single platform. This is because the horizontal force acting on the entire platform is larger than the single platform under the influence of WECs. The surge response of the single platform tended to be larger when LC2 was applied than when LC1 was applied. The response of the single platform in the natural frequency range decreased when LC3 was applied compared to when LC2 was applied. In the case of the combined platform, however, the magnitude of the surge response in the natural frequency range hardly changed regardless of the presence or absence of the 2<sup>nd</sup>-order wave load. This is because the WEC PTO of the combined platform offsets the effect of the 2<sup>nd</sup>-order sum-frequency load.

Fig. 5(c) and 5(d) compare the heave responses of the platforms. Similar to the surge response, the heave response was large in the natural frequency range (2.5 rad/s). This indicates that a large response occurred at the natural frequency because of the characteristics of the TLP platform. The magnitude of the response was negligible in the peak frequency range of the incident wave (0.83 rad/s) because it was far from the natural frequency of the platform. For both the combined and single platforms, the magnitude of the heave response did not



**Fig. 5** Comparison of the response spectra under various load conditions: (a) Surge (FOWT-Only); (b) Surge (FOWT+4WECs); (c) Heave (FOWT-Only); (d) Heave (FOWT+4WECs); (e) Pitch (FOWT-Only); (f) Pitch (FOWT+4WECs)

change significantly when LC1 and LC2 were applied. When LC3 was applied to the single platform, however, the magnitude of the heave response was increased by approximately three times. This result was attributed to a phenomenon in which the load increases under the influence of the slowly decaying second-order pressure field as the incident wave is reflected from the cylinder-shaped floating body, and it has already been reported in several studies (Min and Koo, 2022; Koo and Kim, 2007; Kim, 1993, Kim and Yue, 1989). The motion characteristics of TLP structures respond to 2<sup>nd</sup>-order sum-frequency wave loads. In the case of the combined platform model with WECs, however, the effect of the 2<sup>nd</sup>-order sum-frequency wave load can hardly be observed. This appears to be due to the influence of WEC PTO, and the analysis of this phenomenon is described below.

Similar to surge and heave responses, the pitch responses of the platforms (Fig. 5(e) and 5(f)) were observed in the pitch natural frequency of the floating body (1.7 rad/s) and the peak frequency of the incident wave (0.83 rad/s). The magnitude of the pitch response at the peak frequency, however, is similar to that at the natural frequency.

This appears to be because the peak frequency of the incident wave is relatively close to the natural frequency, and a relatively large pitch occurs in the incident wave spectrum. No significant change was observed in the pitch response under the application of the 2<sup>nd</sup>-order wave loads for single and combined platforms. The pitch response, however, slightly increased in the combined platform compared to the single platform. This result was attributed to the motion response (pitch) of WECs in the peak frequency (0.83 rad/s), as mentioned in section 4.3, affecting the pitch increase of the combined platform. WEC attachment also appears to slightly increase the pitch of the combined platform in the pitch natural frequency (1.7 rad/s) of the floating body.

Therefore, regarding the surge response of the TLP-type platform, the motion of the single platform model tends to increase under the influence of 2<sup>nd</sup>-order wave loads. In particular, when the 2<sup>nd</sup>-order sum-frequency wave load was applied, the heave response in the natural frequency range tended to increase dramatically. The heave of the combined platform with WECs was not affected significantly by

the 2<sup>nd</sup>-order wave loads. In the case of pitch, the influence of the 2<sup>nd</sup>-order wave loads was negligible for both models, but the response of the combined platform was slightly larger than the single platform.

4.3 FOWT and WEC Motion Analysis According to the Presence or Absence of WEC PTO

The heave of the single platform model was significantly increased by the 2<sup>nd</sup>-order sum-frequency wave load, but its effect on the combined platform was insignificant. This reason can be explained by the influence of the PTO acting on WEC. Fig. 6 compares the heave response spectra of the combined platform when the WEC PTO force was excluded (w/o PTO) and added (w/ PTO). For the combined platform under the application of LC1, the heave of the platform was significantly reduced when the PTO force was added (Fig. 6(a)). The application of the PTO force also reduced the heave of the combined

platform significantly under the application of LC3 (Fig. 6(b)). The PTO force made the heave of the combined platform smaller than that of the single platform when LC3 was applied. Hence, the PTO force in the combined platform serves as a motion damper that attenuates the heave of the platform.

Fig. 7 compares the rotational motion response spectra of WECs according to the application of the PTO force. WECs operate one-dimensional rotational motion because they are connected to the platform through arms, and the arms are connected to the platform using hinge joints. As shown in Fig. 2, the direction of the motion of WEC2 is perpendicular to the incident wave, while WEC3 is located in front of the incident wave direction. The motion response of WEC2 is similar to that of WEC4 because the arrangement of WECs is symmetrical with respect to FOWT. The response of WEC3, which is expected to be most significantly affected by the incident wave, was

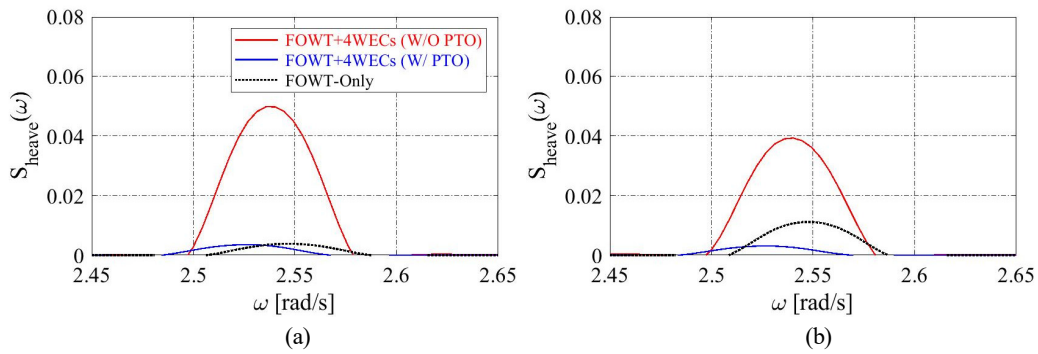


Fig. 6 Comparison of the heave response spectra of a combined platform for WEC PTO force application: (a) LC1 applied; (b) LC3 applied

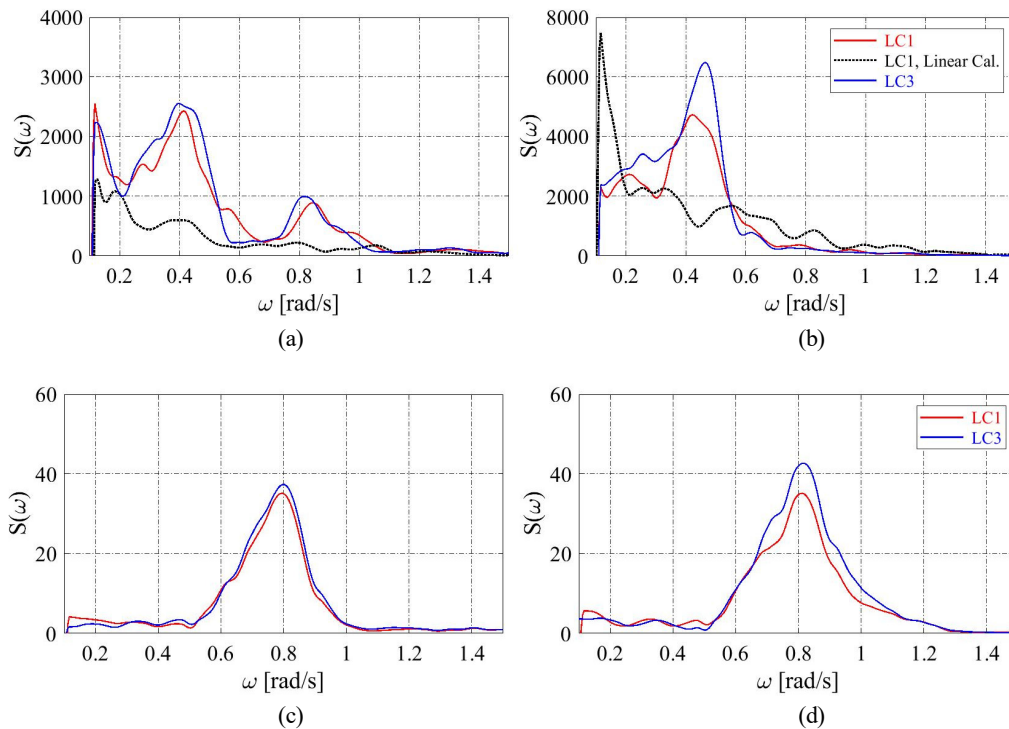


Fig. 7 Comparison of motion spectra of WEC2 and WEC3 for various load conditions (Linear Cal. means application of linear excitation force): (a) WEC3 (w/o PTO); (b) WEC2 (w/o PTO); (c) WEC3 (w/ PTO); (d) WEC2 (w/ PTO)



analyzed. The WEC showed responses at the surge natural frequency of FOWT (0.11 rad/s), half the peak frequency of the incident wave (0.4 rad/s), and the peak frequency of the incident wave (0.83 rad/s).

The motion response of WECs is significantly large when the PTO force is not applied, but the application of the PTO force rapidly decreases the responses in all frequency ranges. Therefore, the PTO force sharply decreases the overall motion response of WECs, and only the response in the peak frequency range of the incident wave occurs (Figs. 7(c) and 7(d)). The rotational response of WECs was slightly larger when LC3 was applied than when LC1 was applied. It appears that the WEC motion response occurred in the surge natural frequency range of the FOWT platform (0.11 rad/s) because WECs are attached to the platform and are thus partially affected by the surge of the platform.

The response that occurs at half the peak frequency of the incident wave is affected by the nonlinear Froude-Krylov force and the nonlinear restoring force of the floating body, and the steepness of the incident wave (Yang et al., 2020). This phenomenon can be explained by the WEC response being reduced rapidly at half the peak frequency of the incident wave if calculation is performed by fixing the wetted surface of the floating body (linear calculation).

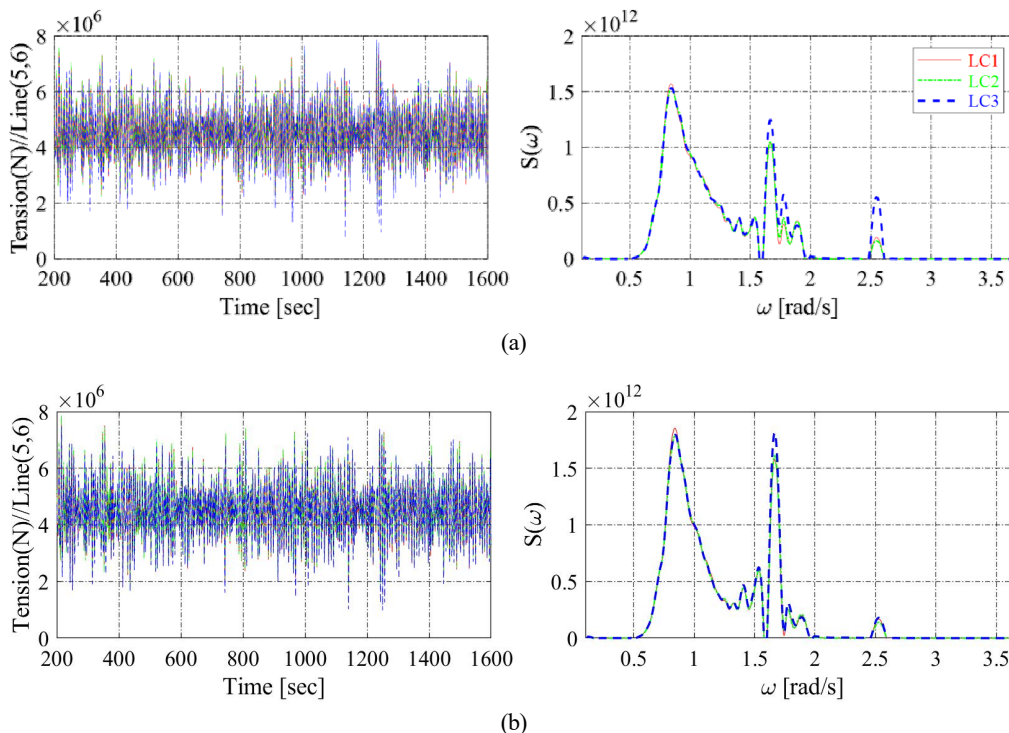
In summary, a comparison of the motion response of the combined platform and WECs according to the presence or absence of PTO confirmed that PTO serves as a heave motion damper of the combined platform and reduces the WEC motion rapidly in all frequency ranges. In addition, as can be seen from the condition without PTO, the WEC motion is affected by the surge natural frequency of FOWT (0.11 rad/s), but FOWT is unaffected by the natural frequency of hinged

WECs (1.26 rad/s). This indicates that the influence of WECs is limited because their size and weight are very small compared to those of FOWT. Moreover, the motion response is larger under the 2<sup>nd</sup>-order wave load condition than the 1<sup>st</sup>-order wave load condition, regardless of the presence or absence of PTO.

#### 4.4 Platform Mooring Line Tension Analysis

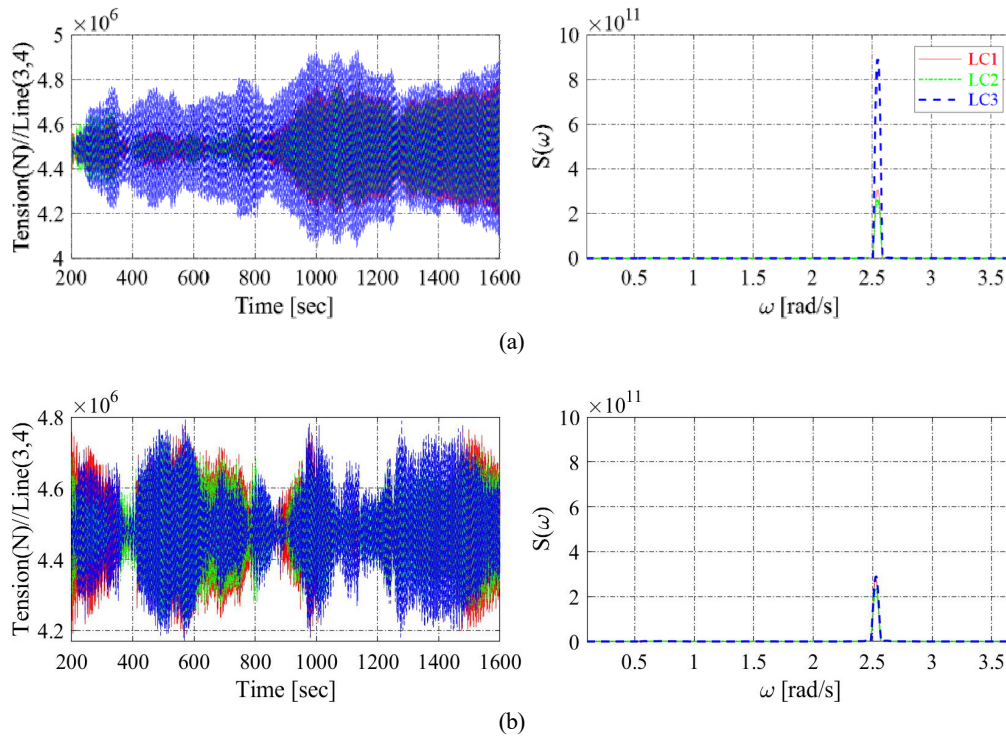
From the mooring line layout in Fig. 1(b), two mooring lines are vertically attached to each of the four spokes. Figs. 8 and 9 compare the time-series data and spectrum for mooring line tension according to the floating body motion. Because the arrangement of mooring lines is symmetrical with respect to FOWT, as with the arrangement of WECs, the results of mooring lines 3 and 4 will be similar to those of mooring lines 7 and 8. The tension of mooring lines 5 and 6, which are expected to be significantly affected by the incident wave, was analyzed. Mooring lines 5 and 6, located in front of the incident wave direction, showed a similar tendency to that of the pitch response spectrum of the platform. An additional response was also observed in the natural frequency range of the heave response spectrum of the platform (2.5 rad/s). This suggests that mooring lines 5 and 6 are affected most significantly by the pitch of the platform and by the heave of the platform to some extent because of their location. Therefore, the mooring line tension in front of the incident wave direction is affected significantly by the 1<sup>st</sup>-order wave load, and the influence of the 2<sup>nd</sup>-order wave loads is insignificant.

Fig. 9 compares the tension time-series data and spectrum for mooring lines 3 and 4, which were installed on the side of the floating body. They generally showed a similar tendency to that of the heave



**Fig. 8** Comparison of time series and response spectrum of lines Nos. 5 and 6 mooring tension (Wave inline direction): (a) FOWT-Only; (b) FOWT+4WECs





**Fig. 9** Comparison of time series and response spectrum of lines Nos. 3 and 4 mooring tension (Side lines): (a) FOWT-Only; (b) FOWT+4WECs

response spectrum of the platform for both the combined and single platforms. This suggests that the mooring lines are affected by the heave of the platform and hardly affected by the surge or pitch of the platform, which can be expected. Therefore, the influence of the 2<sup>nd</sup>-order sum-frequency wave load (LC3), which had a significant impact on the increase in heave of the single platform, acted similarly on mooring lines 3 and 4, increasing the mooring line tension by approximately three times (Fig. 9(a)). This also applies to mooring lines 7 and 8, which are symmetrically installed.

In summary, the mooring line tension in front of the incident wave direction was dominantly affected by the pitch of the platform and partially affected by the heave of the platform. The mooring line tension on the side of the floating body was dominantly affected by the heave of the platform, and the mooring line tension of the single platform (FOWT-Only) increased rapidly under the influence of the 2<sup>nd</sup>-order sum-frequency wave load.

## 5. Conclusion

In this study, motion characteristics were analyzed by applying 2<sup>nd</sup>-order wave loads to identify the precise motion response of a combined wind-wave energy platform based on the TLP structure. The motion response characteristics of single and combined platforms were compared to analyze the change in the motion response of the platform due to the attachment of Wavestar-type WECs. ANSYS AQWA, a hydrodynamic program, was used. A user subroutine was developed for time-domain analysis of the effect of 2<sup>nd</sup>-order wave loads and WEC PTO damping force acting on the combined energy

platform.

The surge response of the platform was large in the natural frequency range for both the combined and single platforms, and the response in the peak frequency range of the incident wave was insignificant. Regarding the motion response of the platform under the application of the 2<sup>nd</sup>-order wave loads, the heave response was found to be large. In particular, the magnitude of the heave response of the single platform increased by approximately three times under the 2<sup>nd</sup>-order sum-frequency wave load. This is because of the influence of the slowly decaying second-order pressure field as the incident wave is reflected from the cylinder-shaped floating body, which was the motion characteristic of the TLP structure. The motion response of the combined platform model, however, was barely affected by the 2<sup>nd</sup>-order sum-frequency wave load because of the influence of the WEC PTO force. The PTO force serves as a heave damper of the combined platform, decreasing the WEC motion in all frequency ranges. The motion response of WECs was slightly larger when the 2<sup>nd</sup>-order wave load was applied than when the 1<sup>st</sup>-order wave load was applied. The mooring line tension in front of the incident wave direction was dominantly affected by the pitch of the platform and partially affected by the heave of the platform. The mooring line tension on the side of the platform was dominantly affected by the heave of the platform, and the mooring line tension of the single platform increased rapidly under the influence of the 2<sup>nd</sup>-order sum-frequency wave load.

This study identified the motion response characteristics of the TLP-type combined wind-wave energy platform according to the attachment of WECs and the influence of 2<sup>nd</sup>-order wave loads.

Through the identification of such motion response characteristics, it is possible to control the excessive mooring line response of the TLP-type wind turbine platforms due to the 2<sup>nd</sup>-order wave loads and to seek more stable energy extraction. Based on this, the motion response characteristics of combined platforms will be analyzed under realistic ocean environmental conditions by adding the aerodynamic load acting on the wind turbine.

### Conflict of Interest

Weoncheol Koo serves as an editor of the Journal of Ocean Engineering and Technology but has no role in the decision to publish this article. No potential conflict of interest relevant to this article was reported.

### Funding

This research was funded and conducted under the Competency Development Program for Industry Specialists of the Korean Ministry of Trade, Industry and Energy (MOTIE), operated by The Korean Institute for Advancement of Technology (KIAT) (No. P0012646, HRD program for Global Advanced Engineer Education Program for Future Ocean Structures). This research was also supported by the Basic Research Project of Science and Engineering, National Research Foundation of Korea (NRF-2018R1D1A1B07040677).

### References

- Adam, F., Myland, T., Dahlhaus, F., & Großmann, J. (2014, November). Gicon®-TLP for wind turbines—the path of development. *In the 1st International Conference on Renewable Energies Offshore (RENEW)* (pp. 24–26).
- Ansys. (2016). *ANSYS aqua theory manual, release 18.2*. ANSYS, Canonsburg.
- Bae, Y.H., & Kim, M.H. (2013). Rotor-floater-tether coupled dynamics including second-order sum-frequency wave loads for a mono-column-TLP-type FOWT (floating offshore wind turbine). *Ocean Engineering*, *61*, 109–122. <https://doi.org/10.1016/j.oceaneng.2013.01.010>
- Chung, W.C., Pestana, G.R., & Kim, M. (2021). Structural health monitoring for TLP-FOWT (floating offshore wind turbine) tendon using sensors. *Applied Ocean Research*, *113*, 102740. <https://doi.org/10.1016/j.apor.2021.102740>
- Ghafari, H.R., Neisi, A., Ghassemi, H., & Iranmanesh, M. (2021). Power production of the hybrid Wavestar point absorber mounted around the Hywind spar platform and its dynamic response. *Journal of Renewable and Sustainable Energy*, *13*(3), 033308. <https://doi.org/10.1063/5.0046590>
- Giorgi, G., & Ringwood, J.V. (2018). Analytical representation of nonlinear Froude-Krylov forces for 3-DoF point absorbing wave energy devices. *Ocean Engineering*, *164*, 749–759. <https://doi.org/10.1016/j.oceaneng.2018.07.020>
- Global Wind Energy Council Global (2019), *Wind Report 2018*, Global Wind Energy Council.
- Hansen, R.H., Kramer, M.M., & Vidal, E. (2013). Discrete displacement hydraulic power take-off system for the wavestar wave energy converter. *Energies*, *6*(8), 4001–4044. <https://doi.org/10.3390/en6084001>
- Jonkman, J. (2010). *Definition of the floating system for phase IV of OC3* (No. NREL/TP-500-47535). National Renewable Energy Lab.
- Jonkman, J., Butterfield, S., Musial, W., & Scott, G. (2009). *Definition of a 5-MW reference wind turbine for offshore system development* (No. NREL/TP-500-38060). National Renewable Energy Lab.
- Jonkman, J. M., & Buhl, Jr, M.L. (2005). *Fast user's guide—updated august 2005* (No. NREL/TP-500-38230). National Renewable Energy Lab.
- Kim, H., Kim, I., Kim, Y.Y., Youn, D., & Han, S. (2016). Simulation and experimental Study of A TLP type floating wind turbine with spoke platform. *Journal of Advanced Research in Ocean Engineering*, *2*(4), 179–191. <https://doi.org/10.5574/JAROE.2016.2.4.179>
- Kim, K.H., Lee, K., Sohn, J.M., Park, S., Choi, J.S., & Hong, K. (2015). Conceptual design of large semi-submersible platform for wave-offshore wind hybrid power generation. *Journal of the Korean Society for Marine Environment & Energy*, *18*(3), 223–232. <https://doi.org/10.7846/JKOSMEE.2015.18.3.223>
- Kim, M.H. (1991). Second-order sum-frequency wave loads on large-volume structures. *Applied ocean research*, *13*(6), 287–296. [https://doi.org/10.1016/S0141-1187\(05\)80052-5](https://doi.org/10.1016/S0141-1187(05)80052-5)
- Kim, M.H. (1993). Second-harmonic vertical wave loads on arrays of deep-draft circular cylinders in monochromatic uni- and multi-directional waves. *Applied ocean research*, *15*(5), 245–262. [https://doi.org/10.1016/0141-1187\(93\)90014-0](https://doi.org/10.1016/0141-1187(93)90014-0)
- Kim, M.H., & Yue, D.K. (1989). The complete second-order diffraction solution for an axisymmetric body Part 1. Monochromatic incident waves. *Journal of Fluid Mechanics*, *200*, 235–264. <https://doi.org/10.1017/S0022112089000649>
- Kim, S.J., Koo, W.C., & Kim, M.H. (2021). The effects of geometrical buoy shape with nonlinear Froude-Krylov force on a heaving buoy point absorber. *International Journal of Naval Architecture and Ocean Engineering*, *13*, 86–101. <https://doi.org/10.1016/j.ijnaoe.2021.01.008>
- Koo, W.C., & Kim, M.H. (2007). Fully nonlinear wave-body interactions with surface-piercing bodies. *Ocean Engineering*, *34*(7), 1000–1012. <https://doi.org/10.1016/j.oceaneng.2006.04.009>
- Lee, H., Cho, I.H., Kim, K.H., & Hong, K. (2016). Interaction analysis on deployment of multiple wave energy converters in a floating hybrid power generation platform. *Journal of the Korean Society for Marine Environment & Energy*, *19*(3), 185–193. <https://doi.org/10.7846/JKOSMEE.2016.19.3.185>

- Matha, D., Fischer, T., Kuhn, M., & Jonkman, J. (2010). *Model development and loads analysis of a wind turbine on a floating offshore tension leg platform* (No. NREL/CP-500-46725). National Renewable Energy Lab.
- Muliawan, M.J., Karimirad, M., & Moan, T. (2013). Dynamic response and power performance of a combined spar-type floating wind turbine and coaxial floating wave energy converter. *Renewable Energy*, 50, 47–57. <https://doi.org/10.1016/j.renene.2012.05.025>
- Min, E.H., & Koo, W.C. (2022). Comparison of wave diffraction forces on a surface-piercing body for various free-surface grid update schemes. *Ocean Engineering*, 259, 111912. <https://doi.org/10.1016/j.oceaneng.2022.111912>
- Oguz, E., Clelland, D., Day, A. H., Incecik, A., López, J.A., Sánchez, G., & Almeria, G.G. (2018). Experimental and numerical analysis of a TLP floating offshore wind turbine. *Ocean Engineering*, 147, 591–605. <https://doi.org/10.1016/j.oceaneng.2017.10.052>
- Park, S., Kim, K.H., & Hong, K. (2018). Conceptual design of motion reduction device for floating wave-offshore wind hybrid power generation platform. *Journal of Ocean Engineering and Technology*, 32(1), 9–20. <https://doi.org/10.26748/KSOE.2018.2.32.1.009>
- Pantusa, D., Francone, A., & Tomasicchio, G.R. (2020). Floating offshore renewable energy farms. A life-cycle cost analysis at Brindisi, Italy. *Energies*, 13(22), 6150. <https://doi.org/10.3390/en13226150>
- Ran, Z. (2000). *Coupled dynamic analysis of floating structures in waves and currents* (Publication No. 9994319) [Doctoral dissertation, Texas A&M University]. ProQuest Dissertations Publishing.
- Robertson, A., Jonkman, J., Masciola, M., Song, H., Goupee, A., Coulling, A., & Luan, C. (2014). *Definition of the semi submersible floating system for phase II of OC4* (No. NREL/TP-5000-60601). National Renewable Energy Lab.
- Si, Y., Chen, Z., Zeng, W., Sun, J., Zhang, D., Ma, X., & Qian, P. (2021). The influence of power-take-off control on the dynamic response and power output of combined semi-submersible floating wind turbine and point-absorber wave energy converters. *Ocean Engineering*, 227, 108835. <https://doi.org/10.1016/j.oceaneng.2021.108835>
- Tsouroukdissian, A.R., Park, S., Pourazarm, P., Cava, W.L., Lackner, M., Lee, S., & Cross-Whiter, J. (2016). *Smart novel semi-active tuned mass damper for fixed-bottom and floating offshore wind* [Conference presentation]. Offshore Technology Conference 2016, Houston, Texas, USA. <https://doi.org/10.4043/26922-MS>
- Ullah, S., Branquinho, R., Mateus, T., Martins, R., Fortunato, E., Rasheed, T., & Sher, F. (2020). Solution combustion synthesis of transparent conducting thin films for sustainable photovoltaic applications. *Sustainability*, 12(24), 10423. <https://doi.org/10.3390/su122410423>
- Yang, J., Teng, B., Gou, Y., Chen, L., & Jin, R. (2020). Half-wave frequency response phenomenon of a tightly moored submerged sphere under monochromatic wave action simulated by using the body-exact approach. *Applied Ocean Research*, 103, 102317. <https://doi.org/10.1016/j.apor.2020.102317>
- Ren, Y., Venugopal, V., & Shi, W. (2022). Dynamic analysis of a multi-column TLP floating offshore wind turbine with tendon failure scenarios. *Ocean Engineering*, 245, 110472. <https://doi.org/10.1016/j.oceaneng.2021.110472>

### Author ORCIDs

Author name	ORCID
Kim, Hongbhin	0000-0003-2180-2638
Min, Eun-Hong	0000-0003-1045-9475
Heo, Sanghwan	0000-0003-0033-5022
Koo, Weoncheol	0000-0002-4384-0996

# Instructions for Authors

## General information

To submit a manuscript to the Journal of Ocean Engineering and Technology (JOET), it is advised to first carefully read the aims and the scope section of this journal, as it provides information on the editorial policy and the category of papers it accepts. Unlike many regular journals, JOET usually has no lag in acceptance of a manuscript and its publication. Authors that find a match with the aims and the scope of JOET are encouraged to submit as we publish works from all over the world. JOET adheres completely to guidelines and best practices published by professional organizations, including Principles of Transparency and Best Practice in Scholarly Publishing (joint statement by COPE, DOAJ, WAME, and OASPA (<http://doaj.org/bestpractice>) if otherwise not described below. As such, JOET would like to keep the principles and policies of those professional organizations during editing and the publication process.

## Research and publication ethics

Details on publication ethics are found in <http://joet.org/authors/ethics.php>. For the policies on research and publication ethics not stated in the Instructions, Guidelines on Good Publication (<http://publicationethics.org/>) can be applied.

## Requirement for membership

One of the authors who submits a paper or papers should be member of the Korean Society of Ocean Engineers (KSOE), except a case that editorial board provides special admission of submission.

## Publication type

Article types include scholarly monographs (original research articles), technical articles (technical reports and data), and review articles. The paper should have not been submitted to other academic journal. When part or whole of a manuscript was already published to conference papers, research reports, and dissertations, then the corresponding author should note it clearly in the manuscript.

## Copyright

After published to JOET, the copyright of manuscripts should belong to KSOE. A transfer of copyright (publishing agreement) form can be found in submission website (<http://www.joet.org>).

## Manuscript submission

Manuscript should be submitted through the on-line submission website (<http://www.joet.org>). The date that manuscript was received through on-line website is the official date of receipt. Other correspondences can be sent by an email to the Editor in Chief or secretariat. The manuscript must be accompanied by a signed statement that it has been neither published nor currently submitted for publication elsewhere. The manuscript should be written in English or Korean. Ensure that online submission are in a standard word processing format. Corresponding author must write the manuscript using the JOET template provided in Hangul or MS Word format. Ensure that graphics are high-resolution.

Be sure all necessary files have been uploaded/ attached.

## Authors' checklist

Please refer to "Authors' Checklist" for details.

## Article structure

Manuscript must be edited in the following order: (1) Title, (2) Authors' names and affiliations, (3) Keywords, (4) Abstract, (5) Nomenclature (optional), (6) Introduction, (7) Main body (analyses, tests, results, and discussions), (8) Conclusions, (9) Conflict of interest, (10) Funding (optional), (11) Acknowledgements (optional), (12) References, (13) Appendices (optional), (14) Author's ORCIDs.

## Abstract

A concise and factual abstract is required. The abstract should state briefly the background, purpose and methods of the research, the principal results and conclusions. An abstract should be written in 150-200 words. References are not cited in abstract whenever possible. Also, non-standard or uncommon abbreviations should be avoided, but if essential they must be defined at their first mention in the abstract itself.

## Keywords

Immediately after the abstract, provide a maximum of 5 or 6 keywords.

## Unit

Use the international system units(SI). If other units are mentioned, please give their equivalent in SI.

## Equations

All mathematical equations should be clearly printed/typed using well accepted explanation. Superscripts and subscripts should be typed clearly above or below the base line. Equation numbers should be given in Arabic numerals enclosed in parentheses on the right-hand margin.

## Tables

Tables should be numbered consecutively with Arabic numerals. Each table should be fully titled. All tables should be referred to in the texts.

## Figures

Figures should be numbered consecutively with Arabic numerals. Each figure should be fully titled. All figures should be referred to in the texts. All the illustrations should be of high quality meeting with the publishing requirement with legible symbols and legends.

## Conflict of interest

It should be disclosed here according to the statement in the Research and publication ethics regardless of existence of conflict of interest. If the authors have nothing to disclose, please state: "No potential

conflict of interest relevant to this article was reported.”

### Funding

Funding to the research should be provided here. Providing a FundRef ID is recommended including the name of the funding agency, country and if available, the number of the grant provided by the funding agency. If the funding agency does not have a FundRef ID, please ask that agency to contact the FundRef registry (e-mail: fundref.registry@crossref.org). Additional detailed policy of FundRef description is available from <http://www.crossref.org/fundref/>. Example of a funding description is as follows: The study is supported by the Inha University research fund (FundRef ID: 10.13039/501100002632), and the Korea Health Personnel Licensing Examination Institute research fund (FundRef ID: 10.13039/501100003647).

### Acknowledgments

Any persons that contributed to the study or the manuscript, but not meeting the requirements of an authorship could be placed here. For mentioning any persons or any organizations in this section, there should be a written permission from them.

### References in text

References in texts follow the APA style. Authors can also see how references appear in manuscript text through the ‘Template’.

### Reference list

Reference list follows the APA style. Authors can see how references should be given in reference section through the ‘Template’.

### Appendices

The appendix is an optional section that can contain details and data supplemental to the main text. If there is more than an appendix, they should be identified as A, B, C, etc. Formulae and equations in appendices should be given separate numbering: Eq. (A1), Eq. (A2), etc.; in a subsequent appendix, Eq. (B1) and so on. Similarly for tables and figures: Table A1; Fig. A1, etc.

### ORCID (Open Researcher and Contributor ID)

All authors are recommended to provide an ORCID. To obtain an ORCID, authors should register in the ORCID web site: <http://orcid.org>. Registration is free to every researcher in the world. Example of ORCID description is as follows:

Joonmo Chung: <https://orcid.org/0000-0003-1407-9031>

### Peer review and publication process

The peer review process can be broadly summarized into three groups: author process, review process, and publishing process for accepted submissions. General scheme is presented in Figure 1.

#### Check-in process for review

If the manuscript does not fit the aims and scope of the Journal or does not adhere to the Instructions to Authors, it may be rejected immediately after receipt and without a review. Before reviewing, all submitted manuscripts are inspected by Similarity Check powered by iThenticate (<https://www.crossref.org/services/similarity-check/>), a plagiarism-screening tool. If a too high degree of similarity score is found, the Editorial Board will do a more profound content screening.

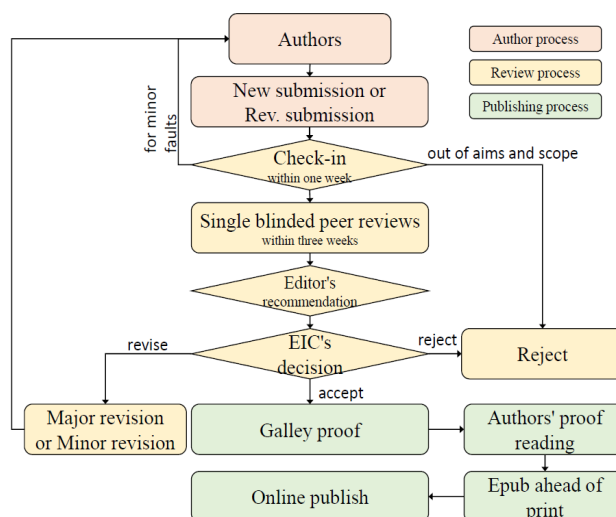


Figure 1 Flow chart of the peer review and publication process of JOET

The criterion for similarity rate for further screening is usually 15%; however, rather than the similarity rate, the Editorial Board focuses on cases where specific sentences or phrases are similar. The settings for Similarity Check screening are as follows: It excludes quotes, bibliography, small matches of 6 words, small sources of 1%, and the Methods section.

#### Number of reviewers

Reviewers will be selected from the list of reviewers. Manuscripts are then peer reviewed by at least 2 experts in the corresponding field, usually by 2.

#### Peer review process and the author response to the reviewer comments

JOET adopts single blind review, which means that the authors do not know the identity of the reviews. All papers, including those invited by the Editor, are subject to peer review.

The review period is 4 weeks. Usually the first decision is made within a week after completion of the review. The Editorial Board's decision after the review will be one of followings: Accept, Minor revision, Major revision, or Rejection. The Editorial Board may request the authors to revise the manuscript according to the reviewers' comments. If there are any requests for revision of the manuscript by the reviewers, the authors should do their best to revise the manuscript. If the reviewer's opinion is not acceptable or is believed to misinterpret the data, the author should reasonably indicate that. After revising the manuscript, the author should upload the revised files with a separate response sheet to each item of the reviewer's commentary. The author's revisions should be completed within 3 months after the request. If it is not received by the due date, the Editorial Board will notify the author. To extend the revision period beyond 3 months, the author should negotiate that with the Editorial Board. The manuscript review process can be provided for up two rounds. If the authors wish further review, the Editorial Board may consider it. The Editorial Board will make a final decision on the approval of the submitted manuscript for publication and can request any further corrections, revisions, and deletions of the article text if necessary. Statistical editing is also performed if the data requires professional statistical review by a statistician.



### *Processing after acceptance*

If the manuscript is finally accepted, the galley proof will be sent to the corresponding author after professional manuscript editing and English proofreading. Proofreading should be performed for any misspellings or errors by the authors. Proofreading manuscript for publication is provided to the corresponding author, and the corresponding author must review the proofreading manuscript. Corresponding authors are responsible for the content of the proofreading manuscript and any errors. After final proofreading, the manuscript may appear at the journal homepage as an article in press with a unique DOI number for rapid communication. All published articles will be replaced by the replacement XML file and a final PDF.

### *Feedback after publication*

If the authors or readers find any errors, or contents that should be revised, it can be requested from the Editorial Board. The Editorial Board may consider erratum, corrigendum or a retraction. If there are any revisions to the article, there will be a CrossMark description to announce the final draft. If there is a reader's opinion on the published article with the form of Letter to the editor, it will be forwarded to the authors. The authors can reply to the reader's letter. Letter to the editor and the author's reply may be also published.

### *How the journal handle complaints and appeals*

The policy of JOET is primarily aimed at protecting the authors, reviewers, editors, and the publisher of the journal. If not described below, the process of handling complaints and appeals follows the guidelines of the Committee of Publication Ethics available from: <https://publicationethics.org/appeals>

#### *- Who complains or makes an appeal?*

Submitters, authors, reviewers, and readers may register complaints and appeals in a variety of cases as follows: falsification, fabrication, plagiarism, duplicate publication, authorship dispute, conflict of interest, ethical treatment of animals, informed consent, bias or unfair/inappropriate competitive acts, copyright, stolen data, defamation, and legal problem. If any individuals or institutions want to inform the cases, they can send a letter via the contact page on

our website: <https://www.joet.org/about/contact.php>. For the complaints or appeals, concrete data with answers to all factual questions (who, when, where, what, how, why) should be provided.

#### *- Who is responsible to resolve and handle complaints and appeals?*

The Editorial Board or Editorial Office is responsible for them. A legal consultant or ethics editor may be able to help with the decision making.

#### *- What may be the consequence of remedy?*

It depends on the type or degree of misconduct. The consequence of resolution will follow the guidelines of the Committee of Publication Ethics (COPE).

### **Article processing charge**

#### *Payment due*

Article processing charge (APC) covers the range of publishing services JOET provides. This includes provision of online tools for editors and authors, article production and hosting, and customer services. Upon editorial acceptance of an article for the regular review service and upon submission of an article for the fast review service, the corresponding author will be notified that payment is due.

#### *APC*

The APC up to 6 pages is ₩300,000 (or \$300) and ₩650,000 (or \$650) for the for the regular and fast review services, respectively. An extra APC of \$100 per page is charged for papers longer than 6 pages. No taxes are included in this charge. For the fast review service, an advance fee of ₩250,000 (\$250) should be paid on submission.

#### *Payment methods*

*Credit card payment* can be made online using a secure payment form as soon as the manuscript has been editorially accepted. We will we send a receipt by email once payment has been processed. Please note that payment by credit card carries a surcharge of 10% of the total APC.

*Invoice payment* is due within 7 days of the manuscript receiving editorial acceptance. Receipts are available on request.

## Title of Article

Firstname Lastname<sup>1</sup>, Firstname Lastname<sup>2</sup> and Firstname Lastname<sup>3</sup>

<sup>1</sup>Professor, Department of OO, OO School, OO University, Busan, Korea

<sup>2</sup>Graduate Student, Department of OO, OO University, Seoul, Korea

<sup>3</sup>Senior Researcher, Department of OO, OO Engineering, Corp., Seoul, Korea

**KEY WORDS:** Lumped mass line model, Explicit method, Steel lazy wave riser (Provide a maximum of 5 or 6 keywords.)

### ABSTRACT:

**\*\*Abstract Construction Guidelines\*\***

- 1) Describe the research background and aims in 1-2 sentences
- 2) Describe the research/analysis method (method section) in 2-3 sentences.
- 3) Describe the research/analysis results (results) in 2-3 sentences.
- 4) Describe the research conclusion in 1-2 sentences.

**\*\*Abstract Editing Guidelines\*\***

- 1) Review English grammar.
- 2) Describe in 150-200 words.
- 3) When using an abbreviation or acronym, write the acronym after full words.
- 4) Abbreviations (acronyms) used only once should be written in full words only, and no acronyms.
- 5) References are not included in the abstract.

### Nomenclature (Optional)

$I_{TOC}$	Increment of total operating cost (\$/yr)
$LHV$	Lower heating value (kJ/kg)
$P_w$	Power (kW)
$T$	Temperature (K)
$V$	Volume (m <sup>3</sup> )
$\rho$	Density (kg/m <sup>3</sup> )

## 1. Introduction

The introduction should briefly place the study in a broad context and highlight why it is important. It should define the purpose of the work and its significance. The current state of the research field should be reviewed carefully and key publications cited. Please highlight controversial and diverging hypotheses when necessary. Finally, briefly mention the main aim of the work and highlight the principal conclusions. As far as possible, please keep the introduction comprehensible to scientists outside your particular field of research.

Received 00 February 2100, revised 00 October 2100, accepted 00 October 2100

Corresponding author Firstname Lastname: +82-51-759-0656, e-mail@e-mail.com

It is a recommended paper from the proceedings of 2019 spring symposium of the Korea Marine Robot Technology (KMRTS).

© 2100, The Korean Society of Ocean Engineers

This is an open access article distributed under the terms of the creative commons attribution non-commercial license (<http://creativecommons.org/licenses/by-nc/4.0>) which permits unrestricted non-commercial use, distribution, and reproduction in any medium, provided the original work is properly cited.

## 2. General Information for Authors

### 2.1 Research and Publication Ethics

Authorship should be limited to those who have made a significant contribution to the conception, design, execution, or interpretation of the reported study. All those who have made significant contributions should be listed as co-authors. Where there are others who have participated in certain substantive aspects of the research project, they should be acknowledged or listed as contributors.

The corresponding author should ensure that all appropriate co-authors and no inappropriate co-authors are included on the paper, and that all co-authors have seen and approved the final version of the paper and have agreed to its submission for publication.

Details on publication ethics are found in the journal's website (<http://joet.org/authors/ethics.php>). For the policies on research and publication ethics not stated in the Instructions, Guidelines on Good Publication (<http://publicationethics.org/>) can be applied.

### 2.2 Requirement for Membership

One of the authors who submits a paper or papers should be member of The Korea Society of Ocean Engineers (KSOE), except a case that editorial board provides special admission of submission.

### 2.3 Publication Type

Article types include scholarly monographs (original research articles), technical articles (technical reports and data), and review articles. The paper should have not been submitted to another academic journal. When part or whole of a manuscript was already published to conference papers, research reports, and dissertations, then the corresponding author should note it clearly in the manuscript.

Example: It is noted that this paper is revised edition based on proceedings of KAOST 2100 in Jeju.

### 2.4 Copyright

After published to JOET, the copyright of manuscripts should belong to KSOE. A transfer of copyright (publishing agreement) form can be found in submission website (<http://www.joet.org>).

### 2.5 Manuscript Submission

Manuscript should be submitted through the on-line submission website (<http://www.joet.org>). The date that manuscript was received through on-line website is the official date of receipt. Other correspondences can be sent by an email to the Editor in Chief or secretariat. The manuscript must be accompanied by a signed statement that it has been neither published nor currently submitted for publication elsewhere. The manuscript should be written in English or Korean. Ensure that online submission is in a standard word processing format. Corresponding author must write the manuscript using the JOET template provided in Hangul or MS Word format. Ensure that graphics are high-resolution. Be sure all necessary files have been uploaded/ attached.

#### 2.5.1 Author's checklist

Author's checklist and Transfer of copyright can be found in submission homepage (<http://www.joet.org>).

## 3. Manuscript

Manuscript must be edited in the following order: (1) Title, (2) Authors' names and affiliations, (3) Keywords, (4) Abstract, (5) Nomenclature (optional), (6) Introduction, (7) Main body (analyses, tests, results, and discussions), (8) Conclusions, (9) Conflict of interest, (10) Funding (optional), (11) Acknowledgements (optional), (12) References, (13) Appendices (optional), (14) Author's ORCID.

### 3.1 Unit

Use the international system units (SI). If other units are mentioned, please give their equivalent in SI.

### 3.2 Equations

All mathematical equations should be clearly printed/typed using well accepted explanation. Superscripts and subscripts should be typed clearly above or below the base line. Equation numbers should be given in Arabic numerals enclosed in parentheses on the right-hand margin. The parameters used in equation must be defined. They should be cited in the text as, for example, Eq. (1), or Eqs. (1)–(3).

$$G_{GEV}(x;\mu,\sigma,\xi) = \begin{cases} \exp[-(1+\xi(x-\mu)/\sigma)^{-1/\xi}] & \xi \neq 0 \\ \exp[-\exp(-(x-\mu)/\sigma)] & \xi = 0 \end{cases} \quad (1)$$

in which  $\mu$ ,  $\sigma$ , and  $\xi$  represent the location (“Shift” in figures), scale, and shape parameters, respectively.

### 3.3 Tables

Tables should be numbered consecutively with Arabic numerals. Each table should be typed on a separate sheet of paper and be fully titled. All tables should be referred to in the texts.

**Table 1** Tables should be placed in the main text near to the first time they are cited

Item	Buoyancy riser
Segment length <sup>1)</sup> (m)	370
Outer diameter (m)	1.137
Inner diameter (m)	0.406
Dry weight (kg/m)	697
Bending rigidity (N·m <sup>2</sup> )	1.66E8
Axial stiffness (N)	7.098E9
Inner flow density (kg·m <sup>3</sup> )	881
Seabed stiffness (N/m/m <sup>2</sup> )	6,000

<sup>1)</sup>Tables may have a footer.

### 3.4 Figures

Figures should be numbered consecutively with Arabic numerals. Each figure should be fully titled. All the illustrations should be of high quality meeting with the publishing requirement with legible symbols and legends. All figures should be referred to in the texts. They should be referred to in the text as, for example, Fig. 1, or Figs. 1–3.

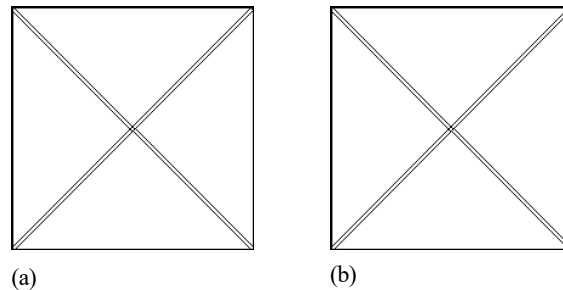


**Fig. 1** Schemes follow the same formatting. If there are multiple panels, they should be listed as: (a) Description of what is contained in the first panel; (b) Description of what is contained in the second panel. Figures should be placed in the main text near to the first time they are cited

### 3.5 How to Describe the References in Main Texts

- JOET recommends to edit authors' references using MS-Word reference or ZOTERO plug-in
- How to add a new citation and source to a document using MS-Word is found in MS Office web page: <https://support.microsoft.com/en-us/office/add-citations-in-a-word-document-ab9322bb-a8d3-47f4-80c8-63c06779f127>
- How to add a new citation and source to a document using ZOTERO is found in zotero web page: <https://www.zotero.org/>

## 4. Results

This section may be divided by subheadings. It should provide a concise and precise description of the experimental results, their interpretation as well as the experimental conclusions that can be drawn. Tables and figures are recommended to present the results more rapidly and easily. Do not duplicate the content of a table or a figure with in the Results section. Briefly describe the core results related to the conclusion in the text when data are provided in tables or in figures. Supplementary results can be placed in the Appendix.

## 5. Discussion

Authors should discuss the results and how they can be interpreted in perspective of previous studies and of the working hypotheses. The findings and their implications should be discussed in the broadest context possible. Future research directions may also be highlighted

## 6. Conclusions

This section can be added to the manuscript.

## Conflict of Interest

It should be disclosed here according to the statement in the Research and publication ethics regardless of existence of conflict of interest. If the authors have nothing to disclose, please state: “No potential conflict of interest relevant to this article was reported.”, “The authors declare no potential conflict of interest.”, “The authors declare that they have no conflict of interests.”

## Funding (Optional)

Please add: “This research was funded by Name of Funder, grant number XXX” and “The OOO was funded by XXX”. Check carefully that the details given are accurate and use the standard spelling of funding agency names at <https://search.crossref.org/funding>

## Acknowledgments (Optional)

In this section you can acknowledge any support given which is not covered by the author contribution or funding sections. This may include administrative and technical support, or donations in kind (e.g., materials used for experiments). For mentioning any persons or any organizations in this section, there should be a written permission from them.

## References

JOET follows the American Psychological Association (APA) style.

- Some samples are found in following web pages: <https://apastyle.apa.org/style-grammar-guidelines/references/examples> or <https://www.ntnu.edu/viko/apa-examples>
- JOET recommends editing authors' references using MS-Word reference or ZOTERO plug-in
- How to add a new citation and source to a document using MS-Word is found in MS Office web page: <https://support.microsoft.com/en-us/office/add-citations-in-a-word-document-ab9322bb-a8d3-47f4-80c8-63c06779f127>
- How to add a new citation and source to a document using ZOTERO is found in ZOTERO web page: <https://www.zotero.org/>

## Appendix (Optional)

The appendix is an optional section that can contain details and data supplemental to the main text. For example, explanations of experimental details that would disrupt the flow of the main text, but nonetheless remain crucial to understanding and reproducing the research shown; figures of replicates for experiments of which representative data is shown in the main text can be added here if brief, or as Supplementary data. Mathematical proofs of results not central to the paper can be added as an appendix.

All appendix sections must be cited in the main text. In the appendixes, Figures, Tables, etc. should be labeled starting with ‘A’, e.g., Fig. A1, Fig. A2, etc.

Examples:

<https://doi.org/10.26748/KSOE.2019.022>

<https://doi.org/10.26748/KSOE.2018.4.32.2.095>



## Author ORCIDs

All authors are recommended to provide an ORCID. To obtain an ORCID, authors should register in the ORCID web site: <http://orcid.org>. Registration is free to every researcher in the world. Example of ORCID description is as follows:

<b>Author name</b>	<b>ORCID</b>
So, Hee	0000-0000-000-00X
Park, Hye-Il	0000-0000-000-00X
Yoo, All	0000-0000-000-00X
Jung, Jewerly	0000-0000-000-00X

# Authors' Checklist

The following list will be useful during the final checking of a manuscript prior to sending it to the journal for review. Please submit this checklist to the KSOE when you submit your article.

## < Checklist for manuscript preparation >

- I checked my manuscript has been 'spell-checked' and 'grammar-checked'.
- One author has been designated as the corresponding author with contact details such as
  - E-mail address
  - Phone numbers
- I checked abstract 1) stated briefly the purpose of the research, the principal results and major conclusions, 2) was written in 150–200 words, and 3) did not contain references (but if essential, then cite the author(s) and year(s)).
- I provided 5 or 6 keywords.
- I checked color figures were clearly marked as being intended for color reproduction on the Web and in print, or to be reproduced in color on the Web and in black-and-white in print.
- I checked all table and figure numbered consecutively in accordance with their appearance in the text.
- I checked abbreviations were defined at their first mention there and used with consistency throughout the article.
- I checked all references mentioned in the Reference list were cited in the text, and vice versa according to the APA style.
- I checked I used the international system units (SI) or SI-equivalent engineering units.

## < Authorship checklist >

JOET considers individuals who meet all of the following criteria to be authors:

- Made a significant intellectual contribution to the theoretical development, system or experimental design, prototype development, and/or the analysis and interpretation of data associated with the work contained in the article.
- Contributed to drafting the article or reviewing and/or revising it for intellectual content.
- Approved the final version of the article as accepted for publication, including references.

## < Checklist for publication ethics >

- I checked the work described has not been published previously (except in the form of an abstract or as a part of a published lecture or academic thesis).
- I checked when the work described has been published previously in other proceedings without copyright, it has clearly noted in the text.
- I checked permission has been obtained for use of copyrighted material from other sources including the Web.
- I have processed Plagiarism Prevention Check through reliable web sites such as [www.kci.go.kr](http://www.kci.go.kr), <http://www.ithenticate.com/>, or <https://www.copykiller.org/> for my submission.
- I agree that final decision for my final manuscript can be changed according to results of Plagiarism Prevention Check by JOET administrator.
- I checked one author at least is member of the Korean Society of Ocean Engineers.
- I agreed all policies related to 'Research and Publication Ethics'
- I agreed to transfer copyright to the publisher as part of a journal publishing agreement and this article will not be published elsewhere including electronically in the same form, in English or in any other language, without the written consent of the copyright-holder.
- I made a payment for reviewing of the manuscript, and I will make a payment for publication on acceptance of the article.
- I have read and agree to the terms of Authors' Checklist.

Title of article :

Date of submission : DD/MM/YYYY

Corresponding author :

signature

Email address :

※ E-mail this with your signature to [ksochj@ksoc.or.kr](mailto:ksochj@ksoc.or.kr)

# Publishing Agreement

## ARTICLE DETAILS

Title of article :  
Corresponding author :  
E-mail address :  
DOI : <https://doi.org/10.26748/KSOE.2XXX.XXX>

## YOUR STATUS

I am one author signing on behalf of all co-authors of the manuscript.

## ASSIGNMENT OF COPYRIGHT

I hereby assign to the Korean Society of Ocean Engineers, the copyright in the manuscript identified above and any tables, illustrations or other material submitted for publication as part of the manuscript (the "Article"). This assignment of rights means that I have granted to Korean Society of Ocean Engineers the exclusive right to publish and reproduce the Article, or any part of the Article, in print, electronic and all other media (whether now known or later developed), in any form, in all languages, throughout the world, for the full term of copyright, and the right to license others to do the same, effective when the Article is accepted for publication. This includes the right to enforce the rights granted hereunder against third parties.

## SCHOLARLY COMMUNICATION RIGHTS

I understand that no rights in patents, trademarks or other intellectual property rights are transferred to the Journal owner. As the author of the Article, I understand that I shall have: (i) the same rights to reuse the Article as those allowed to third party users of the Article under the CC-BY-NC License, as well as (ii) the right to use the Article in a subsequent compilation of my works or to extend the Article to book length form, to include the Article in a thesis or

dissertation, or otherwise to use or re-use portions or excerpts in other works, for both commercial and non-commercial purposes. Except for such uses, I understand that the assignment of copyright to the Journal owner gives the Journal owner the exclusive right to make or sub-license commercial use.

## USER RIGHTS

The publisher will apply the Creative Commons Attribution-Noncommercial Works 4.0 International License (CC-BY-NC) to the Article where it publishes the Article in the journal on its online platforms on an Open Access basis.

The CC-BY-NC license allows users to copy and distribute the Article, provided this is not done for commercial purposes and further does not permit distribution of the Article if it is changed or edited in any way, and provided the user gives appropriate credit (with a link to the formal publication through the relevant DOI), provides a link to the license, and that the licensor is not represented as endorsing the use made of the work. The full details of the license are available at <http://creativecommons.org/licenses/by-nc/4.0/legalcode>.

## REVERSION OF RIGHTS

Articles may sometimes be accepted for publication but later rejected in the publication process, even in some cases after public posting in "Articles in Press" form, in which case all rights will revert to the author.

I have read and agree to the terms of the Journal Publishing Agreement.

Corresponding author:

name

signature

※ E-mail this with your signature to [ksoehj@ksoe.or.kr](mailto:ksoehj@ksoe.or.kr) (Papers will not be published unless this form is signed and returned)

2022년도 한 해 동안 한국해양공학회지에 투고된 원고를 심사하신 분들입니다.  
심사위원 여러분께 감사드립니다.

강태순	(주)지오시스템리서치	박성주	인하대학교	윤상준	고등기술연구원
구남국	동의대학교	박승민	(주)헤인이엔씨	윤성모	KRISO
구원철	인하대학교	박영환	부산대학교	윤현규	창원대학교
김진우	KRISO	박중용	부경대학교	윤희철	충북대학교
김국현	동명대학교	박종천	부산대학교	이강수	KRISO
김도균	서울대학교	박준범	한국해양대학교	이문용	영남대학교
김동진	KRISO	배윤혁	제주대학교	이성욱	한국해양대학교
김범일	한국선급	서대원	한국선급	이우동	경상국립대학교
김병완	KRISO	서유태	서울대학교	이종무	KRISO
김성용	DNV GL	서정관	부산대학교	이철진	중앙대학교
김성재	인하대학교	송창용	목포대학교	전봉환	KRISO
김연중	인제대학교	신성원	한양대학교	정세민	조선대학교
김열우	부경대학교	안석환	중원대학교	정우철	한국해양대학교
김영훈	경남대학교	안진주	한국화학연구원	하윤진	KRISO
김정현	부산대학교	안현정	KRISO	하태민	강원대학교
김정환	동아대학교	양승호	울산과학대학교	함승호	창원대학교
김창수	한국과학기술원	오승훈	KRISO	허상환	인하대학교
남보우	서울대학교	우주현	한국해양대학교	현범수	한국해양대학교
도기덕	한국해양대학교	유선철	POSTECH	홍성훈	계명대학교
박선호	한국해양대학교	유재석	DGIST	황성철	KRISO

# (사)한국해양공학회 특별회원

한국해양공학회의 특별회원은 다음과 같으며, 귀사의 찬조에 진심으로 감사드립니다.(순서: 입회순)

한국선급 / 현대중공업(주) / 대우조선해양(주) / 선박해양플랜트연구소 /  
대양전기공업(주) / 한국해양조선기자재연구원 / 한국조선해양플랜트협회 /  
(주)파나시아 / 선보공업(주) / SK에코플랜트(주) /  
삼성중공업(주) / (주)유에스티21 / (주)해양정보기술



한국해양공학회 특별회원 가입방법은 학회홈페이지([www.ksoe.or.kr](http://www.ksoe.or.kr))의  
입회안내를 참고하시고, 기타사항은 학회 사무국으로 연락주시기 바랍니다.



# Research and Publication Ethics

Journal of Ocean Engineering and Technology (JOET) adheres to the guidelines published by professional organizations, including Committee on Publication Ethics (COPE; <https://publicationethics.org/>)

## 1. Authorship

*JOET considers individuals who meet all of the following criteria to be authors:*

- 1) Made a significant intellectual contribution to the theoretical development, system or experimental design, prototype development, and/or the analysis and interpretation of data associated with the work contained in the article.
- 2) Contributed to drafting the article or reviewing and/or revising it for intellectual content.
- 3) Approved the final version of the article as accepted for publication, including references.

Contributors who do not meet all of the above criteria may be included in the Acknowledgment section of the article. Omitting an author who contributed to your article or including a person who did not fulfill all of the above requirements is considered a breach of publishing ethics.

**Correction of authorship after publication:** JOET does not correct authorship after publication unless a mistake has been made by the editorial staff.

## 2. Originality and Duplicate Publication

All submitted manuscripts should be original and should not be in consideration by other scientific journals for publication. Any part of the accepted manuscript should not be duplicated in any other scientific journal without permission of the Editorial Board, although the figures and tables can be used freely if the original source is verified according to the Creative Commons Attribution License (CC BY-NC). It is mandatory for all authors to resolve any copyright issues when citing a figure or table from other journal that is not open access.

## 3. Conflict-of-Interest Statement

Conflict of interest exists when an author or the author's institution, reviewer, or editor has financial or personal relationships that inappropriately influence or bias his or her actions. Such relationships are also known as dual commitments, competing interests, or competing loyalties. These relationships vary from being negligible to having a great potential for influencing judgment. Not all relationships represent true conflict of interest. On the other hand, the potential for conflict of interest can exist regardless of whether an individual believes that the relationship affects his or her scientific judgment. Financial relationships such as employment, consultancies, stock ownership, honoraria, and paid expert testimony are the most easily identifiable conflicts of interest and the most likely to undermine the credibility of the journal, the authors, or of the science itself. Conflicts can occur for other reasons as well, such as personal relationships, academic competition, and intellectual passion. If there are any conflicts of interest, authors should disclose them in the manuscript. The conflicts of interest may occur during the research process as well; however, it is important to provide disclosure. If there is a disclosure, editors, reviewers, and reader can approach the manuscript after understanding the situation and the background of the completed research.

## 4. Management Procedures for the Research and Publication Misconduct

When JOET faces suspected cases of research and publication misconduct such as a redundant (duplicate) publication, plagiarism, fabricated data, changes in authorship, undisclosed conflicts of interest, an ethical problem discovered with the submitted manuscript, a reviewer who has appropriated an author's idea or data, complaints against editors, and other issues, the resolving process will follow the flowchart provided by the Committee on Publication Ethics (<http://publicationethics.org/resources/flowcharts>). The Editorial Board of JOET will discuss the suspected cases and reach a decision. JOET will not hesitate to publish

errata, corrigenda, clarifications, retractions, and apologies when needed.

## 5. Editorial Responsibilities

The Editorial Board will continuously work to monitor and safeguard publication ethics: guidelines for retracting articles; maintenance of the integrity of the academic record; preclusion of business needs from compromising intellectual and ethical standards; publishing corrections, clarifications, retractions, and apologies when needed; and excluding plagiarism and fraudulent data. The editors maintain the following responsibilities: responsibility and authority to reject and accept articles; avoiding any conflict of interest with respect to articles they reject or accept; promoting publication of corrections or retractions when errors are found; and preservation of the anonymity of reviewers.

## 6. Hazards and human or animal subjects

If the work involves chemicals, procedures or equipment that have any unusual hazards inherent in their use, the author must clearly identify these in the manuscript. If the work involves the use of animal or human subjects, the author should ensure that the manuscript contains a statement that all procedures were performed in compliance with relevant laws and institutional guidelines and that the appropriate institutional committee(s) has approved them. Authors should include a statement in the manuscript that informed consent was obtained for experimentation with human subjects. The privacy rights of human subjects must always be observed.

Ensure correct use of the terms sex (when reporting biological factors) and gender (identity, psychosocial or cultural factors), and, unless inappropriate, report the sex and/or gender of study participants, the sex of animals or cells, and describe the methods used to determine sex and gender. If the study was done involving an exclusive population, for example in only one sex, authors should justify why, except in obvious cases. Authors should define how they determined race or ethnicity and justify their relevance.

## 7. Secondary publication

It is possible to republish manuscripts if the manuscripts satisfy the conditions of secondary publication. These are:

- The authors have received approval from the Editorial Board of both journals (the editor concerned with the secondary publication must have access to the primary version).
- The priority for the primary publication is respected by a publication interval negotiated by editors of both journals and the authors.
- The paper for secondary publication is intended for a different group of readers
- The secondary version faithfully reflects the data and interpretations of the primary version.
- The secondary version informs readers, peers, and documenting agencies that the paper has been published in whole or in part elsewhere, for example, with a note that might read, "This article is based on a study first reported in the [journal title, with full reference]"
- The title of the secondary publication should indicate that it is a secondary publication (complete or abridged republication or translation) of a primary publication.

## 8. Complaints and Appeals

The process of handling complaints and appeals follows the guidelines of the COPE available from: <https://publicationethics.org/appeals>

## 9. Post-publication discussions and corrections

The post-publication discussion is available through letter to editor. If any readers have a concern on any articles published, they can submit letter to editor on the articles. If there found any errors or mistakes in the article, it can be corrected through errata, corrigenda, or retraction.



The Korean Society of Ocean Engineers